

SHAPE, COMPOSITION AND WAVELENGTH DEPENDENT SURFACE ENHANCED RAMAN SPECTROSCOPIC STUDIES ON METAL AND ALLOY NANOPARTICLES

Thesis submitted to the
University of Calicut in partial fulfillment of the
requirements for the award of the degree of

DOCTOR OF PHILOSOPHY IN CHEMISTRY
under the Faculty of Sciences

by

SUMITHA CHANDRAN U. K.

Under the guidance of
Dr. P. Raveendran




**DEPARTMENT OF CHEMISTRY
UNIVERSITY OF CALICUT
KERALA
AUGUST 2021**

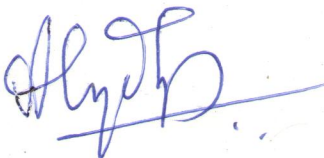
CERTIFICATE

This is to certify that the thesis entitled “**SHAPE, COMPOSITION AND WAVELENGTH DEPENDENT SURFACE ENHANCED RAMAN SPECTROSCOPIC STUDIES ON METAL AND ALLOY NANOPARTICLES**” is an authentic record of the research work carried out by **Sumitha Chandran U K** under my guidance for the award of the degree of Doctor of Philosophy in Chemistry under the faculty of Sciences, University of Calicut, Kerala and the same has not been submitted elsewhere for any degree or diploma. The suggestions/ corrections/ recommendations made by the adjudicators have been included in the revised thesis.

Calicut University
June 2022


Dr. P. Raveendran
(Supervising Teacher)

Dr. P. RAVEENDRAN, Ph.D.
Professor
Department of Chemistry
University of Calicut, Kerala - 673635


HEAD OF THE DEPARTMENT
DEPARTMENT OF CHEMISTRY
UNIVERSITY OF CALICUT
KERALA-673 635



DECLARATION

I hereby declare that the thesis entitled **“SHAPE, COMPOSITION AND WAVELENGTH DEPENDENT SURFACE ENHANCED RAMAN SPECTROSCOPIC STUDIES ON METAL AND ALLOY NANOPARTICLES”** is the bonafide report of the original work carried out by me under the supervision of Dr. P. Raveendran, Professor, Department of Chemistry, University of Calicut for the award of the degree of Doctor of Philosophy in Chemistry under the Faculty of Sciences, University of Calicut, Kerala. The contents of this thesis have not been submitted to any other institute or University for the award of any degree or diploma.

Calicut University
August 2021

Sumitha Chandran U K

ACKNOWLEDGEMENT

First and foremost, I would like to express my deep and sincere gratitude to my Research Supervisor, Dr. P. Raveendran, Professor, Department of Chemistry, University of Calicut, for giving me the opportunity to do research and providing invaluable guidance throughout this research. He has inspired me to become an independent researcher and helped me realize the power of critical reasoning. It was a great privilege and honour to work and study under his guidance.

I would like to thank our Head of the Department, Dr. Yahia. A. I and former heads of the department Dr. V. M. Abdul Mujeeb and Dr. K. Muraleedharan, for providing all facilities for pursuing my research work. I also thank all faculty members of Chemistry department, Prof. Abraham Joseph, Prof. D. Bahuleyan, Dr. N. K. Renuka, Dr. M. T. Rameshan, and Dr. Pradeepan Periyat for their valuable suggestions and support during doctoral committee meetings. My sincere thanks to the non-teaching staff of our department.

I gratefully acknowledge Sri. Mohanan. A., Librarian, Department of Chemistry and Sri. Satheesan. K., Technician, UOC for the assistance they have given to me.

I thank the manager of SN Trust for giving me permission to do my PhD. I would also extend my sincere thanks to the principal of my parent institution Dr. Ajayakumar Koorma, former principal Dr. Sivadasan Thirumangalath, HOD Dr. Anitha P. K., former HOD Dr.

P. Reetha, my colleagues and non-teaching staff of SN college, Kannur for their full-hearted support.

I take this opportunity to express my gratitude towards members of my research group Dr. Bindu. U., Vineeth Madhavan, Dr. Anju Ajayan, Dr. Jyothi. P. R, Dr. Anu Antony for their constant support and motivation throughout my research work. I would also like to mention the support of Dr. Shijina Govindan, Dr. Jasmine Thomas, Jai Thomas and Dr. Divya. T.

I gratefully acknowledge the help of all research scholars of the Department of Chemistry. I would like to mention Dr. Niveditha. P. for her valuable help in taking SEM, Dr. Vijisha Vijayan, Sumayya P.C for their help in carrying out computational studies, Vinduja Ram for carrying out AFM and Anju. M. from the department of Physics for taking Raman spectrum. I also like to mention the help from department of Botany and photography unit of Calicut university for taking beautiful pictures of my samples. Special thanks to all members of physical lab for their invaluable love and support.

I gratefully acknowledge the financial assistance received under FDP and JRF programs from UGC. I acknowledge the premier institutions JNCASR Bangalore, STIC and Department of Physics of CUSAT, CSIF Calicut University for providing facilities for analysis.

I am forever indebted to my teachers for giving me the opportunities and experiences that have made me who I am. They selflessly encouraged me to explore new directions in life.

I express my deep and sincere gratitude to my parents for their continuous and unparalleled love, help and support. This journey would not have been possible without them and I dedicate this milestone to them. I am grateful for my brother for always being there for me.

I would especially thank my family. My husband has been extremely supportive of me throughout this entire process and has made countless sacrifices to help me get to this point. My children have made me stronger, better and more fulfilled than I could have ever imagined.

I also extend my gratitude towards my in-laws, all my friends and relatives.

Finally, I would like to praise and thank God, the Almighty who has granted countless blessing, knowledge and opportunity to accomplish the thesis.

Sumitha Chandran U K

PREFACE

Surface enhanced Raman spectroscopy (SERS) is considered to be one of the most useful analytical tools for the determination of molecular species at very low concentrations. Here the Raman scattering technique is coupled with the use of a metal nanoparticle surface on which the molecule gets adsorbed. The poor Raman scattering cross-section of Raman spectroscopy is overcome by the surface enhancement of the signal, generally by a factor of about 10^6 , due to the chemical enhancement (CE) and the classical electromagnetic enhancement (CEME). CE arises from the interaction of the molecule with the surface and the plausible, transient, electron transfer between the molecular orbitals and the surface. CEME is attributed to the enhancement of the local electric field experienced by the molecule. CEME makes SERS a unique tool as the spectral intensities also depend on the proximity of a specific functional group of the molecule in relation to the surface of the metal nanoparticle, its orientation with respect to the surface and possibly the geometry of the measurement.

Since its discovery, numerous researchers have tried to understand the exact mechanism of the enhancement process and the surface selection rules, with the objective of using SERS as a more versatile analytical tool than the conventional Raman spectroscopy. It is well known that nanoparticles of Au, Ag, and their alloys exhibit a localized surface plasmon resonance (LSPR) and the conduction band electrons on the metal nanoparticle undergo collective oscillation by absorbing the radiation with the characteristic wavelength. In fact, by appropriate

alloying of the component metals, one can tune the LSPR of the systems. It is important that SERS can in fact be employed as a more versatile technique and it can provide us the mode of binding and orientation of the molecule with respect to the surface. In this thesis, we investigate the dependence of SERS on the wavelength of the plasmon absorption (λ_{\max}), excitation wavelength (λ_{exc}), composition, and the shape of the molecule.

The first chapter provides a general introduction to the basic aspects of nanoscience, properties of metal nanoparticles, theories of surface plasmon absorption, fundamentals of Raman spectroscopy, and SERS. A description of the basics of some of the analytical and instrumental techniques used for the analysis are described in Chapter 2.

Wavelength-dependent SERS studies of 1,4-BDT under three conditions—plasmon resonant, near resonant and off resonant conditions, with reference to the absorption maximum λ_{\max} of the two excitation lines 532nm and 1064nm are presented, in Chapter 3. We investigate if there is any relation between the value of λ_{\max} and λ_{exc} on SERS spectra using Au, Ag, and AuAg alloy nanoparticles of various composition in association with the two excitation lines mentioned above. Cellulose acetate sheet was used as support for the nanoparticles. Networked metal and alloy NPs, are also employed. One observes significant differences between the relative intensities and spectral profiles.

Preferential binding of different atoms of model molecular systems such MB and R6B on Au, Ag, and AuAg alloy NPs is investigated in Chapter 4 using FT Raman spectrometer. Cotton fabric is used as support for the

nanoparticles, in this case. Significant changes are observed in the SERS spectra from the various substrates. These are attributed to the difference in the binding of these multi-dentate molecules with the surface.

SERS studies of 1,4-BDT, MB and R6B on Ag substrates with different shape/morphology are carried out and presented in Chapter 5. Ag NF structures of different morphologies were prepared for investigating the spectral differences. Shape-dependent studies on Ag were carried out by preparing three Ag NF substrates containing flowers with varying degrees of sharpness and we studied how this slight change in flower morphology going to affect SERS spectra. We were able to predict the orientation of these analytes by interpretation of the SERS data.

SERS spectra of 1,4-BDT, MB and R6B studied over three Au-based SERS substrate systems, viz., the faceted polygonal, NF, and Au/C hybrid substrates, are presented in Chapter 6. Considerable differences are observed in the SERS with reference to the different substrate systems. Specifically, one observes a difference in the mode and strength of binding of these molecules on the three substrates as evidenced by the position of the metal-adsorbate peaks. The metal-adsorbate bonds are stronger in the case of the NF system in comparison with the polygonal systems. This must be attributed to the largely unsatisfied Au surfaces of the NFs, making the metal-adsorbate peaks stronger. This is also evidenced by the increased electron density in the π -ring systems in the case of the adsorbate molecules attached to the rather smooth polygonal systems. In comparison with Ag NF systems

studied in Chapter 5, the observed differences between the different SERS substrate systems are more pronounced.

Conclusions from the experimental observations presented in the earlier chapters is presented in Chapter 7. The results presented in the above chapters reiterate that SERS cannot be considered as a routine Raman spectroscopic technique and care must be taken to analyze the SERS spectra. SERS spectra recorded from different substrates vary based on the shape of the individual nanoparticles, their shapes as well as the orientation of the molecule with respect to the surface. Since the molecular orientation depends on the mode of binding, the nature of the metal or alloy surface on which also affects the SERS spectra. Since there is selective enhancement for some of the vibrational modes and suppression of some others based on binding and orientation of the molecules, care must be taken to interpret the spectra correctly.

CONTENTS

<i>Chapter No.</i>	<i>Title</i>	<i>Page No</i>
1	INTRODUCTION	1-49
	1.1. Metal Nanoparticles	2
	1.2. Classification of Metal nanoparticles	3
	1.3. Nanoparticle synthesis	4
	1.3.1. Gas -Solid phase methods	4
	1.3.2. Wet chemical (liquid phase) methods	7
	1.4. Synthesis of metal NPs	9
	1.4.1. Chemical methods	9
	1.4.2. Green synthesis of metallic NPs	10
	1.5. Fundamental properties of metal NP	12
	1.5.1. Size effects	12
	1.5.1.1. Increase in relative surface area	12
	1.5.1.2. Quantum confinement effects	13
	1.5.2. Structural properties	15
	1.5.3. Thermal properties	16
	1.5.4. Chemical properties	16
	1.5.5. Mechanical properties	16
	1.5.6. Magnetic properties	16
	1.5.7. Electronic properties	17
	1.5.8. Optical properties	18
	1.6. Plasmonics	19
	1.7. Theories of Plasmonics	22
	1.7.1. Mie theory	22
	1.7.2. Gans theory	24

1.7.3. Drude dispersion model	25
1.7.4. Effective medium theory	28
1.8. Applications of metallic nanoparticles	32
1.8.1. Biological and biomedical applications	32
1.8.2. Catalytic applications	34
1.9. Raman spectroscopy	34
1.10. Surface enhanced Raman spectroscopy	40
1.10.1. Chemical enhancement mechanism of SERS	41
1.10.2. Electromagnetic enhancement mechanism of SERS	42
1.11. Applications of surface enhanced Raman spectroscopy	45
1.12. Present study	47
2 ANALYTICAL METHODS	51-66
2.1. Electron microscopic techniques, SEM and TEM	51
2.1.1. Scanning Electron Microscope (SEM)	52
2.1.2. Transmission Electron Microscopy (TEM)	53
2.2. Scanning Probe Microscope (SPM)	56
2.2.1. Atomic force microscopy	57
2.3. X-ray diffraction technique	59
2.4. Spectroscopic techniques	61
2.4.1. UV-Vis-NIR absorption spectroscopy	62
2.4.2. Instrumentation	62
2.5. RAMAN spectroscopy	63
2.6. SERS Spectral Studies	66
2.7. Quantum chemical calculations	66

3	PLASMON- RESONANT, NEAR- RESONANT AND OFF- RESONANT SERS OF MODEL DITHIOL SYSTEMS	67-98
	3.1 Introduction	67
	3.2. Experimental Methods	75
	3.2.1. Materials	75
	3.2.2. Synthesis of Au, Ag and Au-Ag alloy nanoparticles	75
	3.2.3. Preparation of NPs decorated Cellulose Acetate sheets	76
	3.2.4. Preparation of networked Au, Ag and Au Ag alloy NP Films	77
	3.3. RESULTS AND DISCUSSIONS	77
	3.3.1. UV-VISIBLE, FESEM and AFM studies	77
	3.3.2. SERS Studies	84
	3.3.2.1. Relative Intensities	87
	3.3.2.2. FT-SERS on networked NP substrates using 1064 nm laser Excitation	88
	3.3.2.3. Plasmon resonant and near-resonant SERS	91
	3.3.2.4. FT-SERS Spectra of other dithiols on networked and non-networked substrates	95
	3.4. Conclusions	97
4	FT-SERS studies of Methylene Blue and Rhodamine 6B on Au, Ag and Au Ag alloy nanoparticle (NP) embedded cotton fabrics	99-119
	4.1. Introduction	99
	4.2. Experimental details	104
	4.3. Results and Discussion	104
	4.3.1. SERS studies of MB	107

	4.3.2. SERS of R6B	114
	4.4. Conclusions	119
5	Dependence of SERS spectra on the Shape/ Morphology of Ag NP substrates: Case studies of 1,4-Benzene Dithiol, Methylene Blue and Rhodamine-6B on Nanoflowers of different roughness	121-137
	5.1 Introduction	121
	5.2. Experimental details	125
	5.2.1. Synthesis of Ag Nanoflowers (NFs)	125
	5.3. Results and Discussion	125
	5.3.1. UV-VISIBLE, FESEM, TEM and XRD	125
	5.3.2. SERS studies	128
	5.3.2.1. 1,4-BDT	128
	5.3.2.2. FT SERS of MB over Ag NF1, NF2 and NF3	131
	5.3.2.3. Rhodamine 6B	134
	5.4. Conclusions	136
6	Dependence of SERS spectra of 1,4-BDT, MB, and R6B on the Shape/ Morphology of Au NP substrates	139-158
	6.1. Introduction	139
	6.2. Experimental details	141
	6.2.1. Synthesis of Au/C hybrid NFs	141
	6.2.2. Synthesis of Au NFs	141
	6.2.3. Polygonal Au NPs	141
	6.2.4. Preparation of SERS substrates	142
	6.3. Results and discussions	142
	6.3.1. UV-Visible Absorption spectral studies	142
	6.3.2. Morphological studies	143
	6.3.3. XRD studies	144

	6.3.4. SERS Studies	145
	6.3.4.1. 1, 4- BDT	145
	6.3.4.2. SERS of Methylene Blue (MB)	149
	6.3.4.3. Rhodamine 6B (R6B)	154
	6.4. Conclusions	157
7	CONCLUSIONS AND OUTLOOK	159-164
	REFERENCES	165-189

GLOSSARY OF TERMS

FEEM	-	Field emission electron microscope
SEM	-	Scanning electron microscopy
TEM	-	Transmission electron microscopy
STM	-	Scanning tunnelling microscopy
AFM	-	Atomic force microscopy
XRD	-	Xray diffractometer
SAED	-	Selected area electron diffraction
EDAX	-	Energy dispersive analysis of X-rays
MNPs	-	Metal nanoparticles
NP	-	nanoparticle
Au NP	-	Gold nanoparticles
Ag NP	-	Silver nanoparticle
Cu NP	-	Copper nanoparticle
Pt	-	Platinum
DOS	-	Density of state
SPR	-	Surface plasmon resonance
LSP	-	Localized surface plasmon
EF	-	Electric field
EM	-	Electromagnetic

Au NR	-	Gold nanorod
SERS	-	Surface enhanced Raman spectroscopy
SERRS	-	Surface enhanced resonance Raman spectroscopy
CEME	-	Classical electromagnetic enhancement
CE	-	Chemical enhancement
1,4- BDT	-	1,4- Benzene dithiol
1,3- BDT	-	1,3- Benzene dithiol
1,2-BDT	-	1,2- Benzene dithiol
MB	-	Methylene blue
R6B	-	Rhodamine 6B
DFT	-	Density functional theory
TDDFT	-	Time dependent density functional theory
DRS	-	Diffuse reflectance spectra
NIR	-	Near infra-red
CT	-	Charge transfer
CA	-	Cellulose acetate
FT-SERS	-	Fourier transform surface enhanced Raman spectroscopy
FT-Raman	-	Fourier transform Raman
Au-N	-	Gold-Nitrogen
Au-S	-	Gold- Sulphur

Ag NF - Silver nanoflower

Au NF - Gold nanoflower

Au/C hybrid NF- Gold/ Carbon hybrid nanoflower

CHAPTER 1

INTRODUCTION

Materials science has undergone a major revolution in the past couple of decades with the design of materials at nanoscale dimensions where size-dependent modifications in the electronic, optical, magnetic, and other properties. This offers tremendous opportunities in many advanced areas of chemistry, physics, biology, and medicine.¹⁻¹⁰ The birth of nanoscale science is often referred to the famous lecture by Richard Feynman at the American Physical society meeting entitled “There is plenty of room at the bottom”.¹¹ He suggested that there are tremendous, hitherto unexplored, opportunities in the design of small scale materials with the possibility of smart materials with unique properties. The term Nanotechnology was coined by Norio Taniguchi to describe the manipulation of matter on an atomic, molecular and supramolecular scale.¹² The development of electron microscopy enabled researchers to see materials at the nanoscale dimensions. Field emission electron microscope (FEEM) revolutionized the transmission electron microscopy (TEM), scanning electron microscopy (SEM), and scanning tunnelling microscopy (STM) to get high resolution images of the materials. Atomic force microscopy (AFM) helped researchers to investigate the unique surface structures of the materials with great details.

Another major milestone in nanoscience was the discovery of fullerene by Croto, Curl, and Smalley. The interest in carbon nanostructures was followed up by the discovery of carbon nanotubes and graphene.¹³⁻²⁰

1.1. Metal nanoparticles

Metal nanoparticles (MNPs) constitute an important class of materials. Among these the NPs of noble metals such Au, Ag, Pt and Pd are of immense significance. At nanoscale dimensions, these MNPs exhibit properties that are quite different from their bulk samples. Historically, MNPs have been widely used for the generation of beautiful colours. One of the best examples is Lycurgus cup. It appeared red in transmitted light and green in reflected light. This is due to the presence of silver and gold nanoparticles of 70 nm size and 7:3 compositions in addition to about 10% Cu. The beautiful colours of the windows of old churches and many ceramic potteries were due to the incorporation of Au, Ag and Cu NPs. In the seventeenth century, Andreas Cassius et al described procedure for preparing Au NP with intense purple colour, so called “Purple of Cassius”.

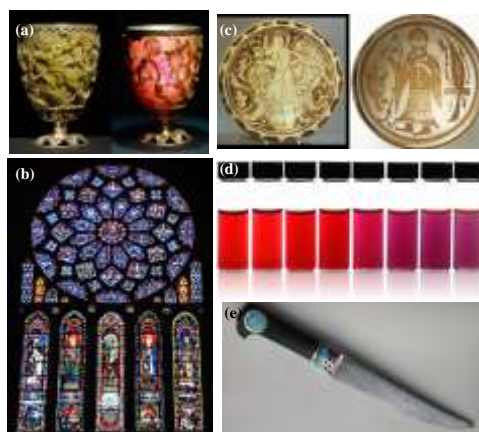


Figure 1.1: (a) Lycurgus cup in reflected and transmitted light (b) stained glass windows of old church, (c) ceramic potteries, (d) ruby gold, (e) Damascus steel (adapted from Wikipedia).

In the era of modern science, it was Michael Faraday in 1857 who reported the preparation of colloidal Au NPs by the reduction of Gold

salts with reagents including organic compound or Phosphorous. He explained the red colour of the solution as a result of small sized Au particles in their finely divided form.

1.2. Classification of MNPs

Based on the degree of spatial confinement, nanoparticles can be classified. If metal nanoparticles are spatially confined in all the three dimensions, they are termed zero-dimensional materials.²¹ Based on composition, they can be categorized into monometallic (originated from single type metal) and bimetallic (presence of more than one type metal).²² Bimetallic NP includes core-shell and alloy NP.²³ If the electron motion is confined in one-dimension, two-dimensional nanomaterials arise. If the confinement is in two dimensions, one dimensional material such as nano wires result. Metallic nanoparticles exhibit variety of shapes and they are named based on the shape they possess; for example, silver nanocubes, Gold nanorods etc.

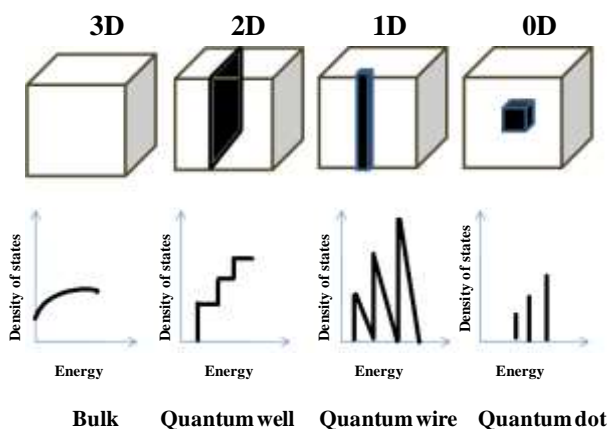


Figure 1.2: Schematic diagram showing bulk 3D material, 2D,1D and 0D material and corresponding Density of States (DOS) (adapted from Dresselhaus, M. S.; Chen, G.; Tang, M. Y.; Yang, R. G.; Lee, H.; Wang, D. Z.; Ren, Z. F.; Fleurial, J. P.; Gogna, P., *Adv. Mater.* **2007**, *19*, 1043–1053.)

1.3. Nanoparticle synthesis

Fundamentally there are two methods available for the synthesis of MNPs. The first is the top-down approach which involves cutting down the bulk into nanodimensions.²⁴ The latter is the bottom-up approach where MNPs are prepared, building up the nanostructures from the metal atoms produced by the reduction of metal ions by suitable reducing agents under different protective environments.²⁵

1.3.1. Gas -Solid phase methods

Gas phase synthesis can be further classified into

- (a) Chemical Vapour Deposition (CVD) - In this method a substrate is exposed to one or more volatile precursors of metallic nanostructures, then the precursors may react or decompose on the substrate surface to produce corresponding metal nanostructures.²⁶
- (b) Laser ablation - In this method, NP are generated by nucleation and growth of laser vaporized species in a background gas.²⁷
- (c) Flame pyrolysis - It is a gas phase combustion method for producing NP with high purity and narrow size distribution. Precursors can be introduced into flame either through an evaporation system at controlled temperature or through a spray system, in liquid phase.²⁸
- (d) Inert gas condensation - In this a metallic or inorganic material is vaporized using evaporation sources and a rapid controlled condensation is done to produce the required particle size.²⁹

- (e) Sputtering - In this method a controlled gas like chemically inert Argon is introduced into a vacuum chamber and particles are ejected from the solid material due to bombardment.³⁰

Gas phase synthetic methods are shown schematically in the figure

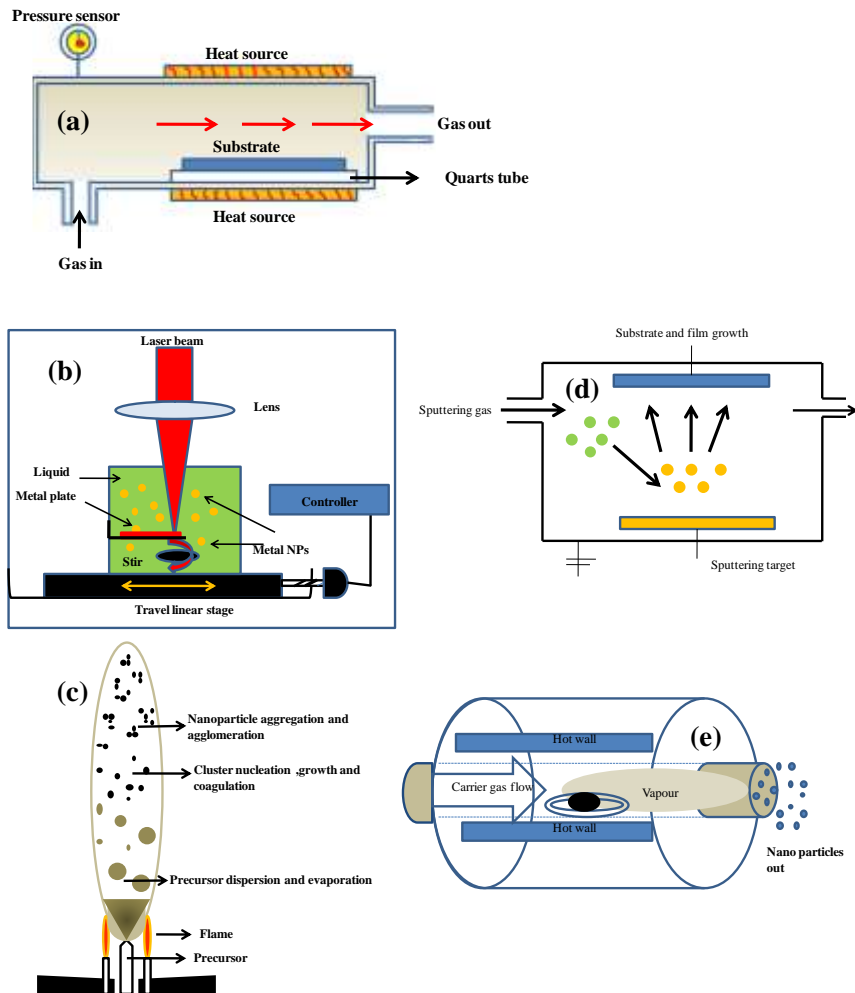


Figure 1.3: Schematic diagram for gas phase synthesis of metal NP; (a) chemical vapour deposition, (b) laser ablation, (c) flame pyrolysis, (d) inert gas condensation, (e) sputtering (images adapted from Wikipedia).

Solid phase method involves

- (a) Agitated ball milling - In ball milling a powder mixture placed in the ball mill is subjected to high energy collision from the balls. ³¹
- (b) Lithography - This technique is based on depositing, etching or writing, on a surface feature with dimensions on the order of nms. Lithography can be performed using light (optical or photolithography), electrons (e-beam lithography), ions (i-beam lithography), or x-ray (x-ray lithography LIGA) depending on the desired minimum feature size of the outputs. ³²

Solid phase methods are shown schematically in the figure

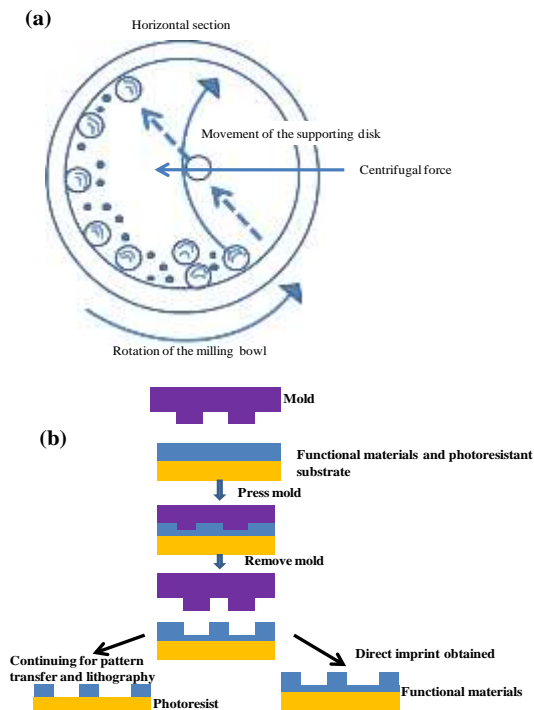


Fig 1.4: Solid phase synthesis of metal NPs: (a) agitated ball milling, (b) nanolithography (images adapted from Wikipedia).

1.3.2. Wet chemical methods

Some of the liquid phase NP synthesis methods are discussed below

- (a) Sol-gel method - sol gel process involves chemical transformation of a liquid (the sol) into a gel state, and with subsequent treatment and transition into a solid oxide material. It is highly useful for the synthesis of ceramics or metal oxides.
³³
- (b) Co-precipitation method- It is generally done by the co-precipitation of metal cations in the soluble salt form from a common medium as hydroxides, carbonates, oxalates etc. Usually, oxides and carbonates of the relevant metals are taken and these are digested with an acid and then a precipitating agent was added. The precipitate is dried and heated to the required temperature in appropriate atmosphere to produce the final product. Magnetic NP is generally prepared by this method.³⁴
- (c) Solvothermal synthesis - In this method chemical reactions are carried out in solvents under moderate to high pressure and temperature around their critical points in sealed vessels. If water is used as the solvent; the method is called “hydrothermal synthesis”.³⁵
- (d) Biomimetic synthesis - It uses biologically inspired templates and methods for NP synthesis. Some of them are the use of single amino acids, small synthetic peptides, combinatorial libraries etc.³⁶

- (e) Microemulsions - Microemulsions are clear, thermodynamically stable, isotropic liquid mixtures of oil, water and surfactant, frequently in combination with a cosurfactant. It is a controlled method for the preparation of NP with a narrow size distribution. The mechanism is based on intramicellar nucleation and growth and particle aggregation.³⁷

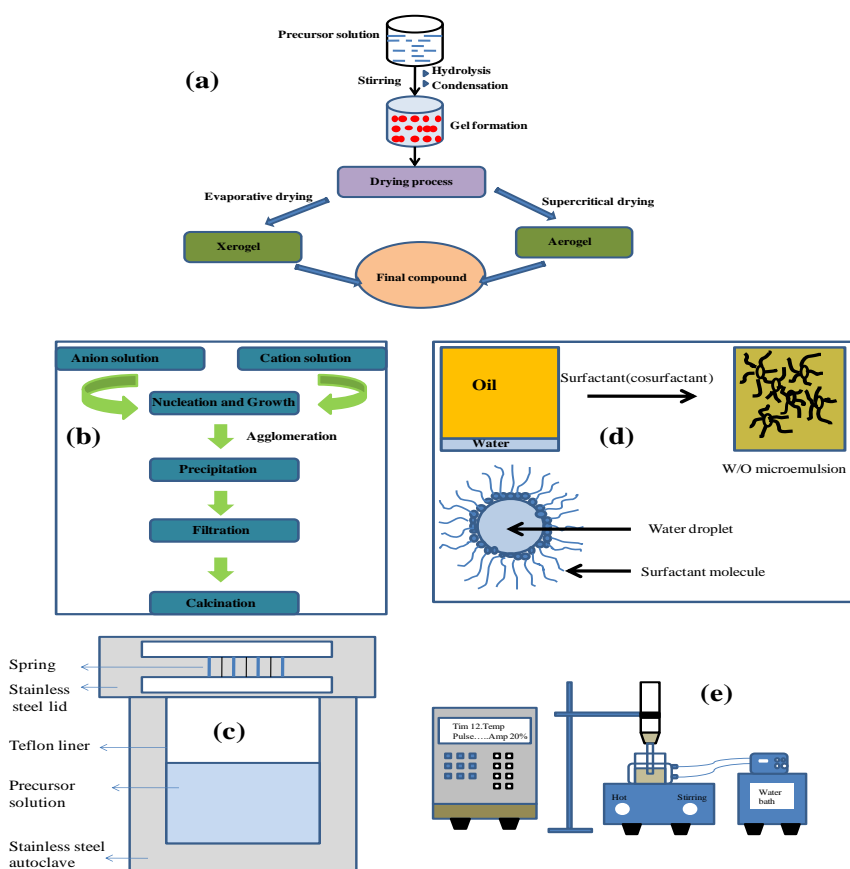


Fig 1.5: Liquid phase metal NP synthesis; (a) sol-gel, (b) co-precipitation, (c) solvothermal synthesis, (d) micro emulsion, (e) sonochemical synthesis (images adapted from Wikipedia).

- (f) Sonochemical synthesis - Use of high intensity ultra sound for the synthesis of NP is known as sonochemical synthesis. The mechanism behind sonochemical synthesis is acoustic cavitation (the formation, growth, and implosive collapse of bubbles) and the process can be classified as 1⁰ sonochemistry (gas phase chemistry occurring inside the collapsing bubbles), 2⁰ sonochemistry (solution-phase chemistry occurring outside the bubbles), and physical modifications.³⁸

Some of the liquid phase nanoparticle synthetic methods are shown in the Figure 1.5

1.4. Synthesis of metal NPs

Most common methods for the synthesis of metal NPs involve chemical methods and green synthetic methods.

1.4.1. Chemical methods

Chemical method consists of reduction of the corresponding metal ions from metal salts using suitable reducing agents and subsequent stabilization of the NPs using appropriate stabilizing agents. Borohydrides, aminoboranes, formaldehyde, hydrazine, hydroxylamine, polyols, citric and oxalic acids, sugars, hydrogen, acetylene are commonly employed reducing agents and tri sodium citrate dehydrate, ligands containing sulphur, nitrogen, oxygen phosphorous, dendrimers, polymers and surfactants like CTAB (Cetyl trimethylammonium bromide) are functioning as capping agents. One of the oldest methods for Au NP synthesis is Turkevich method that involves reduction of

HAuCl₄ by citrate in water. Here citrate is acting both as reducing and stabilizing agent.³⁹ Frens modified Turkevich method by controlling the ratio of reducing agent/stabilizing agent.⁴⁰ Thermally stable and air stable Au NPs of controllable size and low dispersity is achieved by Brust-Schiffrin method that involve phase transfer agent Tetra Octyl Ammonium Bromide (TOAB) which causes phase transfer of AuCl₄⁻ from an aqueous solution to a toluene solution and reduced by NaBH₄.⁴¹ Song et al has shown the electrochemical synthesis of Au on the surface of multiwalled carbon nanotubes with glassy carbon electrodes.⁴² Yu et al prepared Ag NP by chemical reduction using dextrose in which macromolecular and polyanionic Na⁺-poly (γ -glutamic acid) (PGA) Silver nitrate complex acted as both a metal ion provider and a particle protector.⁴³ In another report Liu et al synthesized ultrafine Ag NP from bulk Ag substrates in aqueous solutions by sonoelectrochemical methods.⁴⁴ Goia et al tailored particle size of monodispersed colloidal gold by reducing tetrachloric(III) acid with iso-ascorbic acid.⁴⁵ Jana et al prepared Au and Ag NP using seeding growth method. Here tri sodium citrate was used as a source of OH⁻ ions in the seeding step; NaBH₄ was used as reducing agent.⁴⁶

1.4.2. Green synthesis of metallic NPs

Many green chemical methods have been developed in the recent years. For example, Raveendran and Wallen had shown that it is possible to synthesize metal and alloy nanoparticles by the reduction of metal ions such as Au and Ag and then passivating these particles using protecting agents such as starch.⁴⁷ There are also biosynthetic methods for the

preparation of MNPs using microbes, enzymes, and plant extracts due to their environmentally benign nature. Bacterial synthesis of metal NP occurs either by extracellular or by intracellular mechanisms. Beveridge and Murray et al first reported the deposition of gold NP extracellularly on *Bacillus subtilis* cell wall when gold chloride solution was used to suspend unfixed wall. ⁴⁸ Capability of *Pseudo monas aeruginosa* to synthesis variety of NPs intracellularly was reported by Srivastava et al. ⁴⁹ Actinomycetes are able to produce various bioactive compounds and Otari et al explained the green biosynthesis of Ag NP using actinobacteria *Rhodo coccus* NCIM 2891. ⁵⁰ In comparison to bacteria, fungi have higher productivity in terms of NP generation and higher tolerences to metals. Bhargava et al has studied the effect of various parameters and the yield of fungi *clodosporium oxysporum* to convert gold ion into NPs. ⁵¹ Biosynthesis of NPs using algae was reported by Ferreira et al and he employed the dried unicellular microalga, *Chlorella vulgaris* for the biosynthesis of Ag NPs. ⁵² The thick outer surface coating of capsid proteins in viruses provide a highly suitable platform for interaction with metallic ions. Cao et al employed red clover necrotic mosaic virus (RCNMV) for the synthesis of NP for the controlled delivery of doxorubicin drug for chemotherapy. ⁵³

Several studies reported that many plants and plant extracts are very good candidates for NP synthesis. Shankar et al has reported biosynthesis of Au NP using plant *Azadirachta indica* and *Gardea-Torresdey* et al has used *Medicago sativa* for Au NP synthesis. ^{54,55} *Aloevera* and lemon grass were also found to be very good in NP synthesis by Chandran et al and Shankar et al. ⁵⁶ Leaf extracts of

Mangifera indica and banana peel were found to be useful for NP synthesis by Philip et al and Bankar et al.⁵⁷ Prasad and Elumalai et al reported Ag NP synthesis using leaf extracts of polyalthia logifolia.⁵⁸ Ahmed et al has proposed a single step, rapid green method for synthesizing Ag NPs by plant extracts of Crotonia retusa as well as Terminalia arjuna as reducing and stabilizing agent.⁵⁹

1.5. Fundamental properties of metal NP

Fundamental properties of metallic NP are different from bulk due to following reasons.

1.5.1. Size effects

1.5.1.1. Increase in relative surface area

When compared to bulk, nanomaterials exhibit greater surface area to volume ratio. Reduction in size also increases number of surface atoms and these atoms will have fewer numbers of direct neighbours leading to lower coordination numbers that makes them highly unstable thereby increasing chemical reactivity. The catalytic activity of small gold particles is first discovered by Haruta et al and nanogold found practical applications in catalysis, for e.g., as ‘odour eaters’ in bathrooms or for low temperature oxidation of CO to CO₂.⁶⁰ As surface to volume ratio increases with decrease in size, numerous properties like melting and phase transition temperature also decreases with reduction in size. How reduction in size lead to an increase in the number of surface atoms is shown in the figure shown below.







Full shell clusters		Total number of atoms	Surface atoms (%)
1 shell		13	92
2 shells		55	76
3 shells		147	63
4 shells		309	52
5 shells		561	45
6 shells		1415	35

Fig 1.6: Pictorial representation of reduction in % of surface atoms as size increases (adapted from *Chem. Soc. Rev.* **2006**, 35, 1162 – 1194).

1.5.1.2. Quantum confinement effects

Size effects contribute to the fascinating properties exhibited by the nanomaterials and these arises from the magic numbers of atoms in metal clusters, quantum mechanical effects at small sizes and from size scaling effects applicable to larger nanostructures. The highest occupied molecular orbital (HOMO) of a molecular system is replaced by Fermi energy, E_F of the free electron model in the case of bulk metals. E_F depends only on the density $\rho = \frac{N}{V}$ of the electrons (N = number of electrons, V = volume) and Fermi energy is independent of particle size. Assume all levels upto E_F are occupied by a total of N electrons, and the average level spacing can be estimated as $\delta \cong \frac{E_F}{N}$, where δ is the Kubo

gap that is inversely proportional to volume, $V=L^3$ (L-side length of the particle) and directly proportional to E_F , $\delta \propto E_F, \left(\frac{\lambda_F}{L}\right)^3$. Here λ_F is the wavelength of electron energy E_F and is of the order of interatomic distances. These are based on the assumptions of wavecharacter of electrons and for the model of an electron in a box of side length, L only discrete values of energy are allowed i. e. the ratio $2\frac{L}{\lambda}$ is an integer. The separation values δ becomes larger with smaller values of L. How energy levels are changing from a molecular system to bulk metal based on density of state as a function of energy are shown below. In the case of bulk metals from the infinite number of nondifferentiated electrons the energy levels are merged together to form bands and in the case of molecules with lesser electrons, discrete energy levels are forming.

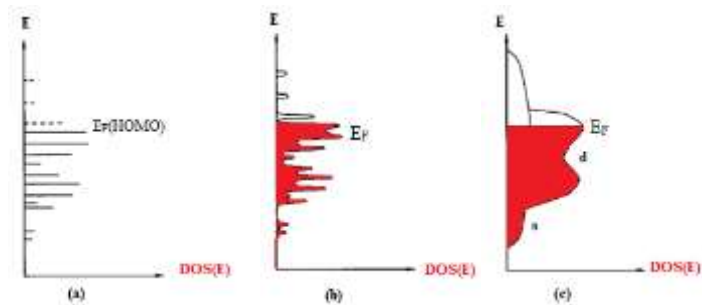


Fig 1.7: Pictorial representation of formation of a band structure (a) from a molecular state (b) from a nanosized particle (c) the fully developed band structure consisting of s and d bands (adapted from *Nanoscale materials in chemistry*, page18)

When the particle size is reduced to nanorange the particles behave like individual atoms due to the formation of discrete energy levels rather than the continuum in the energy levels. The DOS within a band is basically proportional to the number of atoms of an ensemble. The band

width is ~a few eV. Thus, Density Of States (DOS) is on the order of number of atoms per eV, which is very large for a bulk amount of matter, but low for small clusters. The average spacing of successive Quantum levels, δ , known as Kubo gap is given by $= 4E_F/3n$ where E_F is the Fermi Energy of the bulk metal and n is the number of valence electrons in the nanoparticle. Because of the presence of Kubo gap, properties such as electrical and magnetic susceptibility exhibit quantum size effects. Discreteness of energy levels also brings about changes in the special features, especially those related to valence band. When an electron gets thermally excited across the Kubo gap, at low temperatures insulator becomes semiconductor and at higher temperatures, to a metal. Thus, non-metal to metal transition can take place within a single incompletely filled band or when two bands begin to overlap because of band broadening.

Due to confinement of electron wave functions in one, two or three physical dimensions of the nanomaterials, they exhibit both size and shape dependent properties. Some of them are given below

1.5.2. Structural properties

nanomaterials show different lattice parameters eventhough they may or may not have same crystal structure as its bulk one. For example, nanometer sized gold and aluminium are icosahedral where as they are face centered cubic in bulk. Also due to very large electrostatic forces and short-range core-core repulsion, the inter atomic spacing in nanomaterials decreases than in bulk. ⁶¹

1.5.3. Thermal properties

As size reduced there will be increase in surface energy and change in inter atomic spacing which will have marked effect on melting properties of nanomaterials. For example, the melting point of gold nanoparticle decreases rapidly as size reduces.⁶²

1.5.4. Chemical properties

nanoscale materials have greater ionization energies than for the corresponding bulk one. There will be enormous change in chemical reactivity of nanomaterials due to which nanoscale materials find greater application in catalysis.⁶³

1.5.5. Mechanical properties

Mechanical properties of nanoparticles exhibit variations depending on the nature of association or bonding between the individual atoms. Mechanical properties are also affected by several other factors such as grain boundaries, point defects, dislocations, etc. Such defects are generally high for nanomaterials and show increase due to the non-thermal equilibrium, causing modifications in the mechanical properties.⁶⁴

1.5.6. Magnetic properties

Magnetic nanoparticles with reduced dimensions exhibit superparamagnetism.⁶⁵ In the case of bulk ferromagnetic materials in order to minimize magnetostatic energy of the system spontaneously magnetized domains will be formed. However, magnetic domain formation is not energetically favoured in the case of nanoscale

materials. In such case all spins will be oriented in one direction. In such a case, the coercivity, H_c is described by the equation

$$H_c = \frac{2K}{M_s} \left[1 - \frac{T}{T_B} \right] \quad (1.1)$$

Here M_s stands for the saturation magnetization as a result of the applied magnetic field, T_B is the blocking temperature, and K is the anisotropy constant. In the presence of the applied field, the magnetic moments may orient in a unique direction in the case of anisotropic systems. Anisotropy may also arise as a result of the nanoparticle shape, applied stress and by the inherent crystal structure. The temperature above which the thermal energy is able to set the orientation of magnetic moments free is known as the blocking temperature. Below the blocking temperature, they are frozen. The single domain nanoparticles generally do not exhibit any coercivity or hysteresis. These are known as superparamagnetic particles. In these systems, the spins are oriented in a single direction and they switch to the opposite direction in a coherent manner. The switching time is provided by the equation

$$t = \tau_0 e^{-KV/kT} \quad (1.2)$$

This happens generally in a time scale of femtoseconds.

1.5.7. Electronic properties

When atoms form lattice, the discrete energy levels of the atoms are smudged out into energy bands. When a metal particle having bulk properties is reduced in size to a few hundred atoms, the DOS in the conduction band and the top band containing electrons change dramatically. The continuous DOS in the band is replaced by a set of discrete energy levels, which may have energy level spacing larger than

the thermal energy and a gap opens up.⁶⁶ The small cluster is analogous to a molecule having discrete energy level with bonding and antibonding orbitals. Eventually a size is reached where the surface of the particle is separated by distances in the order of the wavelengths of the electrons.

In this situation the energy levels can be modeled by the quantum-mechanical treatment of a particle in a box. This is referred to as quantum size effects. The emergence of new electronic properties can be understood in terms of the Heisenberg uncertainty principle, which states that the more the electron is spatially confined, broader will be its range of momentum. The average energy will not be determined so much by the chemical nature of atoms, but mainly by the dimension of the particle.

1.5.8. Optical properties

The optical properties of nanoparticles have been extensively investigated in recent years. When an electromagnetic wave passes through a metal particle, the electronic and vibrational states get excited. The optical interaction induces a dipole moment that oscillates coherently at the frequency of the incident wave. The frequency of this oscillation depends on the electron density, its effective mass, the shape and size of the charge undergoing oscillation. There can be other influences such as those due to other electrons in the system. The restoring force arises from displacement of the electron cloud relative to the nuclei, which results in the oscillation of the electron cloud relative to the nuclear framework. The collective oscillation of the free conduction electrons is called 'Plasmon resonance' of the particle.⁶⁷ In this resonance, the total electron cloud moves with the applied field.

Mie explained this optical phenomenon in terms of the well-known Maxwell's equations. When an electromagnetic radiation interacts with uniformly sized spherical particles in a particular medium, a reduction is observed in the intensity. One should specially consider the dielectric constant of these nanoparticles. In fact, Mie theory does not account for the interactions between the individual particles. Thus, the extinction cross section for spherical particles with radius R , C_{ext} is provided by the equation

$$C_{ext} = \frac{24\pi^2 R^3 \epsilon_m^{\frac{3}{2}}}{\lambda} \frac{\epsilon_2(\omega)}{(\epsilon_1(\omega) + 2\epsilon_m)^2 + \epsilon_2^2(\omega)} \quad (1.3)$$

Mie provided a successful explanation for the observation of an absorption band for metal nanoparticles in visible region of the electromagnetic spectrum. In order to explain the observed shift in the plasmon bands for very small nanoparticles (below 10 nm), the dielectric constant needs consideration. In the case of metals, the dielectric response of electron is well described by the Drude model.

Various models are proposed to explain the optical properties of metal nanoparticles and are discussed in the following sections.

1.6. Plasmonics

The oscillations of the surface charge density in metallic NP, commonly named localized surface plasmons (LSPs) is arising as a result of the collective oscillations of conduction band electrons under the constraints imposed by the physical boundaries of the NP geometry. In comparison to the surface modes propagating along metal dielectric interface, LSP modes are stationary oscillations of the surface charge density at optical frequency along the metal boundaries of a metallic particle. Surface

Plasmon Polaritons are surface charge density waves that propagate at a metal-dielectric interface and light cannot be couple directly to Plasmon excitation of a flat, metal surface since energy and momentum cannot be conserved simultaneously.^{68,69}

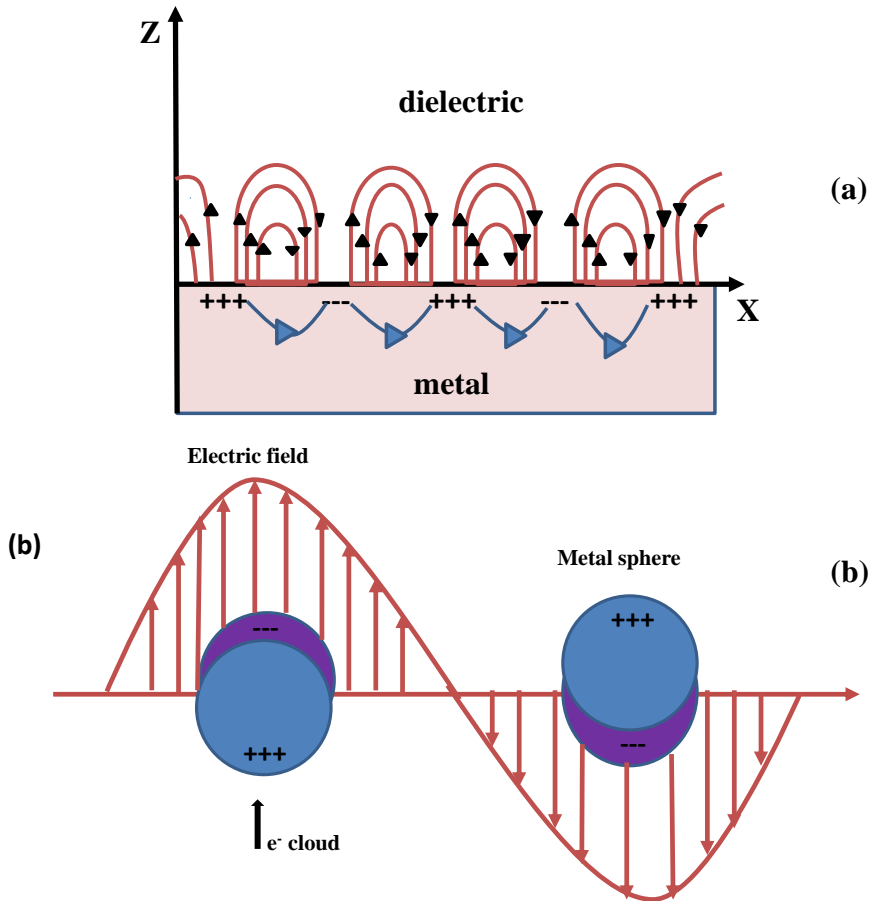


Fig 1.8: Schematic diagram; (a) propagating surface Plasmon resonance, (b) localized surface Plasmon resonance (adapted from 41. Kelley, K. S.; Coronado, E.; Zhao, L. L.; Schatz, G. C., *J. Phys. Chem. B* **2003**, *107*, 668 – 677).

The optical response of the LSP in a metallic particle can be described through the particle polarizability α , that relates the incoming EF, E_0

with the electric dipole moment $\mathbf{p} = \alpha\mathbf{E}_0$. Generally, polarizability of a metallic object is a frequency dependent magnitude that depends on the dielectric function $\varepsilon(\omega)$ of the metal and on the surrounding medium, as well as on the particle geometry.⁷⁰ A localized surface Plasmon resonance is associated with the polarizability α of the metal NP as a function of frequency (wavelength).

The EM coupling of light to the LSP resonances can be understood in the context of simultaneous conservation of energy and momentum. In a metallic NP, the finite geometry act as a source of momentum, generating a stationary surface charge density wave that is localized at the particle. For a particle of generic size a , the momentum provision $\Delta k = n \frac{2\pi}{a}$ where n is an integer. In this case a discrete set of LSP modes of order n that couple effectively to light are possible. In analogy to other ranges of the EM spectrum, these localized EM surface modes are commonly referred to as optical antenna resonances. The finite geometry of the metal NP essentially determines their optical properties. It does not only allow for coupling to external light but it also provides a means to tune the energies of the Plasmon excitations and to localize and enhance optical fields in the vicinity of the particle. All these aspects of the metal NP make them key building blocks in nano-optics.

1.7. Theories of Plasmonics

1.7.1. Mie theory

As mentioned earlier, it was Gustav Mie who presented an analytical solution to the Maxwell's equations to explain the scattering and absorption of light by spherical particles.⁷¹ (For very small particles $d \ll \lambda$, Mie scattering agrees with the more familiar Rayleigh scattering).

Finding the scattered field produced by a plane wave incident on a homogeneous conducting sphere results in the following total scattering, extinction and absorption cross-sections.

$$\sigma_{sca} = \frac{2\pi}{|k|^2} \sum_{L=1}^{\infty} (2L+1) (|a_L|^2 + |b_L|^2) \quad (1.4)$$

$$\sigma_{ext} = \frac{2\pi}{|k|^2} \sum_{L=1}^{\infty} (2L+1) [R_E(a_L + b_L)] \quad (1.5)$$

$$\sigma_{abs} = \sigma_{ext} - \sigma_{sca} \quad (1.6)$$

Here k is the wavevector and L are integers and based on its values it represents dipole, quadrupole and higher multipoles of the scattering. In the above expressions, a_L and b_L are the following parameters, composed of the Riccati-Bessel functions ψ_L and χ_L :

$$a_L = \frac{m\psi_L(mx)\psi'_L(x) - \psi'_L(mx)\psi_L(x)}{m\psi_L(mx)\chi'_L(x) - \psi'_L(mx)\chi_L(x)} \quad (1.7)$$

$$b_L = \frac{\psi_L(mx)\psi'_L(x) - m\psi'_L(mx)\psi_L(x)}{\psi_L(mx)\chi'_L(x) - m\psi'_L(mx)\chi_L(x)} \quad (1.8)$$

Here, $m = \frac{\tilde{n}}{n_m}$, where $\tilde{n} = n_R + in_I$ corresponds to the complex refractive index of the metal, and n_m denotes real refractive index of the surrounding medium. Also, $x = k_m r$, the radius of the particle is represented here as r . $k_m = \frac{2\pi}{\lambda_m}$ corresponds to wavenumber in the medium rather than vacuum wavenumber.

If the NP is assumed to be very small as compared to the wavelength, $x \ll 1$, in this case the Riccati-Bessel functions can be approximated by power series. Following Bohren and Huffmann, and keeping only terms to order x^3 , equations 1.7 and 1.8 simplifies to:

$$a_1 \approx -\frac{i2x^3}{3} \frac{m^2-1}{m^2+2} \quad (1.9)$$

$$b_1 \approx 0$$

And higher order a_L and b_L are zero. To find the real part of a_1 substitute $m = \frac{(n_R+in_I)}{n_m}$ into equation (1.9)

$$a_1 = -\frac{i2x^3}{3} \frac{n_R^2 - n_I^2 + i2n_R n_I - n_m^2}{n_R^2 - n_I^2 + i2n_R n_I + 2n_m^2} \quad (1.10)$$

Consider the complex metal dielectric function $\tilde{\epsilon} = \epsilon_1 + i\epsilon_2$ with the following relations:

$$\epsilon_1 = n_R^2 - n_I^2 \quad (1.11)$$

$\epsilon_2 = 2n_R n_I$, also consider the medium's dielectric function: $\epsilon_m = n_m^2$.

These substitutions lead to:

$$a_1 = \frac{2x^3}{3} \left[\frac{-i\epsilon_I^2 - i\epsilon_I \epsilon_m + 3\epsilon_2 \epsilon_m - i\epsilon_2^2 + i2\epsilon_m^2}{(\epsilon_1 + 2\epsilon_m)^2 + (\epsilon_2)^2} \right] \quad (1.12)$$

Substitution of equation (1.12) into equation (1.4) and taking the dipole term only, yield the expression for NP Plasmon resonance

$$\sigma_{Scat} = \frac{18\pi\epsilon_m^{3/2}}{\lambda} \frac{\epsilon_2(\lambda)}{[\epsilon_1(\lambda)+2\epsilon_m]^2+\epsilon_2(\lambda)^2} V \quad (1.13)$$

Where V is the particle volume. Another expression for scattering cross-section is

$$\sigma_{Scat} = \frac{32\pi^4\epsilon_m^2V^2}{\lambda^4} \frac{(\epsilon_1-\epsilon_m)^2+(\epsilon_2)^2}{(\epsilon_1+2\epsilon_m)^2+(\epsilon_2)^2} \quad (1.14)$$

The extinction cross-section will be maximized when the denominator in equation (1.14) is minimized, a condition that will be met when $\epsilon_1 = -2\epsilon_m$.

1.7.2. Gans theory

Mie theory as formulated above is strictly applicable only to spherical particles. For spheroidal particle, Richard Gans put forward a new theory known as Gans theory and it is based on Mie theory with some modifications based on small particle approximation.⁷² He found that the absorption cross section for a prolate spheroid, analogous to that in equation 1.14 above for a sphere is,

$$\sigma_{abs} = \frac{\omega}{3c} \epsilon_m^{3/2} V \sum_j \frac{(1+P_j^2)\epsilon_2}{\{\epsilon_1+[(1-P_j)/P_j]\epsilon_m\}^2+\epsilon_2^2} \quad (1.15)$$

Here the sum over j considers the three dimensions of the particle. P_j Includes P_A, P_B, P_C termed depolarization factors, for each axis of the

particle, where $A > B = C$ for a prolate spheroid. The depolarization factors are given as

$$P_A = \frac{1-e^2}{e^2} \left[\frac{1}{2e} \ln \left(\frac{1+e}{1-e} \right) - 1 \right] \quad (1.16)$$

$$P_B = P_C = \frac{1-P_A}{2} \quad (1.17)$$

Here e is the factor given below and it include the term R , representing aspect ratio.

$$e = \left[1 - \left(\frac{B}{A} \right)^2 \right]^{1/2} = \left(1 - \frac{1}{R^2} \right)^{1/2} \quad (1.18)$$

There are two peaks in the extinction spectrum as per the equation 1.13 one with greater intensity is known as longitudinal plasmon peak and the other with lesser intensity as transverse peak.

1.7.3. Drude dispersion model

Theoretical model- Drude's model (1900) is based on the kinetic theory of electrons in a metal which assumes that the material has motionless positive ions and a non-interacting electron gas.⁷³ This simple model uses classical mechanical theory of free electrons. It was constructed in order to explain the transport properties of conduction electrons in metals (due to intra-band transitions in a quantum-mechanical interpretation), conductive oxides and heavily doped semiconductors.

Since the conduction electrons are considered to be free, Drude oscillator is an extension of the single Lorentz oscillator to a case where the restoring force and the resonance frequency are null ($\Gamma_0=0, \omega_t = 0$)

The equation of motion is,

$$m \frac{d\vec{v}}{dt} + m\Gamma_d \cdot \vec{V} = -e \cdot \vec{E} \quad (1.19)$$

Where $m \frac{d\vec{v}}{dt}$ is the acceleration force; m is the mass of the oscillator (here the electron) and V is the speed of the gas of electron.

$m\Gamma_d$ is the frictional force;

The term $-e \cdot \vec{E}$ is the electric force; it contains the term $E = E_0 e^{i\omega t}$ which is the electric field of pulsation ω and e is electric charge.

The solution of the previous equation is given by the following expression for oscillation amplitude,

$$\vec{V}(\omega) = \vec{V}_0 e^{i\omega t} = \frac{-e \vec{E}_0}{m i\omega + \Gamma_d} \quad (1.20)$$

The conduction density of current J_c corresponding to the movement of the N electrons per unit volume is,

$$\vec{J}_c(\omega) = -Ne\vec{V} = \frac{Ne^2}{m(\Gamma_d + i\omega)} \vec{E} \quad (1.21)$$

The displacement density of current of vacuum is expressed by

$$\vec{J}_d = \frac{\partial \vec{D}}{\partial t} = i\omega \varepsilon_0 \vec{E} \quad (1.22)$$

Where D is the electric displacement of vacuum $D = \varepsilon_0 \vec{E}$. The total density of current J is given by

$$\vec{J}(\omega) = \vec{J}_c + \vec{J}_d = \left[\frac{Ne^2}{m(\Gamma_d + i\omega)} + i\omega\varepsilon_0 \right] \vec{E} \quad (1.23)$$

Assuming that the plasma can also be characterized by identifying the total density of current to a global displacement current $D_{tot} = \varepsilon_0 \varepsilon_r E$. A new expression for the total density of current is then given by,

$$\vec{J}(\omega) = \left[\frac{Ne^2}{m(\Gamma_d + i\omega)} + i\omega\varepsilon_0 \right] \vec{E} = i\omega\varepsilon_0 \tilde{\varepsilon}(\omega) \cdot \vec{E} \quad (1.24)$$

By simplifying the last expression, it is possible to deduce Drude's dielectric function $\varepsilon(\omega)$ given by the following equation.

$$\tilde{\varepsilon}(\omega) = 1 - \frac{Ne^2}{m\varepsilon_0} \cdot \frac{1}{(\omega^2 - i\Gamma_d\omega)} = 1 - \frac{\omega^2 p}{-\omega^2 + i\Gamma_d\omega} \quad (1.25)$$

Note that for $\omega \rightarrow \infty$, $\varepsilon(\infty) \rightarrow 1$, then it is possible to rewrite the dielectric function as

$$\tilde{\varepsilon}(\omega) = \varepsilon(\infty) - \frac{\omega^2 p}{-\omega^2 + i\Gamma_d\omega} \quad (1.26)$$

The real $\varepsilon_1(\omega)$, and the imaginary $\varepsilon_2(\omega)$ parts of the dielectric function are given by

$$\varepsilon_1(\omega) = 1(\varepsilon(\infty)) - \frac{\omega^2 p}{\omega^2 + \Gamma^2} \quad (1.27)$$

$$\text{And } \varepsilon_2(\omega) = \frac{\omega^2 p \Gamma}{\omega(\omega^2 + \Gamma^2)} \quad (1.28)$$

Behaviour of Drude dielectric function

1. If $\omega < \omega_p$ then the real part of ε is negative. Any electrical field cannot penetrate the metal that is totally reflective. The optical constants of the material are complex.
2. If $\omega = \omega_p$, then the real part of the dielectric function is zero. This means that all electrons oscillate in phase throughout the material propagation length.
3. If $\omega > \omega_p$ the reflectivity decreases and the metal becomes transparent. The refractive index of the material is almost real.
4. When $\omega^2 \gg \Gamma_d^2$ then $\varepsilon_r(\omega) = 1 - \left(\frac{\omega_p^2}{\omega^2}\right)$ (1.29)

The imaginary part of the dielectric function can be approximated by $\varepsilon_i(\omega) = \left(\frac{\omega_p^2 \Gamma}{\omega^2}\right)$ and there is no absorption at the high frequency limit.

$$\omega_p = \sqrt{\frac{Ne^2}{m\varepsilon_0}} \quad (1.30)$$

1.7.4. Effective medium theory

SPR of metal NP strongly depend upon the close-packing of NP, and if the metal NP in a solution is not isolated, there is coupling of plasmons of one particle with other. Mie theory cannot be applied to concentrated nanoparticle solutions since it is for very dilute solution and in such cases interparticle coupling is stronger than the coupling within the surrounding medium. The effective medium theory is successful for explaining the optical absorbance behaviour of the metal NP present in a closely packed assembly.⁷⁴ This is applicable strictly in the quasistatic

limit ($2R \ll \lambda$) along with very small interplanar distances but can be generalized to various shapes of the particles. According to Maxwell Garnett theory, the optical properties of the small particles mainly depend upon two contributions: the properties of the particles acting as well-isolated individuals and the collective properties of the whole ensemble. The aggregated clusters are characterized by their correlation length of spatial order, filling factors, details of the structure of the geometric ordering etc. Here we have to consider a statistical average over a large number of aggregates and the averaged volume fraction, f of the separated clusters in the sample i.e., the filling factor is introduced to describe the topology as

$$f = \frac{V_{cluster}}{V_{sample}} \quad (1.31)$$

For an aggregate of spherical geometry, the filling factor is given by

$$f = \frac{NR^3}{r^3} \quad (1.32)$$

Where r is the radius of the spherical aggregates.

In a medium of aggregates of metal spheres, dielectric function of a single spherical particle will be the sum of all contribution to the electrical polarization including those from retarded electrodynamics in the neighbouring particles and the effective EF at the position of a given particle by applying Lorentz theory is given as

$$E_{local} = E_0 + E_d + E_S + E_{near} \quad (1.33)$$

E_0 = external field, E_d = field due to charges at the external surface, E_S = field due to dipoles inside the sphere. The above equation can be written as

$$E_{local}=E_{Maxwell} + E_S + E_{near} \quad (1.34)$$

Where $E_{Maxwell}$ is the incident field (i.e., the average field, simply denoted as E) in the matrix, i.e., the external field plus the field from polarization charges at the surface of the Lorentz sphere. For a filling factor $f > 10^{-3}$, collective properties became important. Under such situation, $E_{near}=0$, due to cancelling of scattering fields of all the particles within the Lorentz sphere. The field due to polarization charges around the sphere, E_S , is given by

$$E_S = \int_0^\pi \left(\frac{P \cos\theta}{R^2} \right) \cos\theta (2 R^2 \sin\theta) d\theta \quad (1.35)$$

$$= \frac{4\pi}{3} P \quad (1.36)$$

The local field related to average field (E) and polarization (P) as

$$E_{local} = E + \frac{4\pi}{3} P \quad (1.37)$$

The dipole moment of an atom or particle can be expressed in the form

$$\mu = \alpha E_{local} \quad (1.38)$$

And the polarization (P) in the form

$$P = \sum_i N_i \mu_i = \sum_i N_i \alpha_i E_{local}(i) \quad (1.39)$$

Where N_i and α_i are the number density and the polarizability of the i^{th} particle species. Putting the value of E_{local} in equation above we get

$$P = \sum_i N_i \mu_i = \sum_i N_i \alpha_i \left(E + \frac{4\pi}{3} P \right) \quad (1.40)$$

Then, the susceptibility (χ) is defined by

$$\chi = \frac{P}{E} = \frac{\sum_i N_i \alpha_i}{1 - \frac{4\pi}{3} \sum_i N_i \alpha_i} \quad (1.41)$$

The polarizability of a spherical particle with permittivity ε and radius R is defined as

$$\alpha = \frac{\varepsilon - \varepsilon_m}{\varepsilon + 2\varepsilon_m} R^3 \quad (1.42)$$

Based on effective medium theory the system may be replaced by an effective medium and it acts like a homogeneous material and can be described by the effective dielectric function,

$$\varepsilon_{eff} = \varepsilon_{1,eff} + i\varepsilon_{2,eff} \quad (1.43)$$

The Clausius-Mossotti relation describes the link between the macroscopic observable ε_{eff} and macroscopic parameter α as,

$$\frac{\varepsilon_{eff} - \varepsilon_m}{\varepsilon_{eff} + 2\varepsilon_m} = \frac{4\pi}{3} \sum_i N_i \frac{\varepsilon - \varepsilon_m}{\varepsilon + 2\varepsilon_m} R^3 \quad (1.44)$$

After introducing the filling factor, f the above equation can be expressed as

$$\frac{\varepsilon_{eff} - \varepsilon_m}{\varepsilon_{eff} + 2\varepsilon_m} = f \frac{\varepsilon - \varepsilon_m}{\varepsilon + 2\varepsilon_m} \quad (1.45)$$

Above equation is of the form Lorentz-Lorenz formula and equation (1.45) changed into the form

$$\varepsilon_{eff} = \varepsilon_m \frac{1+2f\Lambda}{1-f\Lambda} \quad (1.46)$$

$$\text{Where } \Lambda = \frac{1}{\varepsilon_m} \frac{\varepsilon - \varepsilon_m}{\varepsilon + 2\varepsilon_m} = \frac{\alpha}{3\varepsilon_0 \varepsilon_m V} \quad (1.47)$$

When dealing with a material composed of two equal inclusions, the Maxwell-Garnett formula is changed into the form

$$\frac{\varepsilon_{eff} - \varepsilon_m}{\varepsilon_{eff} + 2\varepsilon_m} = f_1 \frac{\varepsilon_1 - \varepsilon_m}{\varepsilon_1 + 2\varepsilon_m} + f_2 \frac{\varepsilon_2 - \varepsilon_m}{\varepsilon_2 + 2\varepsilon_m} \quad (1.48)$$

There is only one resonance at $\varepsilon = -2\varepsilon_m$ corresponding to the SPR at $\omega = \frac{\omega_p}{(1+2\varepsilon_m)^{\frac{1}{2}}}$ of an isolated metal NP. The absorption spectrum is then given by the absorption constant, $\gamma_a(\omega)$

$$\gamma_a(\omega) = \frac{\omega}{n_r c} I_m\{\varepsilon_{eff}\} = \frac{4\pi k}{\lambda} \quad (1.49)$$

$$= \frac{2\omega}{c} \sqrt{\frac{-\varepsilon_{1,eff}^2}{2}} + \sqrt{\frac{\varepsilon_{1,eff}^2 + \varepsilon_{2,eff}^2}{2}} \quad (1.50)$$

The Maxwell-Garnet theory is only valid for dilute ensembles of particles and if the particles are close enough for their near-field to interact, the theory breaks down.

1.8. Applications of metallic nanoparticles

1.8.1. Biological and biomedical applications

There are several nanoscale structures that find application in a broad range of biological and biomedical applications.⁷⁵⁻⁷⁹ Quantum dots, due

to their size dependent fluorescence are useful for biological labelling and detection.⁸⁰⁻⁸¹ Magnetic NPs are used for cell sorting, MRI, drug delivery and magnetic hyperthermia therapy.⁸²⁻⁸⁴ Carbon nanotubes are used for photothermal therapy and drug delivery.⁸⁵⁻⁸⁷ Since it is possible to tune the properties of metal NP by varying size, shape, composition and because of higher synthetic control, metal NPs are very good candidates for biomedical applications, among which gold NP are especially promising due to their biocompatibility and ability for bioconjugation. Due to its strong SPR, Au NP also find applications in light scattering imaging and Sokolov et al showed that by conjugation with the anti-epidermal growth factor receptor (anti-EGFR), Au NP can target cancer cells and can be visualized by the SPR of nanoparticles.⁸⁸ Huang et al reported that gold nanorods (NR) conjugated anti-EGFR antibodies can also target cancer cells.⁸⁹ Au NR also exhibit two photon luminescence (TPL), and Wang et al demonstrated that single NR can be imaged *in vivo* in the mouse ear blood vessel.⁹⁰ Durr et al applied TPL for the molecular imaging of cancer cells.⁹¹ In addition to light scattering Au NP absorb light strongly and light is converted to heat and this makes them highly useful for photothermal therapy.⁹² Pitsillides et al first reported the photothermal therapy of lymphocytes and El-syed et al demonstrated the selective photo thermal therapy of cancer cells, *in vitro*, using EGFR antibodies.^{93,94} Metal NPs also find extensive applications in biosensing and in monitoring molecular events.⁹⁵⁻⁹⁸ Mirkin et al reported that mercapto alkyl oligo nucleotide modified Au NP probes generate cross-linked polymeric aggregates that signalled hybridization with complimentary oligonucleotide target via colour

change.⁹⁹ A system performing multiplexed detection of oligonucleotide targets has been reported by Cao et al.¹⁰⁰ Li and Rothberg et al has reported another colorimetric hybridization assay that uses unmodified/ unfunctionized Au NP for sequence-specific detection of DNA.¹⁰¹ Colourimetric sensing due to protein- ligand interaction is studied by Tsai et al.¹⁰² Lan et al has reported Au NP/ enzymes-based biosensors that measure cellular glucose levels.¹⁰³

1.8.2. Catalytic applications

Eventhough bulk gold remained chemically inactive and act as an inert catalyst, nano-sized Au shows high catalytic activity and act as green catalyst.¹⁰⁴⁻¹⁰⁶ Catalytic reduction of dyes by silver NP supported on silica spheres was reported by Jiang et al and silver NP on silica spheres avoids flocculation of nanosized colloidal metal particles during a catalytic process in the solution.¹⁰⁷ Sharma et al reported p-Nitro phenol reduction employing biosynthesized Au NPs.¹⁰⁸ Mukherjee et al has shown that Au NP synthesised by auto reduction of the Au³⁺ ions with fumed silica was catalytically active in the hydrogenation of cyclohexene.¹⁰⁹ Pina et al has reviewed the recent development of the catalytic properties of gold in the selective oxidation of organic compounds.¹¹⁰

1.9. Raman spectroscopy

When a monochromatic light interacts with molecules, two types of scattering are possible. The first is the elastic scattering, known as Rayleigh scattering, where incident light and scattered light are having

same energy. For the second, the inelastic scattering known as Raman scattering, the scattered light is having either lower energy compared to incident light (Stokes Raman) or higher energy compared to incident light (anti-Stokes Raman). It was in 1928 that C V Raman and K S Krishnan discovered this important phenomenon.¹¹¹ The branch of spectroscopy which deals with inelastic scattering of radiation was later termed as Raman spectroscopy and it provides unique vibrational signature of the molecule. Raman spectroscopy is a non-destructive technique and it can be used for the analysis of solid substances, liquids or gases but due to the very low Raman scattering cross section, it is a weak technique.¹¹²⁻¹¹⁵ This is particularly true for biomolecular systems that contain relatively small atoms. The energy of a photon, E is expressed as

$$E = h\nu \quad (1.51)$$

Where ν is the frequency of the incident radiation and h is the Plank constant (6.626×10^{-34} Js). The energy exchange is shown in the schematic diagram where $h\nu_i$ is the energy of the incident photon and $h\nu$ is the energy of the scattered photon. The letters n and v are used to represent electronic and vibrational levels ($n=0$ and $v=0$ is the ground states). ΔE is the energy difference that the photon can lose or gain during scattering. A photon with energy $h\nu_i$ excites a molecule from the ground state ($v=0$) to the virtual energetic level.

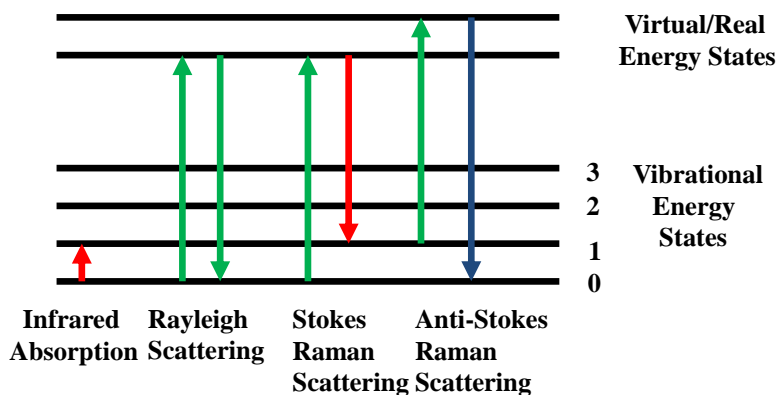


Fig 1.9: Schematic representation of Rayleigh, stokes and anti-stokes scattering (adapted from (ACS symposium series 1305) Matthew D. Sonntag - *Raman Spectroscopy in the Undergraduate Curriculum*, 2018)

In the first diagram showing Rayleigh scattering, molecule in the virtual energy state falls back to ground state and emits a photon with the same frequency of the incident photon ($h\nu = h\nu_i$). In the second figure showing Stokes scattering molecule from virtual energy state falls back to an excited vibrational state ($v=1$) and emits a photon with an energy lower than the incident photon. The energy of the scattered photon will be $h\nu = h\nu_i - \Delta E$. In the third figure representing Anti-Stokes scattering molecule is originally in the vibrational state ($v=1$) and it is excited to the virtual state by the incident photon. When it falls back to the ground state ($v=0$) it emits a photon with an energy higher than the incident light ($h\nu = h\nu_i + \Delta E$). The population of molecules at $v=0$ is much larger than that at $v=1$ (Maxwell-Boltzmann distribution law). Thus, Stokes lines are stronger than antistokes lines under normal conditions. The ratio between the populations N_1 and N_0 can be expressed as $\frac{N_1}{N_0} = e^{-\Delta E/kT}$ where N_1 and N_0 represent the population density in the vibrational levels $v=1$ and $v=0$ respectively; ΔE is the energy gap between the two

levels; T the temperature and k the Boltzmann constant. At room temperature, the population density N_1 can be neglected with respect to N_0 and this justified the higher intensity of Stokes lines. In the classical picture of Raman scattering, when light falls on a molecule, the size of the molecule is much smaller than the wavelength of light and the electric field of the wave can displace electrons of the molecule from its equilibrium position. Thus, inducing a dipole moment $\mu(t)$ given by

$$\mu(t) = \alpha * E(t) \quad (1.52)$$

Where α is the molecular polarizability and $E(t)$ the electric field of the incident radiation. If the molecule has its own internal vibration, the polarizability can be given as

$$\alpha = \alpha_0 + \alpha_k \sin(2\pi\vartheta_{\text{vib}}t) \quad (1.53)$$

The polarizability at the equilibrium is represented using the notation α_0 and the polarizability rate using α_k . E is the EF at the time t and it can also be written as

$$E(t) = E_0 \sin(2\pi\vartheta t) \quad (1.54)$$

By substituting (1.53) and (1.54) in (1.52)

$$\mu(t) = E_0 \sin(2\pi\vartheta t) [\alpha_0 + \alpha_k \sin(2\pi\vartheta_{\text{vib}}t)] \quad (1.55)$$

$$= E_0\alpha_0 \sin(2\pi\vartheta t) + E_0\alpha_k \sin(2\pi\vartheta t) \sin(2\pi\vartheta_{\text{vib}}t) \quad (1.56)$$

And rearranging the equation according to the relation

$$2\text{SinA}\text{SinB} = \text{Cos}(A-B) - \text{Cos}(A+B) \quad (1.57)$$

The complete equation for the dipole has the following form

$$\mu(t) = \alpha_0 E_0 \sin(2\pi\vartheta t) + \underbrace{\frac{E_0 \alpha_k}{2} \cos 2\pi(\vartheta - \vartheta_{\text{vib}})t}_{\text{Stokes}} - \underbrace{\frac{E_0 \alpha_k}{2} \cos 2\pi(\vartheta + \vartheta_{\text{vib}})t}_{\text{Anti-Stokes}}$$

(1.58)

The first term refers to Rayleigh scattering while the second and third terms denote respectively the Stokes and Anti-Stokes lines. The dipole oscillators with frequency ν , $\nu - \nu_{\text{vib}}$, $\nu + \nu_{\text{vib}}$. The Raman intensity (I_{Raman}) is strongly dependent on the number of particles of the sample (n), the scattering cross-section (σ) and the laser power (P). The frequency of the Raman shift $\bar{\nu}$ can be calculated knowing the force constant (k) and reduced mass (μ).

$$\bar{\nu} = \frac{1}{2\pi c} \sqrt{\frac{k}{\mu}} \text{ cm}^{-1} \quad (1.59)$$

The Raman polarizability α_R is a tensor that is determined by the structure of the molecule. To understand the connection between the scattered power and the Raman polarizability, we begin by considering the definition of scattering cross-section σ_{scat} :

$$\sigma_{\text{scat}} = P_{\text{scat}} / I_{\text{inc}} \quad (1.60)$$

where P_{scat} is the measured scattering power and I_{inc} is the intensity of the illumination. The scattering cross-section into any given direction is given by the differential scattering cross-section

$$\frac{d\sigma_{\text{scat}}(\Omega)}{d\Omega} = \frac{dP_{\text{scat}}(\Omega)}{d\Omega} / I_{\text{inc}} \quad (1.61)$$

Where Ω denotes the solid angle. In Raman scattering, each vibrational mode has its own differential scattering cross-section. The differential scattering cross-section is also a function of excitation wavelength. The differential Raman cross-section of the Raman molecule typically refers to the value measured at the direction that is perpendicular to both the incident light and the incident polarization, also known as the 90° configuration.

$$\frac{d\sigma_R}{d\Omega} = \frac{dP_R(90^\circ)}{d\Omega} / I_{\text{inc}} \quad (1.62)$$

If the Raman scattering from the molecule is modelled as that from linear dipole, the same differential Raman cross-section values are obtained for forward scattering and back scattering. For other detection directions, the radiation pattern of the molecule must be considered. Also from the dipole approximation the differential Raman cross-section can be related to the polarizability as:

$$\frac{d\sigma_R}{d\Omega} = \frac{dP_R(90^\circ)}{d\Omega} / I_{\text{inc}} \quad (1.63)$$

$$= \frac{\omega^4}{16\pi^2\epsilon_0^2c^4} |\alpha_R|^2 \quad (1.64)$$

By measuring the scattering at 90° and by making use of equations (1.63) and (1.64), the magnitude of Raman polarizability can be determined experimentally.

Theoretical calculations based on quantum mechanics, for Raman scattering, shows that the power of the scattered light P_s , is described by the product of the intensity of the incident photons, I_0 , and the the Raman cross-section, σ_R , given by

$$\sigma_R \propto \frac{1}{\lambda^4} \quad (1.65)$$

$$P_s \propto \frac{I_0}{\lambda^4} \quad (1.66)$$

It is seen that P_s is directly proportional to I_0 and inversely proportional to λ^4 .

1.10. Surface enhanced Raman spectroscopy

Due to very low scattering cross-section of Raman, for every 10^{10} incident photons, only about 1 photon will be Raman scattered. This limitation of Raman spectroscopy was arguably overcome by the discovery of enhanced signals from a solution of Pyridine over Silver electrode in 1974 by Fleischmann, Hendra and McQuillan of university of Southampton, UK. ¹¹⁶ Initially they thought that the enhanced spectra resulted from high surface area of the roughened electrode. When molecules are in close proximity to finely divided metals, the Raman signals get enhanced by a factor of about 10^6 . Since Raman spectra originating from the vibrational frequency of molecules that can act as a fingerprint for the identification of molecules and the enhanced spectra resulting from metal NP surfaces can replace other vibrational techniques utilizing non-destructive sample analysis method adopted in Raman. ^{117,118} Later in 1977, Jeanmaire and Van Duyne found out that the enhancement cannot be explained by the increase in the surface area alone. ¹¹⁹ Soon after, Albrecht and Creighton also reported similar results. ¹²⁰ The reports suggested that the enhancement can only be explained by an increase in the Raman scattering cross-section, to a degree of 10^5 to 10^6 times. Such an enhancement in the Raman scattering

cross section provides a new tool for studying the surface dynamics of various analyte molecules.¹²¹⁻¹²³

It is well established that a dipole is induced in the molecule as a result of its interaction with the radiation. This induced dipole moment is a product of the applied electric field and the molecular polarizability. Thus, for an enhancement in Raman signals, there should be an enhancement in either molecular polarizability or electric field or both. The first mode of the enhancement may be due to an interaction between the polarizability of the molecule can be larger ie $|\alpha_{\text{SERS}}| > |\alpha_{\text{R}}|$. This is known as ‘chemical enhancement’ component of SERS. The second enhancement originates from enhanced electric field due to plasmons excited on the metal; the local field at the position of the molecule can be larger. This is known as ‘electromagnetic enhancement’ of SERS. The electromagnetic enhancement involves two subprocesses (1) The field associated to the incident laser is enhanced due to surface Plasmon polariton on the surface of the metal NP, $(E(v_L))$ and (2) beam scattered by the sample $(E(v_S))$ is also enhanced through the same process. The intensity of the Raman signal is therefore enhanced by a factor of A^2 in each process.

$$I_{\text{SERS}} = I_{\text{Laser}} \cdot N \cdot \sigma_{\text{ads}}^{\text{R}} \cdot (A(\vartheta_L))^2 (A(\vartheta_S))^2 \quad (1.67)$$

1.10.1. Chemical enhancement mechanism of SERS

For chemical enhancement to operate there must be direct contact between the adsorbed molecules and the metal surface, thereby increasing the Raman cross-section.¹²⁴⁻¹²⁶ There is perturbation of electronic structure of the molecule by chemisorption or bond formation between molecule and surface. Electron transfer can take place from

filled orbitals of metal to molecule and vice versa leading to charge transfer complex formation. An early evidence for the observation of chemical enhancement is from the huge difference in the SERS intensities of two molecules CO and N₂ eventhough both show similar polarizabilities. A second evidence comes from potential dependent electrochemical experiment. Since changes in electrode potential results in changes in Fermi level of the metal, charge transfer process will depend on applied potential.

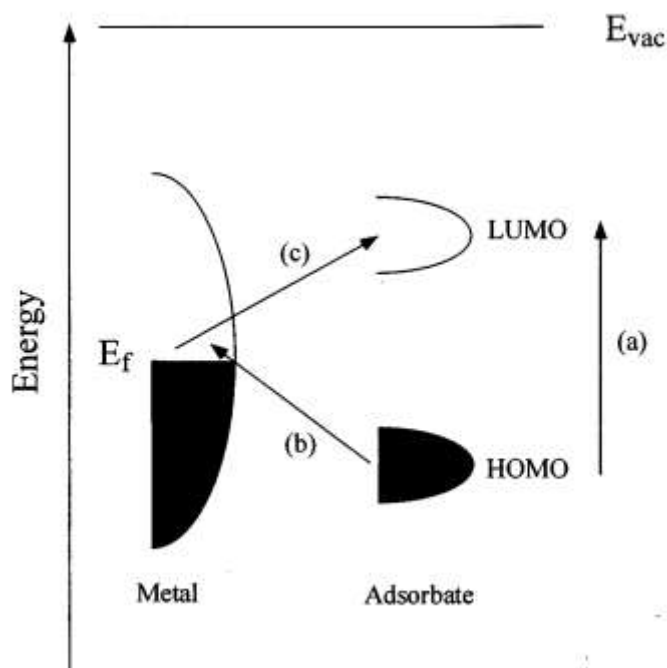


Fig 1.10: Charge transfer mechanism (adapted from *Chemical Society Reviews*, 1998, volume 27, 243)

1.10.2. Electromagnetic enhancement mechanism of SERS

Electromagnetic field of light at the surface can be greatly enhanced under conditions of surface Plasmon excitation; the amplification of

both the incident laser field and the scattered Raman field through their interaction with surface Plasmon resonance constitute the electromagnetic SERS mechanism.¹²⁷⁻¹³¹ The field induced at the surface of a sphere whose size is comparable to the wavelength of light, we can use electrostatic approximation and the field induced is related to the applied, external (laser) field by the equation (1.68).

$$E_{\text{induced}} = \{[\varepsilon_1(\omega) - \varepsilon_2]/[\varepsilon_1(\omega) + 2\varepsilon_2]\} \quad (1.68)$$

$$E_{\text{out}}(x, y, z) = E_0 \hat{Z} - \alpha E_0 \left[\frac{\hat{Z}}{r^3} - \frac{3Z}{r^5} (x\hat{X} + y\hat{Y} + z\hat{Z}) \right] \quad (1.69)$$

In equation (1.69) the distance from the centre of the particle is denoted by r , polarizability by α , and \hat{X} , \hat{Y} , and \hat{Z} corresponds to unit vectors. The incident field is represented by first term in equation 1.69 and induced dipole by second term. The induced dipole moment is $\mu_{\text{ind}} = \alpha E_0$, where $\alpha = g_d a^3$ and

$$g_d = \frac{\varepsilon_{\text{in}} - \varepsilon_{\text{out}}}{\varepsilon_{\text{in}} + 2\varepsilon_{\text{out}}} \quad (1.70)$$

Polarizability of metals dielectric function (ε_{in}) is represented by g_d and the external dielectric constant is represented by (ε_{out}).

To describe electromagnetic mechanism electrostatic approximation is a good one. Electric field surrounding the particle is given by the equation (1.69). Wavelength dependency of dielectric function leads to wavelength dependency of enhancement and this enhancement decreases with distance as r^{-3} . Here Raman scattering intensity shows a

strong dependency on E_0^2 , and the enhanced field experienced at a small metal sphere of radius a according to equation 1.68 is given below

$$|E_{\text{out}}|^2 = E_0^2 [1 - g]^2 + 3\cos^2\theta(2R_e(g) + |g|^2) \quad (1.71)$$

In equation 1.71 the angle between incident field vector and the vector representing molecular position on the surface is given by θ and when $\theta = 0^\circ$ or 180° a maximum value of $|E_{\text{out}}|^2$ will be there. At those angles molecule will be along the polarization direction. Electromagnetic enhancement can be explained as below. Since metal NP when irradiated with an incident radiation, it will undergo coherent oscillation with the incoming radiation and it enhances the dipole created in the molecule. The scattered radiation is inelastic in nature and energy is utilised for molecular vibration. There is a two fold enhancement i.e. both the incoming radiation and radiation scattered by the molecule will undergo enhancement and this overall EF can be expressed as

$$EF = \frac{|E_{\text{out}}|^2 |E'_{\text{out}}|^2}{|E_0|^4} = 4|g|^2 |g'|^2 \quad (1.72)$$

Where electric field and polarizability of scattered radiation is represented using primed symbols and for small inelastic scattering the value of polarizability g of both incident and scattered radiation can be taken as g and in equation 1.72 EF becomes equal to g^4 . Correspondingly E^4 enhancement occurs in the SERS.

1.11. Applications of surface enhanced Raman spectroscopy

Since SERS overcomes many inherent inefficiencies associated with Raman spectroscopy, it is an excellent analytical tool in myriad of areas and advancement of instrumentation techniques and synthesis and fabrication of excellent SERS substrates made analysis simple. It finds applications in broader areas such as forensic science, pharmaceutical industry, nanotechnology, art, semiconductors, bioscience¹³²⁻¹⁴¹ etc and single molecular detection ability of SERS is useful for label-free detection applications. Some of the applications of SERS are discussed below.

(a) Application of SERS in biosensing

SERS is successful in the detection, identification and characterization of biomacromolecules and many microorganisms. It also able to examine the structure, conformation and charge-transfer of bio molecules. Yan et al was able to get reproducible SERS signals from whole bacterial cells,¹⁴² and able to discriminate three tested bacteria species: *Escherichia coli*, *Bacillus cereus* and *Staphylococcus aureus*. For this nanoparticle cluster arrays fabricated on top of thin Au film using template guided self-assembly was employed. Temür et al also carried out SERS detection of E-coli using two different types of gold NP.¹⁴³ SERS as a tool for glucose sensing was first done by Shafer-Peltier et al and for this glucose molecule partitioned into an alkanethiol monolayer adsorbed on a silver film over nanosphere (AgFON) was used.¹⁴⁴ Lyandres et al also carried out glucose sensing using tri (ethylene glycol)-terminated alkanethiol (EG3) and decanethiol (DT)

SAMS on SERS active Ag FON surface. ¹⁴⁵ Kahraman et al has used SERS for the detection of E-coli and Staphylococcus cohnii by attaching Ag NPs and Au NPs onto the bacteria wall using layer-by-layer technique. ¹⁴⁶ Picoril et al has applied SERRS spectroscopy technique for getting vibrational spectra from the higher plant D1-D2- Cytochrome b559 photosystem II reaction centre complex and it was successful for selectively examining energy transfer and redox-active chromophores involved in the dynamics of the primary processes of photosynthesis. ¹⁴⁷ Electron transfer of Yeast Iso-I Cytochrome c on self-assembled monolayer-coated Ag electrodes was further studied by Feng et al. ¹⁴⁸ Application of SERS in gene diagnostics was carried out by Culha et al and he was successful in detecting BRCA1 breast cancer gene. ¹⁴⁹ Kaminska et al studied the protein interactions using SERS and he used chemically bound Au NP arrays on Si for this. ¹⁵⁰ Isola et al first reported the use of SERS in the detection of 'gag' gene sequence of HIV. ¹⁵¹

(b) Application of SERS in the analysis of NP in the environment

Due to the expansion of nanotechnology, products based on NP are widely used by mankind and toxicity it causes to human health and environment is an important issue to consider. SERS is acting as a versatile tool for the detection of SERS active NPs (Ag and Au). Lahr et al demonstrated that it is possible to monitor the behaviour of Au NPs and Ag NPs in microfluidic paper based analytical device and it can be related to environmental NP detection. ¹⁵² Han et al evaluated the oxidation of Ag NPs exposed to ambient air and a controlled ozone

environment under uv irradiation and correlated it with SERS enhancement factors.¹⁵³

(c) Spectroelectrochemistry and catalysis

SERS act as an excellent tool for monitoring surface chemistry, finding reaction intermediates, bond formation, bond cleavage thereby elucidating reaction mechanisms. Schlücker et al has reviewed applications of SERS for monitoring oxygen electroreduction on Bismuth modified Au surfaces and for monitoring Benzyl chloride reduction at a silver electrode.¹⁵⁴ He further examined the application of SERS in catalysis by monitoring Pt- catalyzed reaction in colloidal solutions. For this he has used Au/Pt/Au nanoraspberries and SERS spectra recorded for the Pt-catalyzed hybrid reduction of 4-nitrophenol to the corresponding aniline derivative.

1.12. Present study

To enhance the performance of SERS spectra, researchers have developed several geometries of metal nanoparticles based efficient SERS substrates that are highly useful due to its significant enhancement, excellent sensitivity and their finger printing ability. Metal NPs are beneficial because of their size, shape and tunability of surface plasmons. SERS has shown its notable applications in a wide range of areas including sensing, quality assurance and safety of food (detecting food adulteration), molecular dynamics on nanoparticle surface as well as for biomedical applications and cellular imaging techniques. Use of novel SERS substrate technologies and advancement

in nanoparticle synthesis shows this technique as a great promise for future. Since we are all facing the havoc of covid 19 pandemic the rapid and accurate diagnosis of infectious diseases using SERS based microdevices for the point of care (POC) diagnosis and Raman based approach for the analysis of saliva to discriminate current infection or a past infection method all pointed towards the importance of SERS studies. For a complete understanding of SERS phenomena, we must look into the mechanism of its origin and what are the parameters that are influencing a SERS signal. The work presented in this thesis is based on these points.

In chapter 1, we have presented a general introduction to nanoscience and nano technology, metal nanoparticles especially Gold and Silver, Surface plasmons, various theories of optical properties of metal NP, fundamentals of Raman spectroscopy, SERS spectroscopy and its applications. In chapter 2 detailed description of various analytical and instrumental methods used for the analysis of nanostructured materials are discussed.

Chapter 3 deals with wavelength dependent SERS studies of 1,4-BDT under three conditions-plasmon resonant, near resonant and off resonant using two excitation lines 532nm and 1064nm. A carbohydrate polymer based flexible cellulose acetate sheets were taken as matrix material for incorporating metal and alloy NP and preparation of SERS substrate is very simple and devoid of harsh chemicals thus making it a promising material. Networked metal and alloy NP were carefully deposited over Whatmann 41 filter papers. The main objective of the work was to investigate the correlation between laser excitation and plasmon

excitation on SERS spectra. These studies have shown that differences are arising with respect to relative intensities and spectral profile and it will be difficult to generalize the position of laser excitation and plasmon excitation wavelength on SERS enhancement. SERS studies of 1,2-BDT and 1,3-BDT on plasmonic metal and alloy and networked metal and alloy supported this. It also indicated composition dependence of SERS substrates on SERS spectra.

In chapter 4 preferential binding of different atoms of analyte molecules on metal and alloy NP was studied. For that analyte molecules with multiple binding sites such as MB, and R6B molecules were selected and SERS studies were carried out using 1064 nm. Since absorption of both dyes are off-resonant with respect to excitation wavelength, problem of fluorescence can be avoided. Here we have taken cotton fabric as the base material for incorporating NP since we know dyes will show superior binding on cloth. By careful examination of each and every peak in powder and SERS spectra we should be able to predict the orientation of these analyte molecules and surface dynamics of the same on SERS substrates.

In chapter 5 shape/morphology dependent SERS studies of 1,4-BDT, MB and R6B on substrates based on Silver nanoflowers of varying roughness and we studied how this slight change in flower morphology going to affect SERS spectra. In chapter 6, we present the morphological dependence of SERS using Au NPs of three different morphologies.

Chapter 7 presents the major conclusions and the future outlook of the work.

CHAPTER 2

ANALYTICAL METHODS

Several experimental techniques are employed for the characterization of the metal and alloy nanoparticles. Generally, these include spectroscopic, electron microscopic and X-ray diffraction techniques. While spectroscopic techniques, particularly the UV-Visible absorption spectroscopy is a unique tool for probing the optical properties and the electronic structural aspects of the metal and alloy NPs, electron microscopic techniques – Scanning electron microscopy (SEM) and Transmission electron microscopy (TEM) allows the direct observation of the metal NPs, their mode of aggregation and surface morphology. Electron diffraction studies provide the structural aspects of the nanoparticles. ¹⁵⁵⁻¹⁶¹

2.1. Electron microscopic techniques, SEM and TEM

Optical microscopy confronts several fundamental limits of detection when dealing with nanoparticle where the nanoparticles have sub-wavelength sizes. Typically, the resolution of optical microscopy is limited to half of the wavelength of the light used for the observation. On the other hand, the resolving power of an electron microscope is far better and is essential for viewing particles of smaller dimensions. In electron microscope, electrons are used as source of illuminating radiation due to its higher speed, smaller wavelength and better resolution. From the electron source (heated tungsten and field emission

filament) a high voltage electron beam is produced and this is accelerated towards the sample system by applying a sufficiently large positive potential. This is further focussed into a monochromatic beam of electrons using metal apertures and magnetic lenses. This beam of electrons interacts with the sample, resulting in the backscattering of electrons, production of Auger electrons, visible light, UV light and even X-rays.

2.1.1. Scanning Electron Microscope (SEM)

SEM is a highly useful technique that allows the study of the morphology of the metal nanostructures and often their sizes. A schematic representation of the functional part of SEM is provided in Figure 2.1. The first electron microscope was developed by Ernst Ruska in 1933. Based on the source/origin of the electrons - whether from a hot filament or a cold cathode- these are called ordinary SEM and FE-SEM. In SEM, electron interact with the positively charged nucleus of an atom undergo scattering at an angle greater than 90° and this type of electrons are called backscattered electrons. These backscattered electrons, due to their lower energy, can give information about topography of the sample surface only. Since the electron density depends on local electron density of the specimen, it provides information about the elemental composition of the sample. If the sample is non-conducting, it is coated with a thin layer of gold or platinum by sputtering to avoid charging effects and all this has to be placed inside a vacuum chamber to avoid oxidation and unnecessary interaction with air molecules. With the help of X-rays produced by the high energy electrons striking the sample we

can do elemental analysis of the sample and this technique is known as Energy dispersive analysis of X-rays (EDAX).

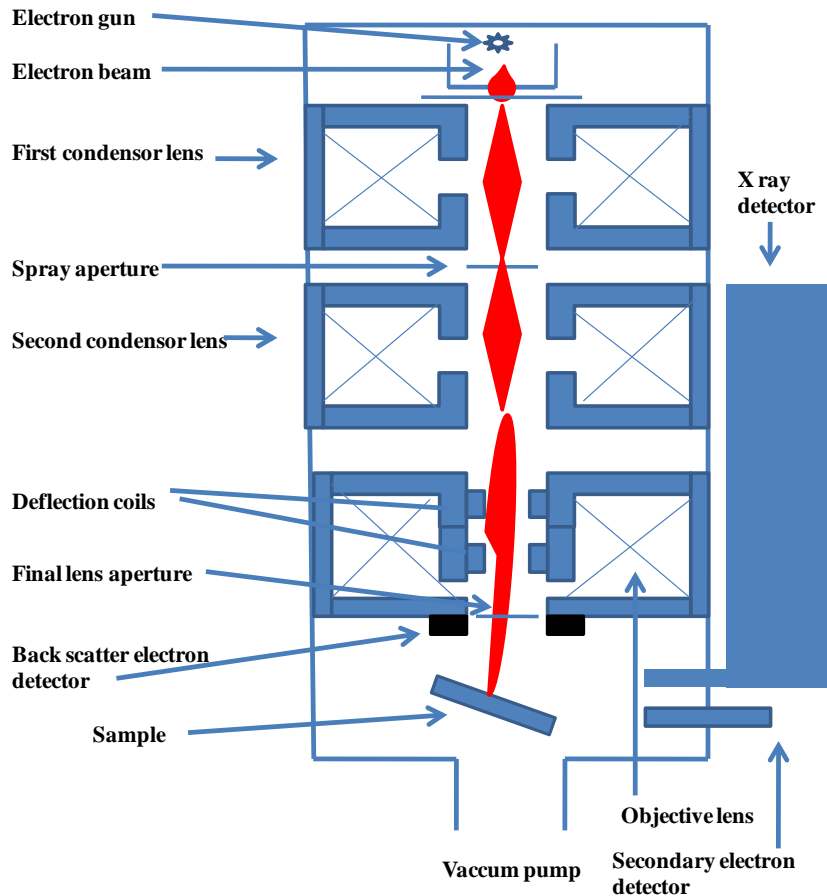


Figure 2.1. Diagrammatic representation of a Scanning Electron Microscope

2.1.2. Transmission Electron Microscopy (TEM)

TEM, as the name implies, use the transmitted electrons for the generation of images. The high-energy electrons generated by the application of high electric field is transmitted through the sample and high-resolution image is obtained. As mentioned earlier, the velocity of

the electrons, on which the resolution of the image depends, can be controlled by manipulating the applied voltage. At higher velocities, one can get a better resolution as predicted by the de Broglie equation. With the Field – emission technique, one can employ a high voltage electron beam to create an image. Here, an electromagnetic lens system is used to converge the electron beam into to a very narrow beam. Generally, TEM consists of the following components: electron source, electromagnetic lenses and an electron detector, as shown in the Figure 2.2.

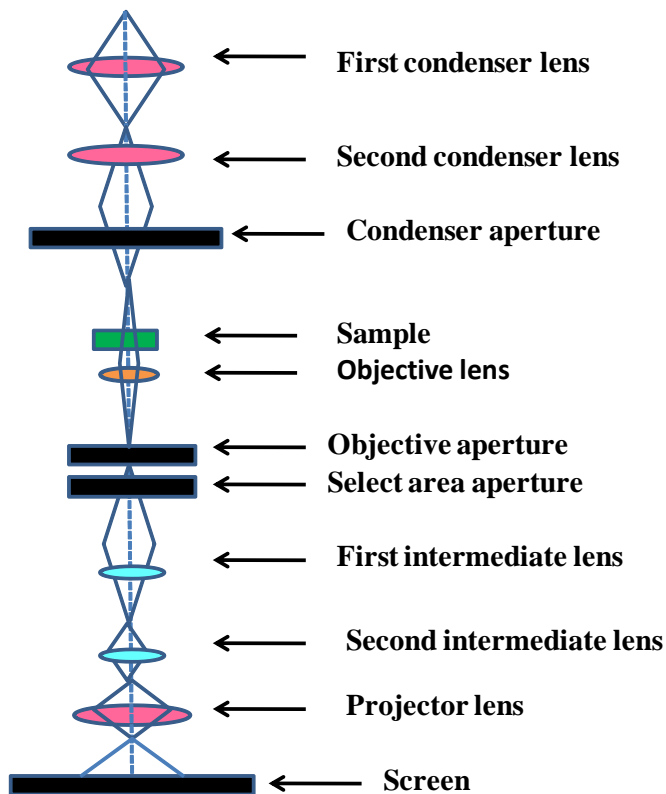


Figure 2.2. Schematic diagram of a Tunnelling Electron Microscope (TEM)

There are two (first and second, as you see in Figure 2.2) condenser lenses, objective lens, two intermediate lenses and a projector lens. Sample is placed in the path of the electron beam and the lenses focus the accelerated beam on to the sample. The beam gets transmitted through the sample after undergoing modifications in energy (depending on the extent and nature of the interaction) and the other lenses are used to magnify the image. Finally, the beam is focused by the objective lens onto a CCD camera, resulting in the formation of an image. Image quality is further enhanced by the use of additional aperture systems by eliminating the electrons diffracted at high-angles. The image passes down the column through the intermediate and projector lenses and strikes a screen. Here, all the components of TEM are kept under high vacuum. In TEM from the SAED pattern it is possible to get information about crystal structure of the material of analysis.

When the electron beam interacts with the sample, some of the electrons are transmitted through it. Some electrons undergo elastic scattering and some others undergo inelastic scattering. Both the elastically scattered electrons and transmitted electrons interact with the image screen coated with phosphorous or with CCD camera to produce a contrast image. In TEM, imaging can be done by either Bright Field TEM (BFTEM) where regions with lesser electron density will appear as bright and in Dark Field TEM it appears as darker.

2.2. Scanning Probe Microscope (SPM)

Scanning Probe Microscopy is fundamentally based on piezoelectric effect, i.e., the deformation of a material as a result of the application of an electric field. Scanning Tunnelling microscopy (STM) and Atomic Force microscopy (AFM) are both classified under the scanning probe microscopic techniques. Since AFM and STM are based on piezoelectric effect, these are also referred to as piezoelectric techniques. Magnetic Force microscopy (MFM) and Scanning Near Field Optical Microscopy (SNOM) are other techniques where MFM utilizes a sharp magnetized tip for scanning magnetic sample and SNOM shows combined applications of optical microscopy and a special resolution beyond the classical diffraction limit.

In SPM, the probe tip mounted on a cantilever tip that can precisely move back and forth on the surface of a sample whose surface is under investigation. An array of photodiodes are employed to collect the laser reflected from the cantilever. The tip moves many times over the surface and can probe the distance between the tip and the surface and can be used to plot the surface of the material using a computer software and can be used to develop images of the surfaces. One of the major advantages of this technique is that we do not require the use of a high vacuum system and the measurement is rather easy. No sample preparation and no need of vacuum makes this technique simple. Metal tips of approximately 10 nm diameter obtained by etching metals like Si, Pt-Ir or Pt-Rh or diamond film coated tips are used.

2.2.1 Atomic Force Microscopy (AFM)

AFM was originally discovered by G. Binnig and C. Gerber for solving the problems associated with STM. For STM to operate, the sample must be either a conductor or a semiconductor. Basic principle of AFM is discussed here. A schematic representation of AFM is presented in Figure 2.3. The repulsive or attractive forces operating between two atoms separated by a distance is given as

$$\mathbf{F} = \frac{\mathbf{A}}{\mathbf{R}^{12}} - \frac{\mathbf{B}}{\mathbf{R}^6} \quad (2.1)$$

Here the force is represented using F and distance between atoms by R . A and B are constants. The first and second term corresponds to repulsive and attractive terms. The force on cantilever is connected to the spring constant, K and displacement of the cantilever δz by

$$F = K \delta z$$

Resonant frequency of cantilever is related to mass and spring constant as

$$(\omega_r) = \sqrt{\frac{K}{m}} \quad (2.2)$$

Variation of force with distance is given by

$$F = F_0 + \left(\frac{\delta F}{\delta z}\right) \delta z \quad (2.3)$$

$$\text{and } F_0 = \left(K - \frac{\delta F}{\delta z}\right) \delta z \quad (2.4)$$

Resonant frequency with respect to above gradient is

$$\omega_r = \sqrt{\frac{\left(K - \frac{\delta F}{\delta z}\right)}{m}} \quad (2.5)$$

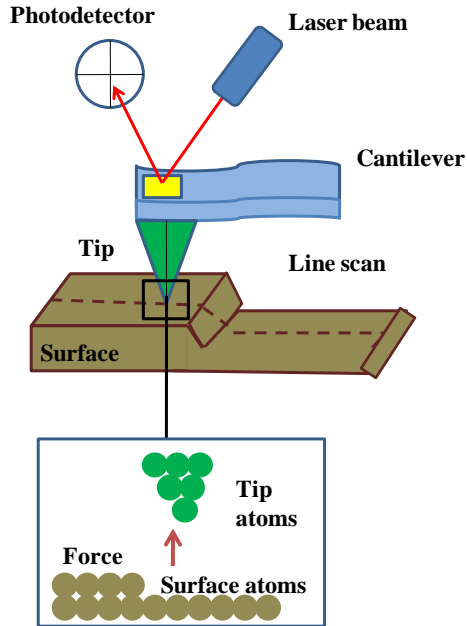


Figure 2.3. Schematic diagram of an Atomic Force Microscope (AFM)

There are primarily 3 different modes viz (1) contact mode, where tip in contact with surface (2) non-contact mode, where tip and sample do not touch (3) tapping mode, that operate both in contact and non-contact mode.

In the contact mode, the cantilever scans across a sample surface and the tip is in contact with the surface. Strong repulsive force causes the cantilever to deflect as it passes over topographically different regions.

As the name implies, in the non-contact mode, the tip is not in contact with the surface. It oscillates around 1 to 10 nm above the surface. The amplitude of oscillation will be typically in the range 1nm or less. As the cantilever passes all the surface features the distance between the surface and the tip changes, causing a change in the inter atomic forces between them. The resulting modifications in the oscillating amplitude are recorded.

Tapping mode may be considered as a combination of the contact and non-contact modes. Here the cantilever oscillates with an oscillating amplitude of 20-100nm and it oscillates at its resonant frequency.

2.3. X-ray diffraction (XRD)

The degree of crystallinity of a sample as well as the crystal structure of a crystalline solid can be determined using the XRD. In a crystalline material, the atoms or molecules are arranged in a regular manner along different planes. When X-rays falls on these planes, X-rays are scattered by this ordered array of atoms and the scattered waves undergo constructive interference and will result in a diffractogram. The interplanar spacing between the planes depend on the wavelength of the incident X-rays and incident angle by Bragg's law and it is given below

$$\mathbf{n\lambda = 2d \text{ Sin}\theta}, \quad (2.6)$$

in which **n** is an integer that accounts for the number of planes, **λ** is the wavelength of the incident X-ray, **d** is the inter planar spacing, and **θ** angle of incidence for the X-ray with reference to the plane. **θ** is called the Bragg's angle.

The diffraction pattern arising from the process will provide us the interplanar spacing between the different planes in which the atoms or molecules are arranged. X-ray crystallography has been much advanced in the recent years and one can develop the atomic level images of the arrangement in the lattice. XRD is a non-destructive technique that helps in the evaluation of the elemental composition, structural changes, degree of crystallinity, etc.

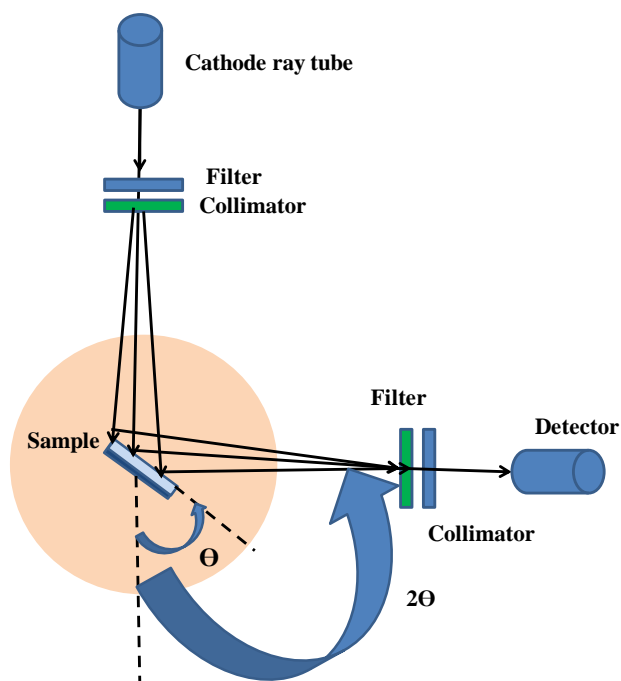


Figure 2.4. Schematic diagram of X-ray diffractometer

The major components of an XRD instrument are: (1) X-ray source (2) specimen (3) X-ray detector. These components are arranged in the circumference of the focussing circle. Here θ , (Bragg angle) is angle between the plane of specimen and source. 2θ is the angle between the projection of source and detector. The radius of the diffractometer is

fixed. The diffractometer circle is referred to as a goniometer circle. In an X-ray diffractometer sample is rotating at an angle θ and detector is mounted on an arm to collect this diffracted X-rays and rotates at an angle 2θ . The component used to adjust angle and rotate sample is known as goniometer.

X-ray sources- X-rays are produced in an evacuated tube similar to a cathode ray tube. An applied current heat up a tungsten filament which liberates electrons. The liberated electrons are accelerated by a high voltage and hit a copper target where copper X-rays are generated. Other metal targets like Mo, Cr also used. These high energy radiations can knock out electrons from K shell and it results in the emission of X-rays when returning to ground state.

In the present case, the X-ray diffraction of the samples were obtained using a Rigaku Miniflex 600 diffractometer using a Cu $K\alpha$ source in a scan range between 5° and 50° .

The specimen- The material to be analysed is placed in the sample component and it can be either a simple needle for holding crystal or a glass plate that is non-diffracting and amorphous.

2.4. Spectroscopic techniques

Spectroscopic methods generally deal with interaction of electromagnetic radiation with matter and the consequent effects on the radiation as well as the sample under study. In the case of metal and alloy nanoparticles, measurement of the surface plasmon absorptions, the collective oscillations of the surface electrons, in liquid dispersions as well as the thin films prepared constitute a major part of the study.

These range from the visible region of the electromagnetic spectrum and often extend to the NIR region depending on the nanostructures.

2.4.1. UV-Vis-NIR absorption spectroscopy

The well-known Beer-Lambert law forms the basis of the UV-Vis absorption spectroscopy. When a monochromatic light passes through a solution containing sample under study, it absorbs the radiation corresponding to the energy required for a resonant electronic process. This is marked by a reduction in intensity of transmitted light, proportional to both the concentration of the absorbing system in the solution and the intensity of incident radiation. The Beer-Lambert law is mathematically represented as

$$\log_{10} \frac{I_0}{I} = \epsilon lc \quad (2.7)$$

In this equation, I_0 represent the intensity of the incident radiation, I correspond to intensity of the transmitted radiation, ϵ is the molar absorption coefficient, l is the path length and c , the concentration of the species

Usually, spherical NP shows single absorption peaks whereas anisotropic structures show multiple peaks based on the direction of polarization and depolarization.

2.4.2. Instrumentation

Components of UV-VIS-NIR spectrometer consist of (1) source (2) filters and monochromators (3) sample compartment (4) detector (5) recorder.

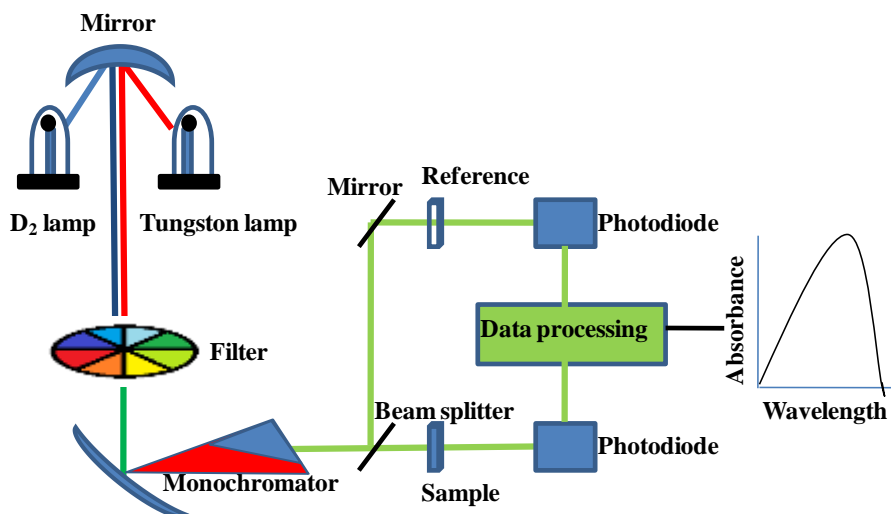


Figure 2.5. Schematic diagram of a UV-VIS-NIR spectrometer

2.5. Raman spectroscopy

Raman spectroscopy is a non-destructive vibrational spectroscopic technique, often complimentary to the IR spectroscopic technique. Unlike the latter, Raman spectroscopy is not an absorption spectroscopy, but rather is based on the inelastic scattering of molecules upon interaction with light. Energy is exchanged between the molecule and the radiation and thus results in a process where the energy of the scattered radiation is different from the incident radiation. When the molecule has taken up energy from the radiation, the scattered radiation will have a lesser energy as compared to the incident radiation and this corresponds to the vibrational/ rotational transitions within the molecule. In this study, we have employed two Raman spectrometers – JASCO MicroRaman spectrometer and Bruker FRA 106 FT Raman spectrometer. The former one uses the 532 nm excitation from the

frequency doubled Nd:YAG laser and the latter uses the 1064 nm laser from the Nd:YAG laser. In both the cases, the retro-Raman mode is used with 180° scattering mode. FT-Raman has its heart the Michelson interferometer and the diagrammatic representation of the same is given in Figure

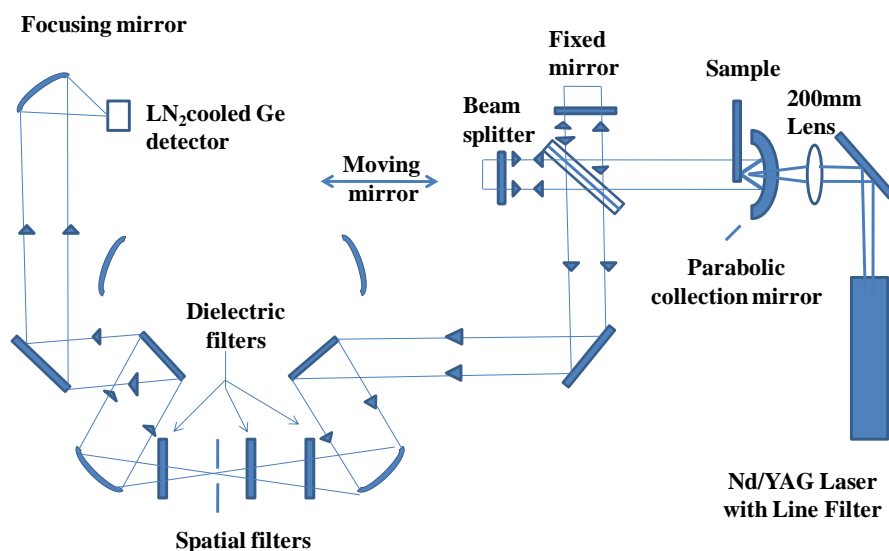


Figure 2.6. Schematic diagram of a FT-Raman spectrometer

FT-Raman spectroscopy belongs to the time-domain method and here it is possible to measure the intensity of light of many frequencies simultaneously. In this technique a Fourier transform algorithm is applied to an optical spectrum and it also known as time domain spectroscopy since a time delay is varied. The optical filters help in eliminating undesired light to reach spectrometer and saturating detector since Raman signals are very weak and there is possibility for Raman signals drowning out. For getting efficient and intense Raman bands the

reduction of the Rayleigh line should be comparable with the strongest Raman line and holographic notch filters aids in eliminating light at the laser frequency from the scattered signal. In the FT-Raman, the laser radiation is focused to the sample by means of a lens and a parabolic mirror, and the light scattered from the sample is collected and a beam splitter is used for passing light through it and then it passes to the moving and fixed mirrors in the interferometer head. From there it passed through a series of dielectric filters and focused onto a liquid N₂ cooled Ge detector.

A schematic diagram of the optics of the JASCO Micro Raman spectrometer is presented in Figure 2.6.

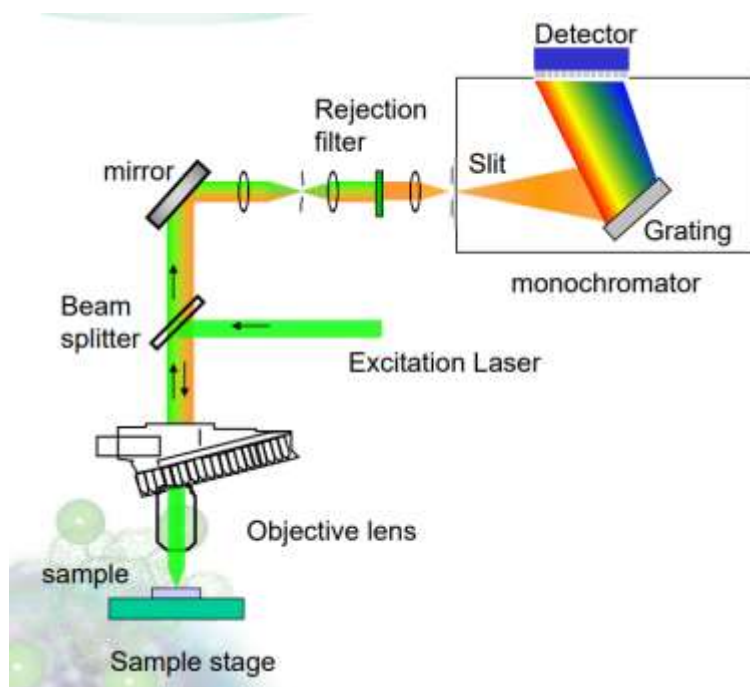


Figure 2.7. Schematic diagram of the JASCO Micro Raman spectrometer

In this equipment, a grating is used to the laser light and is directed through a band pass filter with appropriate wavelength. The backscattered light is collected through the objective and after filtering with a Notch filter to reject the elastically scattered signal, the light is transmitted through the confocal pinhole into the spectrometer. The signal is then directed onto a grating which disperses the light and eventually guided onto the detector to collect the Raman spectrum.

2.6. SERS Spectral Studies

Metal and alloy nanoparticles were prepared by reduction of the corresponding metal ions using a simple reducing agent such as β -D-glucose. Different SERS substrates were prepared by depositing these nanoparticles on solid substrates such as Whatman filter paper or cloth as was done in specific questions. Materials were characterized at different stages using the various techniques mentioned above. Since there are minor variations in the preparations, individual preparation methods are detailed in the Chapters 3, 4, 5 and 6 respectively. Sample sizes of ~ 1 cm square pieces were employed for the SERS measurements.

2.7. Quantum chemical calculations

Theoretical Raman spectra of the compounds are calculated using the Gaussian programme using the B3LYP functional and 631+G* basis set after optimizing the structure of the molecule at the same level. Gaussview was used for the preparation of the input files as well as viewing the output.

CHAPTER 3

PLASMON- RESONANT, NEAR- RESONANT AND OFF-RESONANT SERS OF MODEL DITHIOL SYSTEMS

3.1 Introduction

Enabling the promise of molecular level detection has pushed SERS an ultrasensitive vibrational spectroscopic tool which can serve as a tool for the detection of analytes at very low concentrations.¹⁶²⁻¹⁶⁴ As discussed in Chapter 1, Surface Plasmon Resonance (SPR) is expected to make significant contribution to the enhancement of the intensity of Raman signals. It may be noted that, in fact, LSPR is the basis to generate sub-wavelength enhanced electromagnetic fields for a number of phenomena such as molecular fluorescence, vibrational spectroscopy, photovoltaics, energy transfer, molecular sensing etc.¹⁶⁵⁻¹⁶⁷ As discussed earlier, these Plasmons can be propagating or localized and in propagating case, plasmons cannot couple with light, but the closed geometrical boundaries of metallic nanoparticles can sustain a localized oscillation of the surface charge density. The concept of enhanced spectroscopy relies on the enhancement of local electrical fields adjacent to rough metallic surfaces with intense local fields at gaps and atomically rough protrusions. These spots, with regions of concentrated electromagnetic fields, are often termed as hotspots and can act as optical antennas that support LSPR.¹⁶⁸ It will be highly beneficial, if it is possible to control the magnitude of this enhancement by tailoring geometrical surface parameters at nanometric levels. There are plenty of studies dealing with

the control of LSPR over SERS enhancement mechanism.¹⁶⁹⁻¹⁷² It was demonstrated that it is very easy to tune λ_{\max} (the absorption maxima for the LSPR absorptions), by simple alloying techniques. For example, by alloying between Au and Ag, one can prepare AuAg alloy nanoparticles having λ_{\max} values lying between those of pure Au and Ag nanoparticles.¹⁷³⁻¹⁷⁶ From this point, it is pertinent to examine how the SERS spectra will depend on the wavelength of the laser excitation (λ_{exc}) and λ_{\max} .

Historically, although the two mechanisms, viz., electromagnetic and chemical enhancements, are hypothesized to explain SERS, it is rather difficult to separate out these two effects completely since chemical effect operates almost simultaneously with the LSPR effect. Zhang et al carried out the SERS studies of Crystal Violet (CV) on single, dimer, trimer and aggregates of Silver microparticle surface modified with nanostructures (MSMN) and chemical effect is determined by the chemical adsorption behaviour of CV on single particle.¹⁷⁷ As the number of particles is increased as dimer, trimer, aggregates, no new SERS signals related to chemical effect can be observed and further enhancement is attributed to the LSPR effect. Since the SERS enhancement factor is calculated purely based on electromagnetic enhancement i.e., LSPR effect, it is important to distinguish LSPR from chemical effect. Saikin et al also carried out SERS spectral studies of Benzene thiol molecule with the view of separately identify chemical and electromagnetic contributions and arrived at an important conclusion that the effect of chemical binding is mostly due to changes in the electronic structure of the molecule rather than to the fixed orientation of molecule relative to the surface.¹⁷⁸

There are several important factors that affects SERS.¹⁷⁹ Firstly, the proximity of the molecule with the SERS active substrate determines the local electric field experienced by the molecule. In general, the molecules lying closer to the surface will experience greater SERS enhancements as compared to those lying farther. Secondly, the location of analyte molecule on SERS substrate is important. Large enhancement in SERS signal is observed if molecule is present in the gaps between nanoparticles or on sharp edges or corners of nanoparticle where the concentration of the electric field is greater (hot spots). Since the electric field is a directional property, orientation of the molecule with respect to the surface normal of the substrate will also be a key factor in deciding the SERS enhancement. The strongest enhancement will occur if the induced polarizability or dipole moment of a molecule is parallel to the electric field vector of the light field.¹⁸⁰ Lastly, the interaction between molecule and the substrate act as another determining parameter in SERS that is usually explained by charge transfer interaction and contributes to ‘chemical enhancement’. In fact, one needs to consider all these factors to satisfactorily explain the SERS enhancements.

Since uncertainties about the importance of chemical effect in SERS are still unresolved, studies related to chemical enhancement is very important. Fromm et al described the first use of single resonant “bowtie” nanoantennas consisting of two metallic triangles oriented tip to tip with a coupled plasmon and known electromagnetic enhancement measuring SERS from chemically bonded p-Mercaptoaniline molecule and explored the role of chemical enhancement in SERS.¹⁸¹ Chemical enhancement for organic adsorbates on metal surfaces is reviewed by

Zayak et al using DFT calculations of the static Raman tensor demonstrating a strong mode-dependent modification for the Raman spectra of a Benzene Thiol by Au substrates.¹⁸¹ Raman active modes with the largest enhancement result from stronger contributions from the metal to their electron-vibron coupling, as quantified through a deformation potential. Valley et al carried out normal and SERS studies of a set of substituted benzene thiols both experimentally and theoretically calculated polarizability tensor by TDDFT and found that enhancement varies by a factor of 10, as a result of chemical substitution, with stronger electron donating groups on the benzene unit leading to higher enhancement.¹⁸³

For understanding the mechanism of SERS, the dependence on excitation wavelength for a given nanostructure morphology is important. Sunwani et al has carried out a study related to effect of excitation wavelength and metallic nanostructure on SERS spectra of C₆₀ deposited on structurally different Au surfaces. Two excitation lines 532 nm and 784 nm are used and SERS from different surface morphologies were found to be similar with 532 nm excitation but different with 784 nm excitation which suggested that each excitation wavelength activates different Raman enhancement mechanism in the C₆₀ layer.¹⁸⁴ In another study Puebla et al summarises experimental complexities associated with SERS studies and explain in detail many factors related to instrumentation, the optical enhancer and the analyte molecules.¹⁸⁵ In this article, he shared an interesting view about SERS spectral intensity associated with detector artefact. According to him, for different excitation lines, the quantum efficiency of the detector varies

and this will perturb the true spectrum. Selection of the best excitation line for a given LSPR position is highly important in SERS. There have always been contradictory observations about this. Initially, an excitation line that was slightly red-shifted from the λ_{\max} of the Plasmon extinction spectrum was believed to give maximum enhancement in SERS. But later Van Duyne et al prepared silver thin films having absorption from blue to NIR and SERS spectra of Benzene Thiol was obtained using 13 different laser excitations.¹⁸⁶ In all cases, the best excitation line was blue-shifted with respect to λ_{\max} of the SERS substrate nanoparticle systems.

Influences of SPR wavelength on SERS activity was also studied by Kwon et al and estimated that nanoparticle ensemble exhibiting a Plasmon resonance wavelength at 491 nm, which almost coincides with the excitation wavelength gives highest SERS activity.¹⁸⁷ Wavelength dependency of SERS was again observed in the SERS studies of 4-ATP and 4-MOTP using 532 nm, 633 nm, 785 nm and found that EM effect operate for 4-MOTP and for 4-ATP at 785 nm at all wavelengths but for 4-ATP, CT effect is operating at shorter wavelength excitation of 633 nm and 532 nm.¹⁸⁸ Increase in SERS intensity when the excitation wavelength is close to the maximum of plasmonic band is given by H Guo et al.¹⁸⁹ A similar observation regarding maximum SERS enhancement for a plasmon peak blue shifted from laser excitation is given by Sivapalan et al.¹⁸⁹ But McFarland in wavelength –scanned surface enhanced Raman excitation spectroscopy reported a completely different selection of Plasmon band - red shifted from excitation wavelength for maximum SERS enhancement.¹⁹⁰

The most used substrates for SERS were electrochemically roughened metal electrodes.¹⁹¹ Metal nanoparticles in suspension faces weak enhancement and stability of the colloid after addition of analyte.¹⁹¹ Other methods are metal nanoparticles immobilized in planar solid supports and fabrication of metallic nanostructures using nanolithography. One of the most promising approaches towards reproducible nano structures is template technique.¹⁹²⁻¹⁹⁵ But a simple, low cost, highly reliable and reproducible SERS substrate is needed to explore the potential of SERS in electrochemistry, biosensing, environmental analysis etc. So, on this ground we investigate the use of metal nanoparticle and alloy nanoparticle decorated on cellulose acetate sheet as a SERS substrate which can be fabricated in a simple strategy.

Flexible polymer-based SERS substrates are highly desirable for in-situ Raman detection of chemicals and biological targets which cannot be achieved with rigid substrates such as silicon, glass etc.¹⁹⁶ In-situ formations of metal and alloy nanoparticles inside polymer films in which polymer is acting as both reducing and stabilizing agent is a facile route to the fabrication of efficient SERS substrate. But this method lacks the control over nanoparticle morphology due to interplasmonic coupling. We couldn't fabricate SERS substrates with nanoparticles of desirable shape. Our method is based on synthesis of nanoparticles with required size and shape and these will not undergo any morphological changes during transfer to cellulose acetate sheets, humid.

In this chapter, we investigate the dependence of SERS both on λ_{\max} and the choice of the excitation line, λ_{exc} . Here, the tuning of λ_{\max} has been

achieved by taking appropriate combinations of the Au:Ag alloy nanoparticles as well as by networking them. Two excitation sources, 1064 nm line of the Nd:YAG Laser of the Bruker FT Raman spectrometer as well as its frequency doubled 532 nm line in the JASCO Micro Raman spectrometer, respectively, are used. Detailed, comparative SERS studies of 1,4-BDT, adsorbed on Au, Ag and Au Ag alloy SERS substrates using these two laser lines are presented. Typically, three cases are presented in Figure 3.1.

Case I is a condition where λ_{\max} and λ_{exc} match well or are very close to each other. This is described as Plasmon-resonant SERS. This is the case achieved when the 532 nm laser is employed with the Au NP substrate with a typical λ_{\max} of 530 nm as attained in the preparatory conditions mentioned here.

Case II is the Plasmon-near resonant case where the λ_{\max} is very close to the excitation line, as in the case of the Au:Ag alloys; achieved by tuning the λ_{\max} by alloying with appropriate compositions. Typically, λ_{\max} is moved systematically away from the λ_{exc} .

Case III is the Plasmon off-resonant case, where the excitation line is far away from the λ_{\max} of the substrates. This is true for the silver nanoparticles where the λ_{\max} is around 420 nm (for Ag NPs) and in cases where the λ_{exc} is the 1064 nm of the Nd:YAG laser.

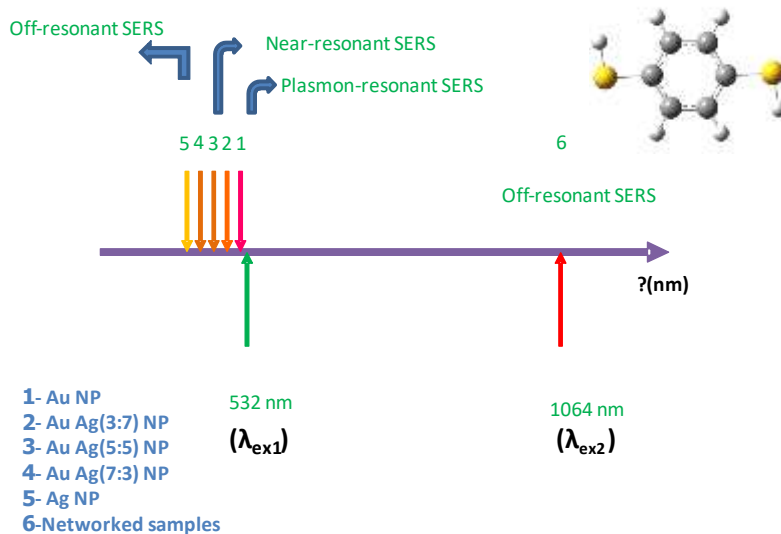


Figure 3.1. Schematic diagram showing Plasmon resonant, near -resonant and off-resonant cases (Case I, Case II, and Case III, respectively).

Significant differences are observed in the spectra recorded under the three different conditions. The results are explained based on both electromagnetic and chemical enhancement mechanisms. We also carried out SERS studies of different dithiols (1,2-BDT, 1,3-BDT, 1,4-BDT) on under these three conditions. Structures of the dithiols used in our SERS studies are shown in Figure 3.2.

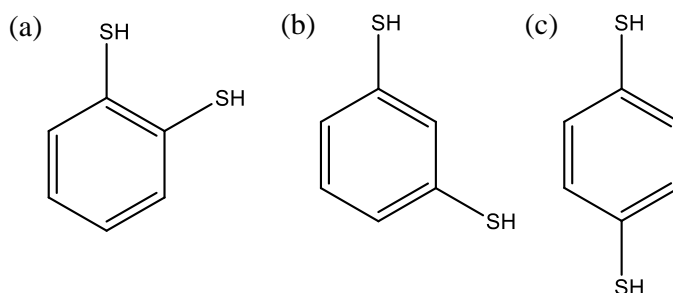


Figure 3.2. Molecular structures of the different dithiols used: (a) 1,2-BDT, (b) 1,3-BDT, (c) 1,4-BDT.

3.2. Experimental Methods

3.2.1. Materials

For the synthesis of metal and alloy NPs, high purity chemicals were used. $\text{HAuCl}_4 \cdot 3\text{H}_2\text{O}$ (99.9+%, Sigma Aldrich), D (+) Glucose (ACS reagent, Sigma), Soluble Starch (extrapure, Merck), NaOH (extrapure, AR, SRL) were used as purchased. Doubly distilled water was used for all the experiments. Cellulose Acetate sheets, humid (unperforated) and 1,4 –Benzene Dithiol were purchased from Sigma Aldrich. The UV-Vis spectra used for the characterization of NPs were carried out using Jasco V-550 model spectrophotometer. SEM of the metal nanoparticle decorated CA sheets was taken using NOVA NANOSEM 600, FEI Company, The Netherlands. For FT-Raman spectral measurement Bruker FT-RAMAN spectrometer with laser wavelength 1064 nm is used. The 532 nm laser experiments were carried out using the JASCO Micro Raman spectrometer.

3.2.2. Synthesis of Au, Ag and Au-Ag alloy nanoparticles

Au and Ag NPs were synthesized by reducing the respective metal ions using D (+) Glucose. Soluble starch was engaged as the capping reagent.

The precursors of metal NPs, glucose and starch containing solutions were heated in a microwave oven. 0.1 M NaOH solution was added dropwise to make the pH basic, to accelerate nanoparticle formation. For this 40 ml .05 M Glucose solution, 25 ml (1%) starch and 250 μ l H₂SO₄ were used.

3.2.3. Preparation of NPs decorated Cellulose Acetate sheets

After preparing NPs, solutions were characterised using UV-VISIBLE spectrophotometer. The CA sheets were immersed in colloidal NP solution and thermally evaporated in an oven at a temperature of 60⁰C. Overnight drying results in uniform distribution of metal NPs both inside and outside of the CA sheets. This can be visually observed by the colour of the CA sheets. Schematic diagram for SERS substrate preparation is shown below.

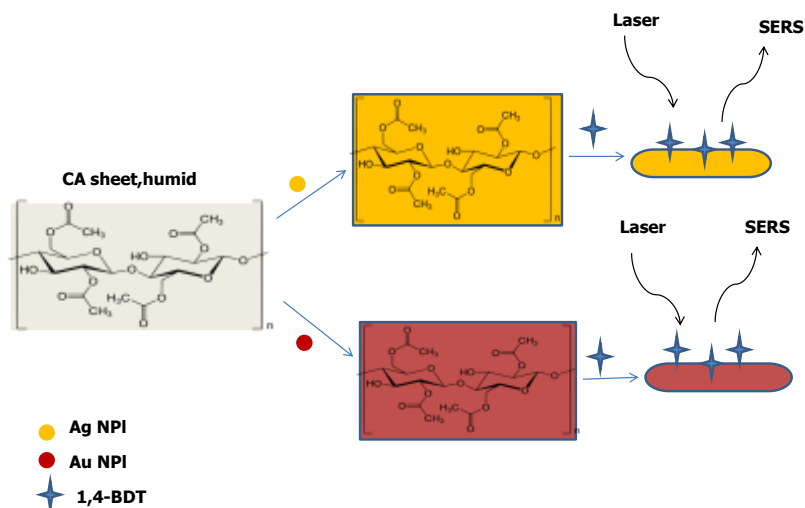


Figure 3.3. Schematic diagram showing the preparation of SERS substrate.

3.2.4. Preparation of networked Au, Ag and Au Ag alloy NP Films

Networked substrates of Au, Ag, and AuAg alloy NPS were prepared at higher pH following the method of Raveendran et al ¹⁹⁷ wherein the binding between the nanoparticles and the protecting group is rather weak, leading to the metal to metal bond formation between the individual NPs, resulting in a kinetically driven network formation. In a typical preparation, 0.1 M NaOH was added to 40 ml 0.05 M Glucose solution, so that the pH reaches a value greater than 12. To this solution, 600 μ l 0.1M HAuCl₄ was added dropwise, resulting in the formation of a black coloured Au NP network. For preparing networked Ag and Au-Ag alloys of different composition, glucose solution of desired pH was added to corresponding precursors.

3.3. RESULTS AND DISCUSSIONS

3.3.1. UV-VISIBLE, FESEM and AFM studies

Photographic images of colloidal Ag NP, Au NP, and alloy nanoparticles of different composition are shown in Figure 3.4. (a). Normalized absorption spectra of Au-Ag alloy nanoparticles of varying compositions are shown in Figure 3.4. (b). A plot of percentage of Au against λ_{\max} for different alloy compositions is shown in the Figure 3.4 (c). Alloy formation of Au-Ag NP and the dependence of the plasmon absorption on their composition can be confirmed from UV-Visible absorption spectra. For alloy NP formation, simple co-reduction of HAuCl₄ and AgNO₃ using glucose as the reducing agent and starch as the capping agent were employed. A linear relationship between the

value of λ_{\max} and the % composition is observed, indicating that the alloy NPs are homogeneous.

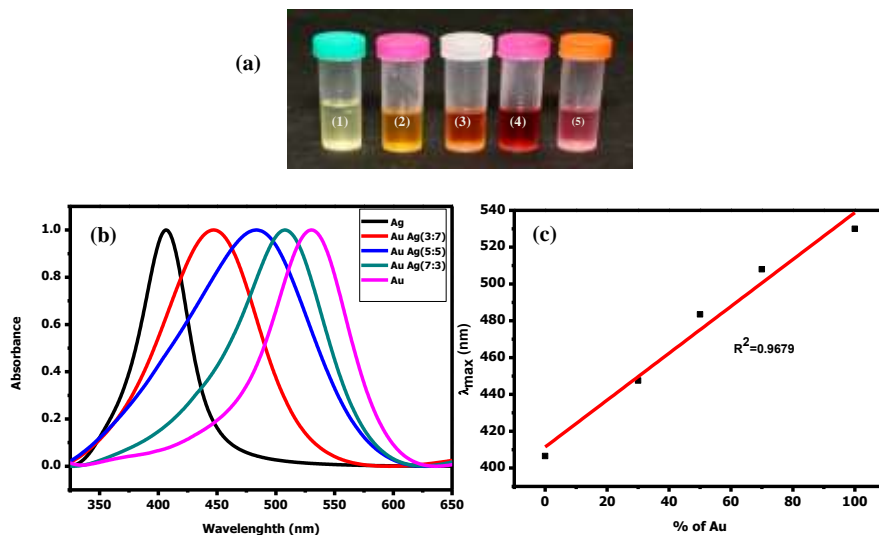


Figure 3.4. (a) Photographic images of aqueous dispersions of (1) Ag NP; Au:Ag alloys of the compositions (2) 3:7 Alloy, (3) 5:5 Alloy, (4) 7:3 Alloy and (5) Au NP; (b) UV-Vis absorption spectra corresponding to images (1)-(5); (c) Plot of λ_{\max} vs % of Au in the nanoparticle for (1)-(5).

The CA sheet used as the solid support for NP adsorption is also a biodegradable, biocompatible material. Synthesis of NPs and NP-decorated CA SERS substrate formation requires only mild reaction conditions and simple experimental, making it an attractive method for the preparation of SERS substrates for routine SERS measurements.

Photographic images of metal- and alloy- NP embedded CA sheets and their corresponding Diffuse Reflectance UV-VIS spectra are presented in figure 3.5.(A) and (B).

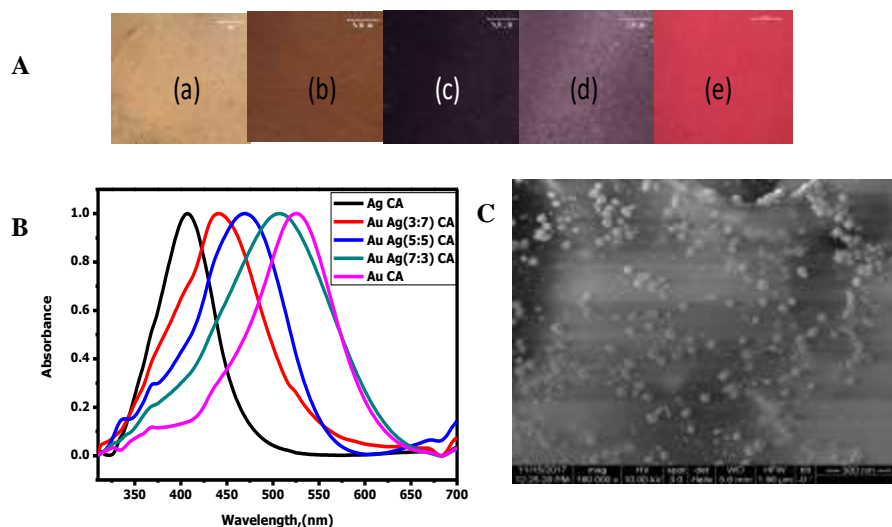


Figure 3.5. (A) Photographic images of CA sheets deposited with various metal and alloy NP: (a) Ag, (b) Au Ag (3:7), (c) Au Ag (5:5), (d) Au Ag (7:3), (e) Au; (B) diffuse reflectance UV-Vis absorption spectra of the substrates (a) – (e); (C) FE-SEM of Au NP -embedded CA sheet.

The NP decorated CA sheets were further characterized by Diffuse Reflectance Spectroscopy and this confirms the absorption of NP on CA sheets. Although the DRS spectral bands are relatively broader in comparison with those of the sols, one doesn't observe any significant shifting of the peaks. This is further confirmed by the SEM images as shown in Figure 3(C). The elemental composition of fabricated material is confirmed by Energy Dispersive Analysis of X-rays (EDAX). In figure 3.6 (A) and (B), the FESEM images of Au CA and CA sheets are shown. The porous nature of the substrate allows the easy placement of the NPs in those pores. The EDAX spectrum of CA is presented in figure 3.6 (C), which has only two peaks corresponding to carbon and oxygen. For better information about distribution of MNPs on CA sheet, SEM analysis of NP decorated CA sheets was also carried out.

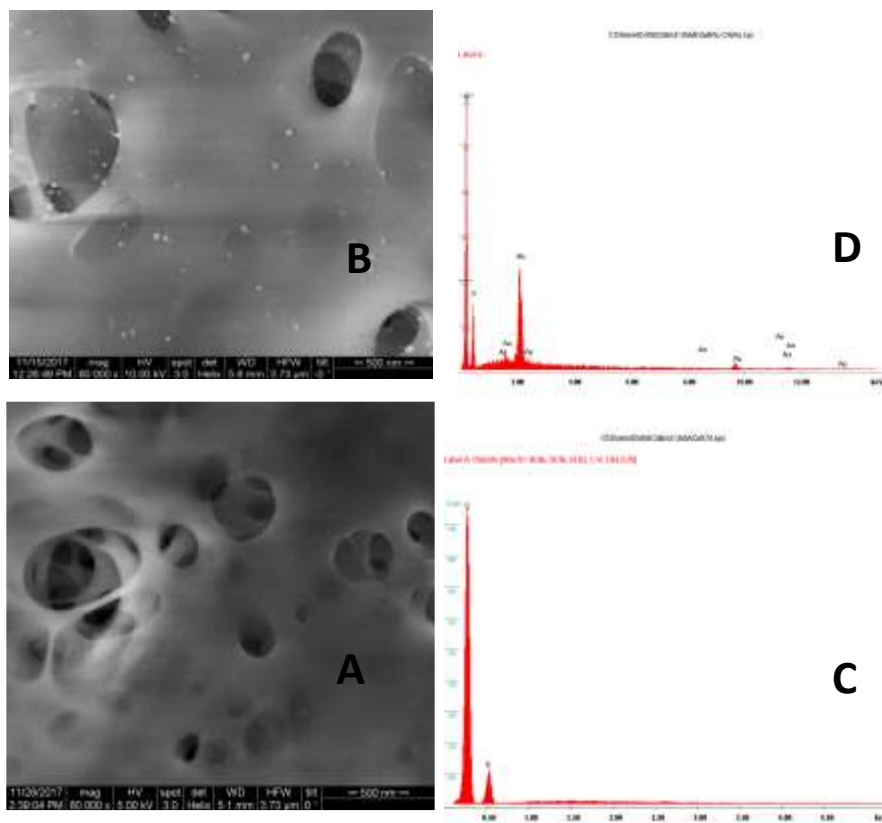


Figure 3.6. (A) FESEM image of CA sheet alone; (B) Au CA; (C) EDAX of CA sheet alone; (D) EDAX of AuCA.

Figure 3.6. (B) shows well dispersed spherical Au NPs on CA matrix without aggregation. Typically, NPs showed a size less than 20 nm. For extending our work to alloy NP based CA sheets, we prepared Au- Ag (3:7,5:5,7:3) alloy by the same synthetic route described above. Figure 3.6. (C) shows EDAX corresponds to the presence of C, O, and Au on the CA sheet.

AFM analysis of the CA sheets decorated with Au, Ag and AuAg alloy NPS are presented in Figures 3.7 – 3.9 and substantiates the presence of the nanometer-scale roughness required for obtaining the SERS spectra.

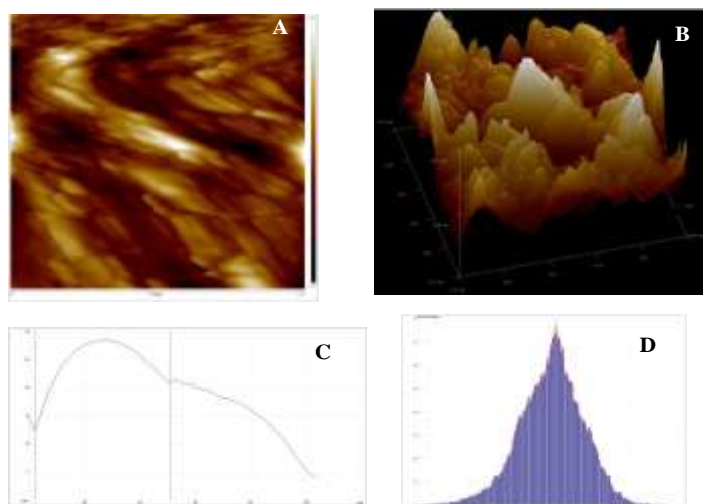


Figure 3.7 AFM analysis of Au CA; (A) 2D,(B) 3D, (C) particle size, (D) particle distribution.

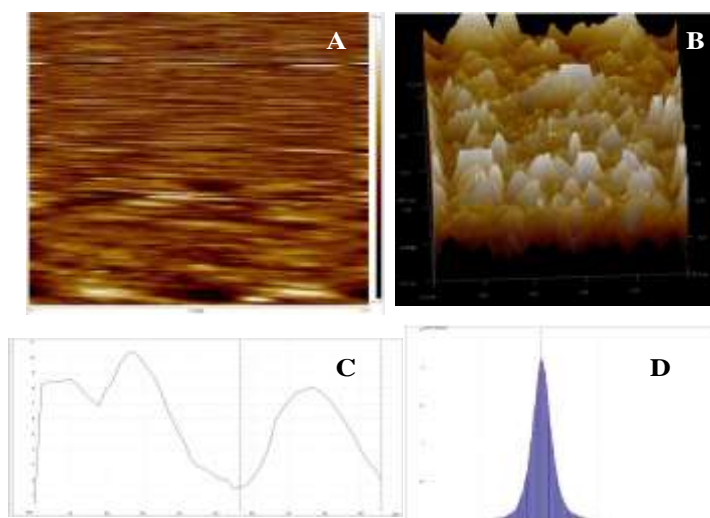


Figure 3.8. AFM analysis of Ag CA; (A) 2D, (B) 3D, (C) particle size, (D) particle distribution.

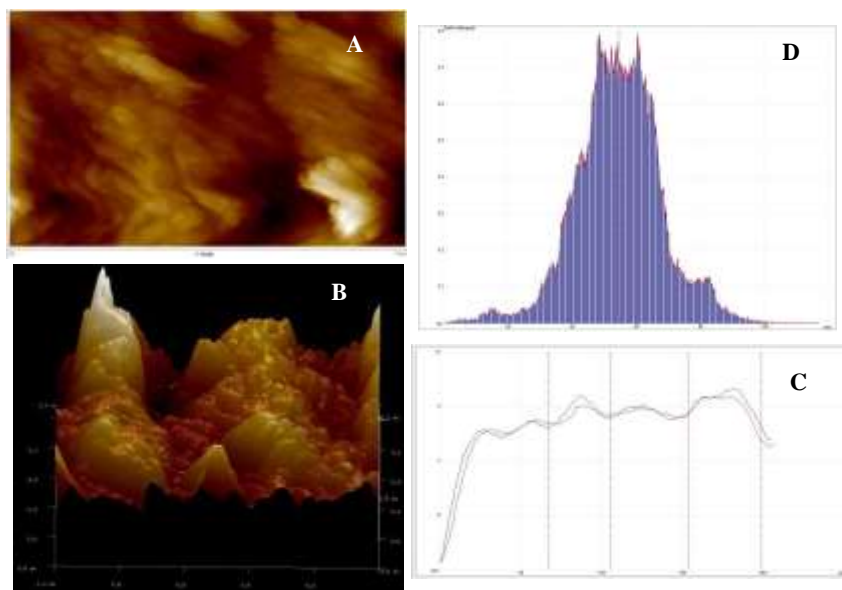


Figure 3.9. AFM analysis of Au Ag alloy (5:5) CA; (A) 2D, (B) 3D, (C) particle size, (D) particle distribution.

Networking of the metal and alloy nanoparticles will result in the delocalization of the surface plasmons of the metal and alloy nanoparticles via interplasmonic coupling causing significant changes in the optical properties of these substrates. The optical images of the networked thin films formed from Au, Ag, and AuAg alloy nanoparticles is presented in Figure 3.10 (A).

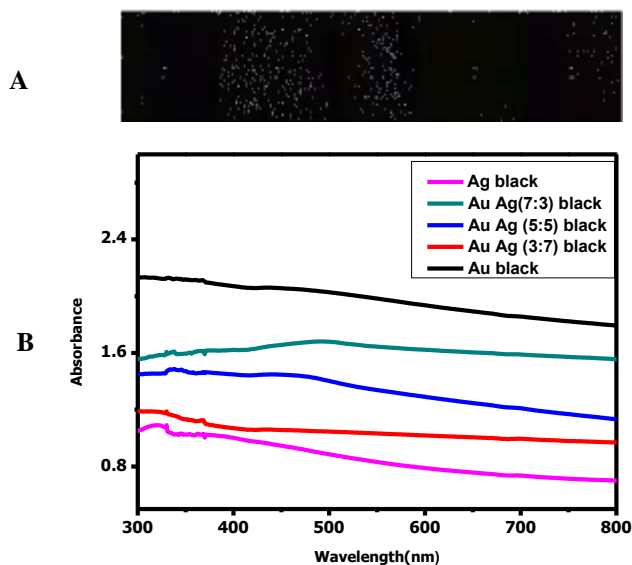


Figure 3.10. (A) Photographic images of Networked films from the nanoparticles of (a)Ag, (b) AuAg (3:7), (c) AuAg (5:5), (d) AuAg (7:3), and (e) Au; (B) Corresponding diffuse reflectance UV-VIS absorption spectra.

All networked films appeared black in colour with slight variations as shown in photographic images shown in Figure 3.10 A Corresponding UV-DRS spectra presented in Figure 3.10 (B) clearly shows a broad range of absorption covering entire visible region of the electromagnetic spectrum. The Morphology and composition of the networked films were analyzed using FESEM and EDAX and are presented in Figure 3.11. The SEM images reveal that the Au, Ag, and alloy are mesoporous, plausibly as a result of the kinetically driven networking of the individual nanoparticles, as hypothesized by Raveendran et al.¹⁹⁷

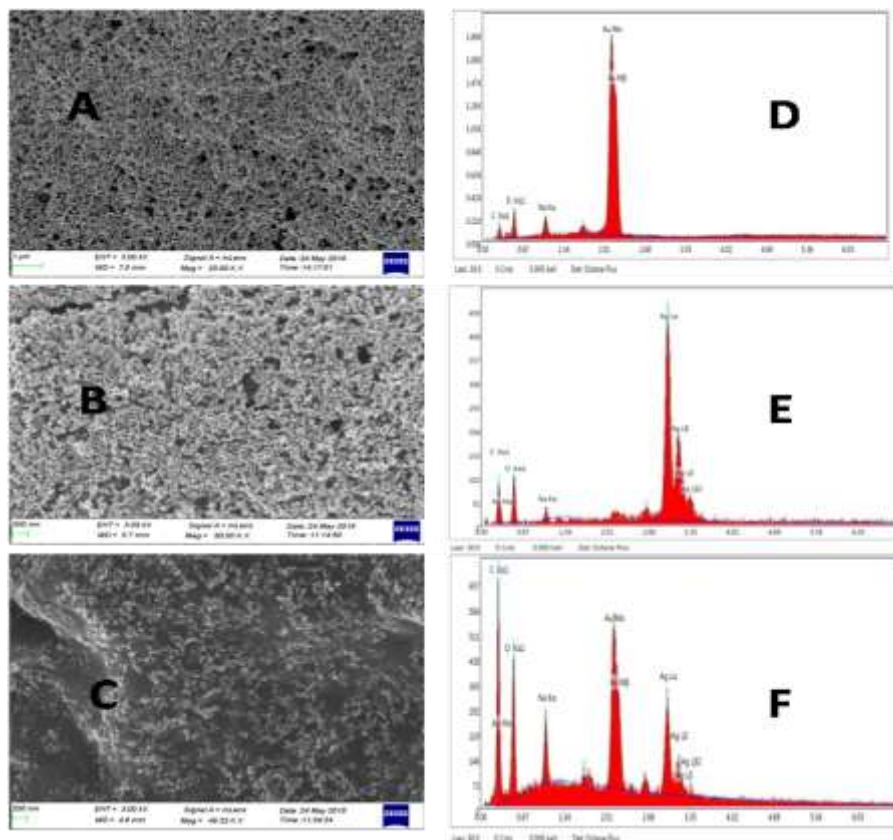


Figure 3.11. FESEM images of networked thin films from (A) Au, (B) Ag; (C) Au Ag (5:5) alloy nanoparticles; (D), (E) and (F): corresponding EDAX spectra.

3.3.2. SERS Studies

As mentioned in the introduction to this Chapter, herein we investigate how the plasmon-resonant, near-resonant and non-resonant differ. Since the 1064 nm excitation is far away from the LSPR absorption corresponding to the Au, Ag, and the AuAg NPs with different bimetallic compositions a comparison of the ordinary Raman spectra of 1,4-BDT with that of SERS spectra obtained from the various substrates

embedded with the different NP systems, recorded using the 1064 nm excitation line is presented in Figure 3.12. Spectra is divided into two regions. The spectral regions 200-2000 cm^{-1} and 2300-3100 cm^{-1} are plotted separately, for clarity purposes. Generally, the spectra are quite intense in all the cases and observes a similarity between the spectra corresponding to the various substrates, except for the slight broadening. The broadening in the alloy spectra may be attributed to the faster relaxation of the excited vibrational modes on those surfaces due to the microheterogeneity. For Au and Ag, the relative intensity is higher for peak at 352 cm^{-1} (C-S stretch and ring stretch). For alloys, the peak at 1562 cm^{-1} is relatively more intense (ring C-C-C stretching vibrations).

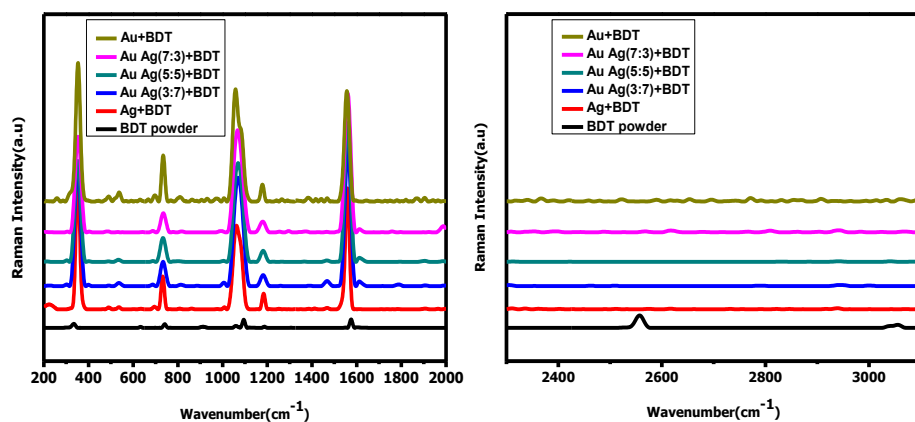


Figure 3.12. Plasmon non-resonant SERS using 1064 nm laser excitation. The black curve corresponds to the ordinary powder Raman spectrum of BDT and the rest are its SERS spectra on the Ag, Au and Au- Ag alloys as described.

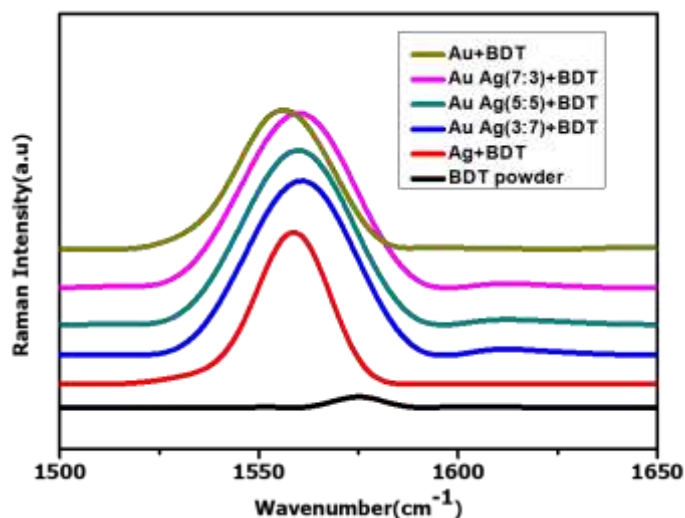


Figure 3.13. Ring C-C-C stretching vibrations of 1,4-BDT over Ag, Au and Au- Ag alloys of different composition acquired using 1064 nm FT-Raman.

The FT Raman spectral region ($1500 - 1650 \text{ cm}^{-1}$) corresponding to the aromatic ring C-C-C stretching vibrations of 1,4-BDT over Ag, Au and Au- Ag alloys of different composition acquired using 1064 nm FT-Raman are presented in Figure 3.13 for a closer look at the spectral features. There are two salient features. The first is that the band occurs at a higher wavenumber in the case of the alloys as compared to the SERS on the monometallic systems. It must be noted here that in all the cases, these SERS bands are relatively red-shifted in comparison with the powder Raman spectra. This may be attributed to an interaction with the metallic surface, whereby the electron density is lowered in the aromatic π -electron system causing a reduction in the bond order and consequently, the force constant corresponding to this mode. Going by the same reason, one must also hypothesize that the interactions are stronger in the case of the monometallic NP systems as compared to the

alloy systems, although this difference is not very significant. Secondly, the SERS spectral bands are relatively broader over the alloys in comparison with those obtained for pure Au and Ag NP substrates plausibly due to faster vibrational relaxation on the alloy NP systems as discussed earlier.

3.3.2.1. Relative Intensities

How do the relative intensities of the various peaks respond to the off-resonant SERS? We hypothesize that one will not observe much differences since the LSPR absorption maximum is far away from the λ_{exc} . The four bar diagrams corresponding to the relative intensities of specific peaks against $\Delta\lambda$ (difference between λ_{exc} and the λ_{max}) corresponding to the LSPR absorptions for Au, Ag, and alloy NPs are presented in Figure 3.14. For calculating I_1/I_2 , the peak at 1181 cm^{-1} is taken as the base peak (I_2), since it does not show much difference in intensity. Intensity ratios of the peaks at 352 cm^{-1} , 730 cm^{-1} , 1064 cm^{-1} and 1562 cm^{-1} were calculated with respect to the intensity of the peak at 1181 cm^{-1} . Except for bar diagram 2 corresponding to intensity due to ring stretching vibration at 730 cm^{-1} , all relative intensity ratios were found to be higher for alloys.

It may be noted that the wavelength - scanned Surface Enhanced Raman Excitation Spectroscopic studies reported by van Duyne et al, showed a higher signal enhancement when the λ_{max} was red-shifted with reference to the laser excitation wavelength.¹⁸⁶ However, in the present studies, no such clear dependence is observed with reference to λ_{max} . The

observed pattern may be due to the differences in the local dielectric environment in the case of the alloys.

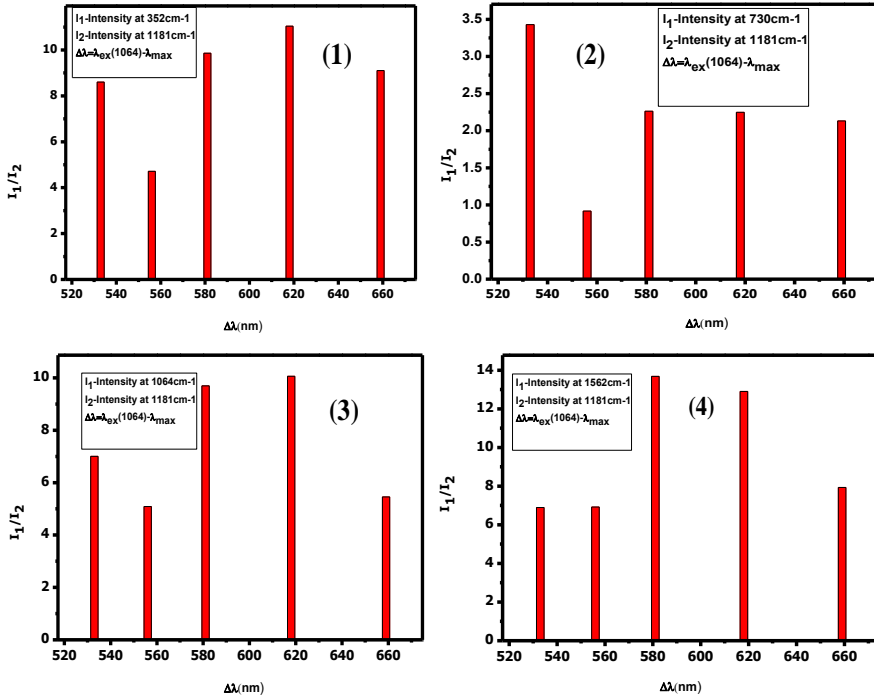


Figure 3.14. Bar diagrams corresponding to the relative intensities of specific peaks against $\Delta\lambda$ (difference between λ_{exc} and the λ_{max} corresponding to the LSPR absorptions for Au, Ag, and alloy NPs.

3.3.2.2. FT-SERS on networked NP substrates using 1064 nm laser excitation

As we had discussed earlier, upon networking, most of the LSPR vanished due to plasmon delocalization. On the other hand, there is tremendous possibility for the formation of interconnected nanometallic structures where one expects the formation of hotspots with significantly higher local electric fields. Thus, the networked Ag, Au, and AuAg

alloys of different compositions might result in a spectral behavior that is different from that for the non-networked substrate. One significant observation is the decrease in intensity of the peak at 352 cm^{-1} (which may be attributed to a combined motion involving both the C-S and the ring). Puebla *et.al* has discussed in detail about the effects of the incident light on the absolute and relative intensity, as well as the SERS spectral profiles.¹⁸⁵ In his paper, he illustrated that for the same sample excited with two different wavelengths, the shorter one will overestimate the intensity of the bands at high wavenumbers, while the longer one will do the same with the shorter wave numbers. He explained this as an instrumental artifact. However, in the present studies, since we are using the same excitation source and the same measurement parameters, our observations will not suffer from such artifacts.

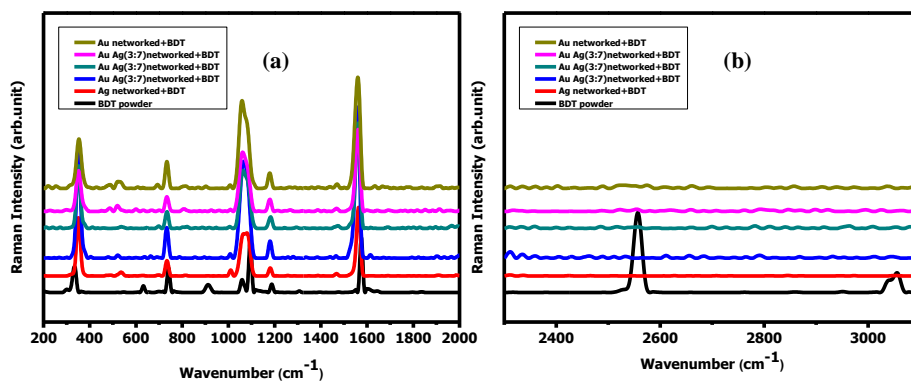


Figure 3.15. SERS spectra of BDT using 1064 nm laser excitation over networked nanostructures in different spectral regions: (a) $200\text{-}2000\text{ cm}^{-1}$ and (b) $2300\text{-}3100\text{ cm}^{-1}$.

Most fascinatingly, the relative intensities of the spectral bands in the SERS spectra obtained on the non-networked (Figure 3.12) and on the networked (Figure 3.15) SERS substrates shows some differences.

Particularly, there is a reversal in the relative intensities of the bands around 350 cm^{-1} (combined motion involving both the C-S and the ring) and the one around 1560 cm^{-1} (corresponding to the aromatic ring stretch). While the former is more intense in the case of the non-networked substrates, the latter is more intense in the networked structures. The higher intensity of the 350 cm^{-1} may be due to a higher proximity of the thiolate part of the molecule in the case of non-networked structures.

Bar diagrams showing the relative spectral intensities for different peaks on different networked substrates are presented in Figure 3.16.

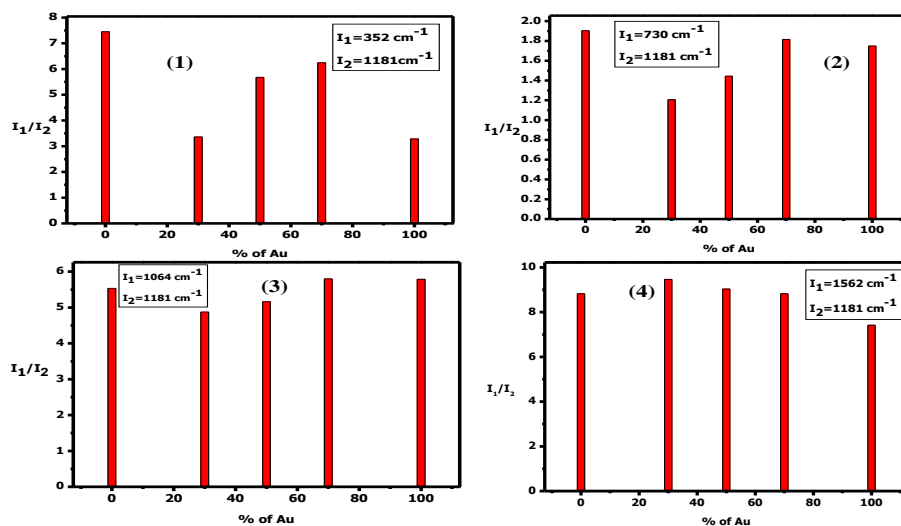


Figure 3.16. Bar diagrams showing relative intensity ratios for different peaks for substrates of different bimetallic compositions of Au and Ag.

It is observed that each peak behaves differently in terms of the intensity enhancement with respect to the different substrates, plausibly indicating that the molecular binding and orientation could be different for different bimetallic compositions.

3.3.2.3. Plasmon resonant and near-resonant SERS

In the plasmon-resonant case discussed in the introductory part of this Chapter, both λ_{exc} and the λ_{max} should coincide or should be very close. When these two do not coincide, but are still lying close, one can describe it as a near resonant condition. These conditions are achieved in the case of the SERS studies carried out using the 532 nm excitation line of a micro Raman spectrometer using the non-networked Au, Ag, and AuAg alloy NP substrates with well-defined LSPR. Typically, in the case of the Au NPs, the λ_{max} (530 nm) almost coincides with the λ_{exc} (532 nm). For other systems, the λ_{max} of the alloys vary between that for pure Au and that for pure Ag (around 420 nm).

A comparison of the ordinary Raman spectra of 1, 4-BDT with that of SERS spectra obtained from the non-networked monometallic and alloy nanoparticle SERS substrates using 532 nm excitation wavelength laser is shown in Figure 3.17.

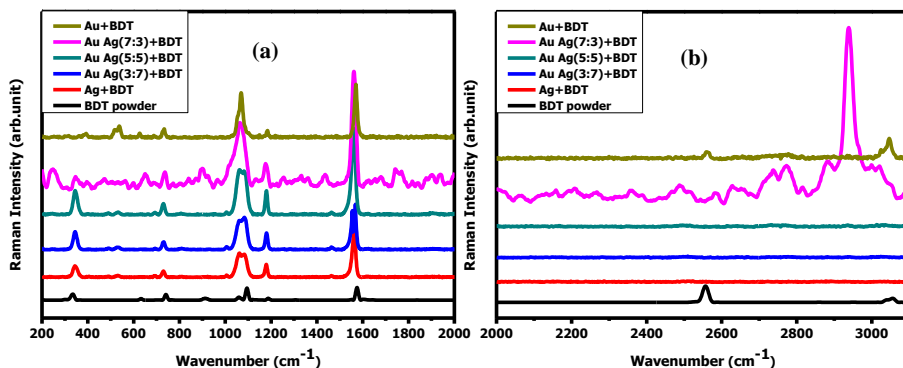


Figure 3.17. Plasmon resonant and near resonant SERS of 1, 4, BDT using 532 nm laser excitation. The black curve corresponds to the ordinary Raman spectrum and the rest are the SERS spectra of Ag, Au and Au- Ag alloys of different composition as described: (a) 200–2000 cm⁻¹; (b) 2000 – 3100 cm⁻¹.

It is very interesting to note that one observes significant differences between the spectra recorded using the 1064 nm and 532 nm excitation lines. Generally, all peaks are less intense and less resolved in the 532 nm spectra as compared to the 1064 nm spectra. The intense peak at 352 cm^{-1} in the 1064 nm spectra are generally very weak in the 532 nm spectra. Also, the peak around 1150 cm^{-1} , corresponding to the ring breathing vibrational mode has considerably broadened in comparison to the 1064 nm spectra. It is also interesting to note that the plasmon-resonant SERS spectra of 1-4 BDT obtained using the AuNP substrate is quite unique in comparison with plasmon near resonant spectra recorded using the alloy NP substrates. In the plasmon-resonant spectrum, the 352 cm^{-1} peak is almost absent indicating only a very weak interaction between the metal and thiol part. This shows that there is no enhancement in the C-S mode intensity, may be due to the poor binding of the sulfur atom with the Au surface. Also, the peak corresponding to the S-H stretch is weakly present in the spectrum around 2550 cm^{-1} . This is indeed curious since the S-H peak is absent in the near resonant spectra. It is also important to note that all the spectra are recorded using the same sample. One also observes significant changes in the spectral region around 1560 cm^{-1} corresponding to the ring C-C stretch for the various systems and is presented in Figure 3.18.

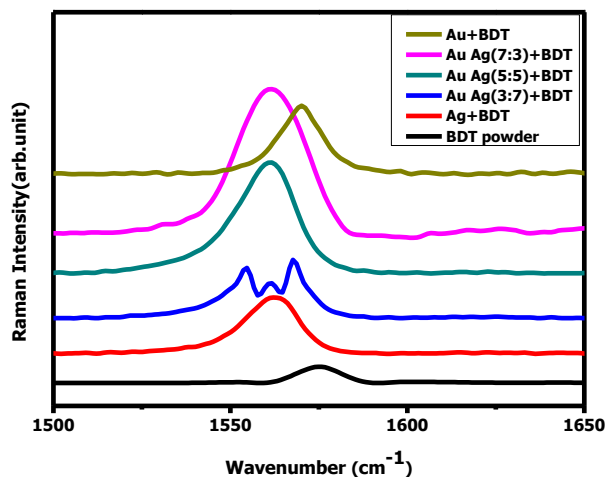


Figure 3.18. 532 nm SERS spectra of 1,4- BDT for Au, Ag, and AuAg alloy NP systems in the region corresponding to the ring C-C stretch.

In fact, one observes that the peak for the Au NP system occurs at a higher wave number as compared to those of the alloys. In fact, the peak for the alloy systems is rather broad and even undergoes splitting in the case of the AuAg (3:7) substrate indicating that there are different modes of binding and orientational preferences for 1,4-BDT on the various substrates. This is also supported by the occurrence of the aromatic C-H stretch of the molecule in the AuNP spectrum. Please see Figure 3.19. From the above one may draw the following conclusions. The 1,4-BDT is oriented at an angle to the Au surface, leaving it neither parallel or perpendicular to the surface, with one of the S-H bonds being left as such. This is also supported by the presence of the aromatic C-H stretch. In the case of the Ag as well as the alloy NP systems, the molecule is presumed to be oriented parallelly to the surface making the S-H stretch and the C-H stretch vanishing or very weak as a result of the electromagnetic selection rules. The occurrence of a strong peak

corresponding to the aliphatic C-H stretch in the AuAg alloy (7:3) may be arising from the C-H of CA. The rather poor S/N ratio of the peak also points to this. The absence of the 352 cm^{-1} peak for the AuNP system with 532 nm excitation may be related to the resonant excitation of the LSPR and the consequent weakening of the Au-S bond.

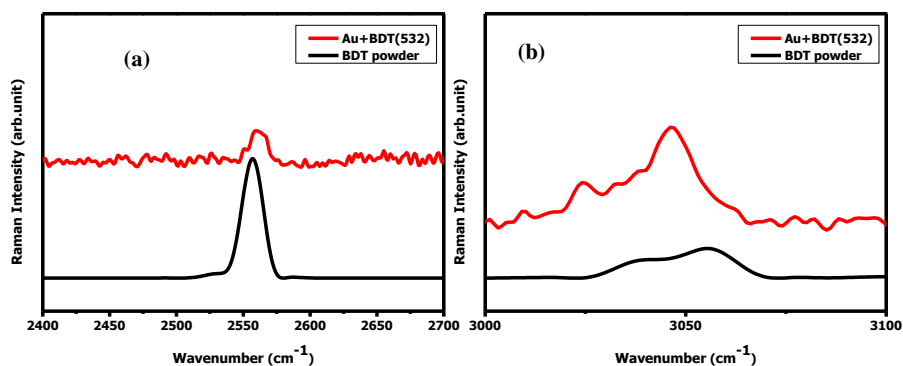


Figure 3.19. Powder Raman spectrum (black curve) and 532 nm AuNP SERS spectrum of 1,4-BDT (red curve): (a) S-H stretching region; (b) aromatic C-H stretching region.

A detailed analysis of Raman spectral band positions and corresponding vibrations of 1,4- BDT powder, SERS spectra of 1,4 BDT resulting from plasmonic metal and alloy substrates using 532nm and 1064nm excitation is given in Table 3.1.

Table 3.1. Raman bands with their assignments in the ordinary Raman spectrum and SERS spectra of 1,4-BDT using 1064nm laser and 532 nm laser.

Band assignments	Ordinary Raman spectra of 1,4-BDT powder (cm ⁻¹)	SERS assignments (cm ⁻¹) 532 nm laser					SERS assignments (cm ⁻¹) 1064 nm laser				
		Ag	Au Ag (3:7)	Au Ag (5:5)	Au Ag (7:3)	Au	Ag	Au Ag (3:7)	Au Ag (5:5)	Au Ag (7:3)	Au
C-S stretch and ring stretch	333	346	344	345	346		351	351	351	353	352
Ring stretch	630	-	-	-	-	629	-	-	-	-	-
Ring stretch	743	730	730	730	737	732	731	733	733	735	734
C-S-H bend	916	-	-	-	-	-	-	-	-	-	-
Ring C-C-C stretch	1077	1073	1072	1074	1066	1069	1074	1071	1070	1069	1075
Ring out of plane stretch	1102	-	-	-	-	-	-	-	-	-	-
Ring wagging	1188	1179	1180	1179	1177	1184	1183	1180	1180	1179	1178
Ring C-C-C stretch	1585	1562	1561	1561	1561	1570	1558	1561	1560	1560	1556
S-H stretch	2565	-	-	-	-	2558	-	-	-	-	-
Ring C-H stretch	3062	-	-	-	-	3045	-	-	-	-	-

3.3.2.4. FT-SERS Spectra of other dithiols on networked and non-networked substrates

We also investigated the FT-SERS spectra of different dithiols such as 1,2, BDT, 1,3-BDT, to examine how their SERS spectra could vary based on the different substrates. Their respective FT-SERS spectra recorded on networked and non-networked Au, Ag, and various alloy NP substrates are presented in Figures 3.20 and 3.21.

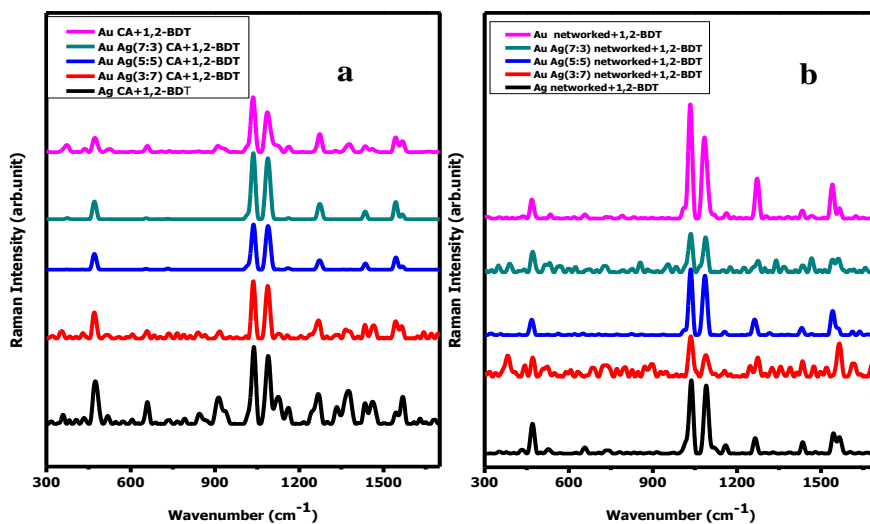


Figure 3.20. FT SERS spectrum of 1,2-BDT over (a) non-networked Au, Ag and their alloy NP substrates (b) over networked Au, Ag and alloy NP substrates.

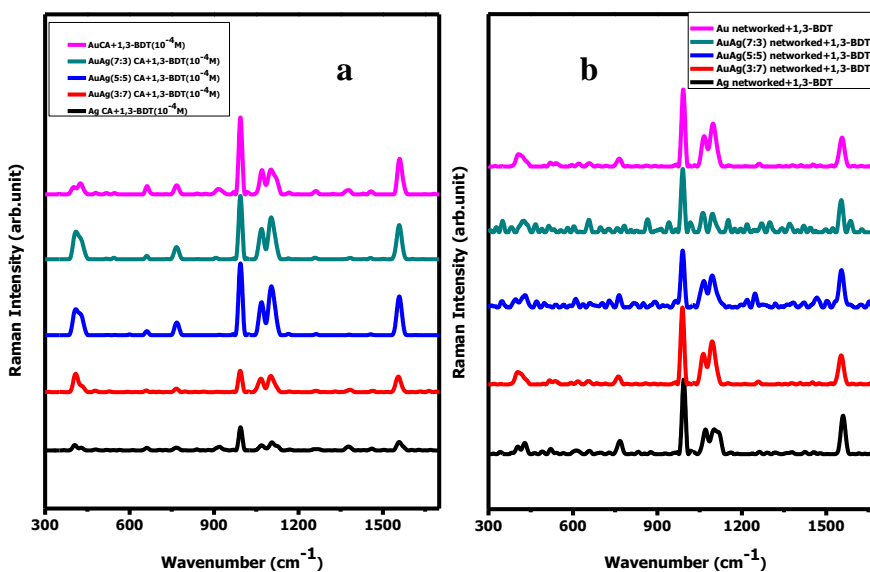


Figure 3.21. FT SERS spectrum of 1,3-BDT over (a) non-networked Au, Ag and their alloy NP substrates (b) networked Au, Ag and alloy NP substrates.

It may be observed that there are only minor differences in the FT-SERS spectra obtained on non-networked and networked substrates for 1,2-BDT and 1,3-BDT. It is however, worth noting that the peak at 352 cm^{-1} is more prominent for the plasmonic (non-networked) alloy NP substrates as compared to their monometallic counterparts in the case of 1,3-BDT. For the networked NP substrates, on the other hand, this peak is less prominent in the case of the alloys. However, no such significant differences are observed for the 1,2-BDT. This difference may be because of the possibility of more rigid binding configurations for 1,2-BDT on the metal and alloy surfaces.

3.4. Conclusions

Surface-enhanced Raman spectra are unique with dependence on the nature of the substrate, λ_{max} corresponding to the LSPR of the individual nanoparticles, possibilities of other local field enhancement mechanisms, molecular orientation, mode of binding of the molecule, proximity of the surface, etc. In that way the SERS spectra could be significantly dependent on the typical experimental conditions unlike the normal powder Raman spectra. However, it has the additional capabilities of providing enhanced detection limits as well as the nature and strength of the interactions between the analyte molecule and the surface. In this chapter, we have focussed the differences between the plasmon-resonant, near-resonant and non-resonant SERS spectra for molecular systems based on the individual nanoparticle surface. We have selected only di thiols which bind to the metal surface through the thiol group, without allowing much scope for competitive binding

possibilities. Our studies revealed that there could be significant differences between the Plasmon-resonant and non-resonant spectra as evidenced by changes in the SERS spectra of 1,4-BDT under different experimental conditions. In the case of alloys, the near- resonant spectra also present notable differences providing insights into the orientational aspects of the molecules.

CHAPTER 4

FT-SERS studies of Methylene Blue and Rhodamine 6B on Au, Ag and Au Ag alloy nanoparticle (NP) embedded cotton fabrics

4.1. Introduction

As discussed in Chapter 3, there are several factors that decide the quality of the SERS spectra and the molecular level information that one can extract from the same, primarily based on the selection rules on the basis of the SERS enhancement mechanisms. Some of them are the shape of the nanoparticles, influence of the relative positions of λ_{exc} and λ_{max} , and the dielectric constants of the materials. There have also been discussions on how SERS enhancement varies between various metals, revealing that the SERS enhancement of Ag exceeds that of Au, which exceeds that of Cu due to the parameter ϵ_b (the contribution of interband transition to the dielectric function), when ϵ_b is large, the width of the resonance increases and SERS enhancement decreases.¹⁹⁸

Generally, the surface selection rules discuss the modification of the band intensities of spectra due to the proximity of the particular atoms or groups to the metallic NP surface is often an interesting issue. Such studies have been employed often to identify the surface orientation of the molecule and the mode of binding. For example, Moskovits et al had reported two chemically plausible orientations of Pthalazine on Ag, one lying down on the surface through π interaction and the other standing up on the Ag surface via σ -bonding through two lone pairs on

the Nitrogen atoms.¹⁹⁹ They also suggested that SERS intensities of vibrational modes of an adsorbed molecule belonging to different irreducible representations may be understood qualitatively and quantitatively on the basis of the relative magnitudes of the normal and tangential components of the EM fields at the surface of an illuminated small conducting sphere. In SERS, the prediction of molecular orientation is based essentially on the extent of electromagnetic field enhancement of vibrations normal to the metal surface. Carron et al reported Raman spectra of noble metal phenyl thiolates and the corresponding SERS spectra of surface species on Cu, Ag, and Au from the tilt, axial angle of the molecular Z axis and also from the possible rotation of the molecule about the molecular Z axis.²⁰⁰ Metal adsorbate binding which contributes to chemical enhancement in SERS can be understood from the orientation of the molecule at surfaces and reactivity of the adsorbed species. Joy and Srinivasan had demonstrated how one can arrive at molecular orientation from the SERS spectra.²⁰¹

FT-SERS is found to be a major tool in art conservation for analysis and used in the identification of archaeological tissues, paints and pigments and studies on degradation of textiles.²⁰² One of the major disadvantages of Raman spectroscopy is interference from fluorescence.²⁰³ SERS allows for an enhanced Raman signal and provides substantial quenching of fluorescence on noble metal NPs. Fibre-based SERS substrates exhibit porosity, sample storage capacity, light weight, easy disposability, handiness, flexibility, in addition to renewability of natural fibre materials.²⁰⁴ Eventhough paper-based SERS sensors are gaining huge interest they lack reusability.²⁰⁵ It has been found recently

that textiles are ideal for support for wearable biosensors, since these are soft, flexible, strong and light.²⁰⁶ Fabrics coated with Metal NPs are recently explored by Chakraborty et al.²⁰⁷ He used Ag clusters on cotton and silk. In another study Kim et al has shown that it is possible to observe the exchange reaction between Benzene Thiol and 4-Nitro Benzene Thiol by SERS using cotton fabrics.²⁰⁸ Cotton threads were used to detect various analytes by Ballerini et al.²⁰⁹ These threads can be incorporated into apparel for the detection of biohazards in war front. Brosseau et al has used metal coated fabric known as Zari to design SERS substrates and was successful for the detection of 4, 4'-Bipy and Adenine.²¹⁰

In Chapter 3, we have also demonstrated the preparation of alloy NPs with tunable λ_{max} values and their impact on the SERS spectra. Alloying is also significant from another perspective. Alloying ensures that there will be different types of metal atoms on the NP surface. For example, for the AuAg alloys, we will have both Au and Ag atoms on the surface. With molecules having different binding sites -such as carboxylate, thiol, or amino groups, one can expect some preferential binding of these groups to specific metal atoms on the surface. This may be related to the relative softness of the individual atoms involved in such binding and the effective charge balancing brought about between the surface and the ligand groups. This has been an interesting aspect even in matters such as solvation of metal ions in different solvents. For example, while Ag⁺ ions show very poor solvation in water, it gets very well solvated in a generally less polar solvent like acetonitrile. From the same principles, one would expect preferential binding of multi-dentate molecules on alloy nanoparticles. For example, while thiols bind both

with Ag and Au substrates well, in the event a molecule has both sulfur- and nitrogen -based ligands, the sulfur might prefer for binding with the Au atoms and the nitrogen atoms with Ag atoms on an alloy surface, if the molecular geometry allows that.

For studying this selectivity of binding, in this Chapter, we carried out systematic SERS studies of Methylene Blue (MB) and Rhodamine 6B (R6B) dye molecules on Au, Ag, and AuAg alloy NP-based cotton fabric SERS substrates using 1064 nm excitation. MB contains fused aromatic rings with both N and S attached and also N atoms attached to the side chain alkyl groups. In R6B there are fused rings with O as the hetero atom. So, there is possibility for selective binding and orientational preferences based on the individual substrates.

Structure of MB and R6B

Molecular structures of MB and R6G are presented in Figures 4.1 and 4.2.

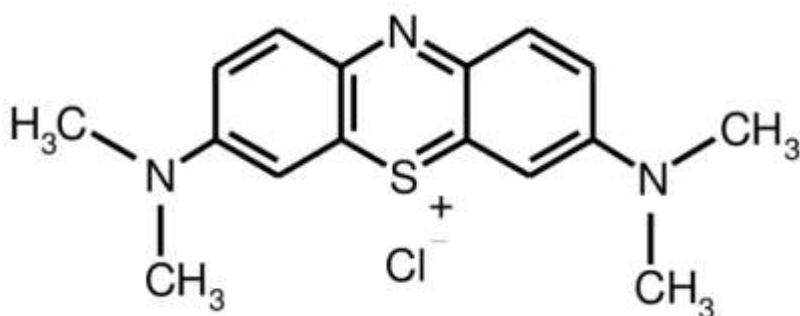


Figure 4.1. Molecular structure of MB

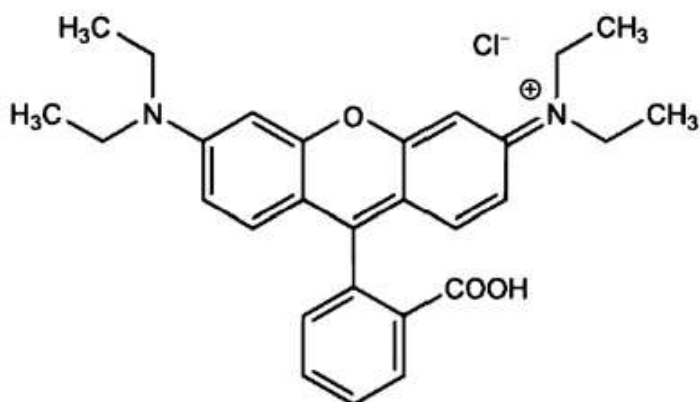


Figure 4.2. Molecular structure of MB

The UV-Vis spectra of these compounds are presented in Figure 4.3.

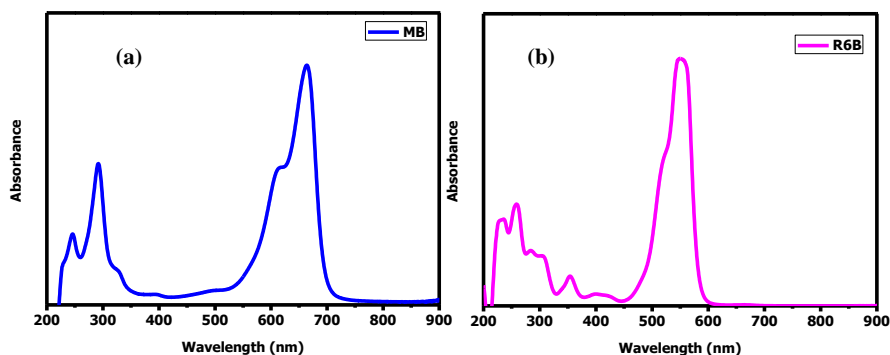


Figure 4.3. UV-VIS absorption spectra of aqueous MB (a) and R6B (b)

MB shows strong absorption band at 664 nm with a shoulder peak at 620 nm. Strong band is due to $n \rightarrow \pi^*$ transition and the shoulder due to 0-1 vibronic transition. Here we have taken 10^{-4} M aqueous dye solutions. Since the dimerization of MB molecules can be readily detectable by a hypsochromic shift of the absorption, our UV- VIS

spectra suggest the existence of MB as monomer, due to the absence of above said shift. R6B shows strong absorption at 552 nm.

4.2. Experimental details

Preparation Cotton fabric substrate incorporated with Au, Ag, Au-Ag alloy NP

As discussed earlier, Au, Ag, and AuAg alloy NPs prepared as per the method described by Raveendran et al.⁴⁷ 0.05M HAuCl₄ and 0.05M AgNO₃ (in the required stoichiometric compositions), were taken as precursors. 1000µl 0.01M NaOH was added to microwave heated solution containing metal ion precursors, reducing agent and capping agent. Cotton fabric pieces in square shape was put into each of the beakers containing metal and alloy NP sol. It was kept in an oven at 60°C for overnight soaking and drying.

4.3. Results and discussions

Photographic images of metal and alloy NP sols and cotton fabrics incorporated with these NPs are shown in Figure 4.4. A and Figure 4.4. C, respectively. One observes a gradual colour change from yellow to purple as the percentage of Au content increases as seen from image 4.4.A (i)-(v). But the dried cotton fabrics present slightly different colours compared to their respective sols, plausibly due to limited aggregation and resulting inter plasmonic coupling. The UV-VIS absorption spectra of Au, Ag and their alloy NP sol are presented in Figure 4.4.B. All the bands are characterized by a single peak, confirming the formation of homogeneous alloys. Normalized

absorption spectra clearly show red shifting of LSPR as Au content increases. In the case of alloys, spectra are broader and also fullwidth at half maximum is higher when compared to Au and Ag absorption spectra. As described earlier, this may be due to faster relaxation because of the microheterogeneity present in the alloy systems. The UV-DRS spectrum of the cotton fabrics coated with metal and alloy NPs presented in Figure 4.4.D shows broader absorption and red shifting of absorption peak, may be due to inter plasmonic coupling resulting from increased plasmon density. Interparticle interactions also play an important role in the optical absorption of the NPs.

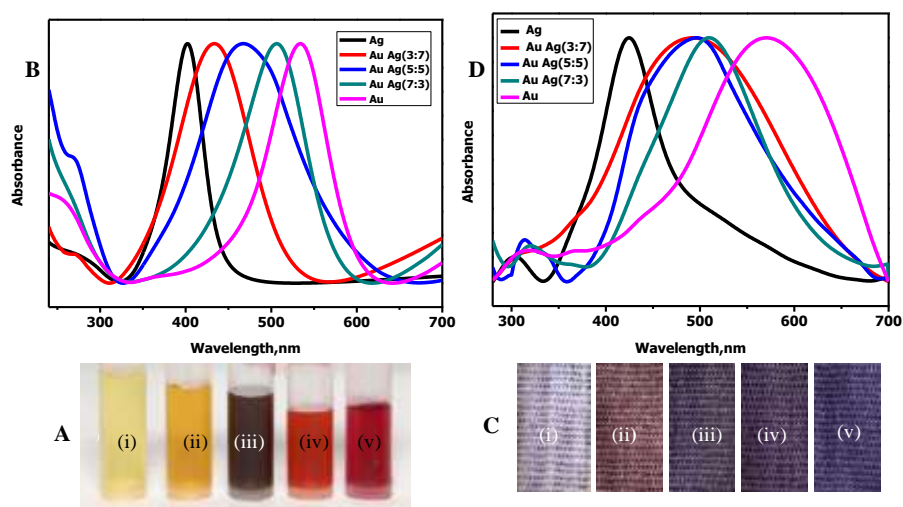


Figure 4.4. (A): (i) – (v) Photographic images of sols Ag NP, Au Ag(3:7) NP, Au Ag(5:5) Au Ag(7:3) NP, Au NP; (B) -normalized UV-VIS absorption spectra of NP sols (i)-(v); 4.4. C: (i)– (v) Photographic images of cotton fabrics coated with Ag NP, Au Ag(3:7) NP, Au Ag(5:5) Au Ag(7:3) NP, Au NP; (D) UV-DRS of the NP - coated cotton fabrics shown in C (i) – (v).

As a typical study, the FE-SEM images and the EDAX spectrum corresponding to the cotton fabric coated with Au NPs is presented in Figure 4.5.

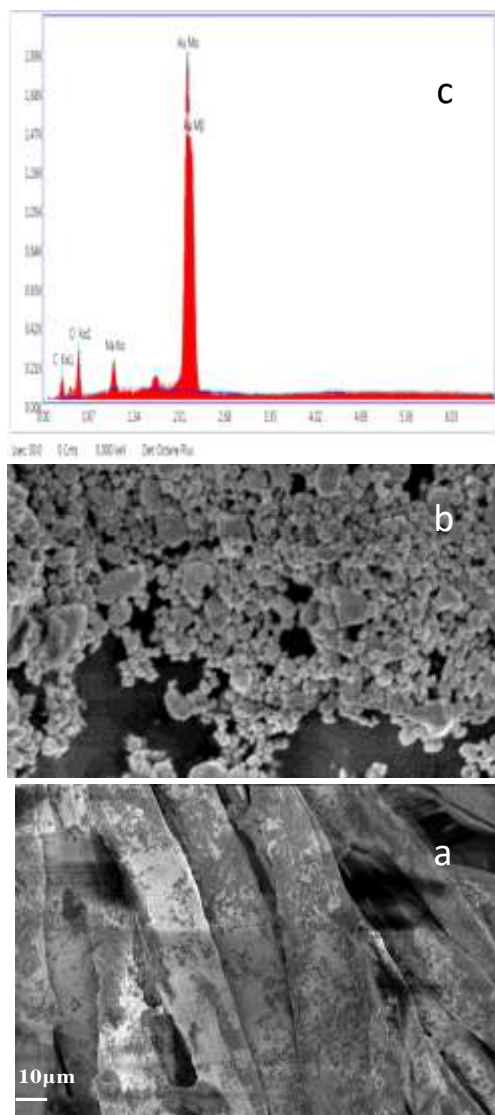


Figure 4.5. (a) & (b): FE-SEM image of Au NP embedded cotton fabric at different magnifications; (c) EDAX spectra of the sample.

From the FESEM images, we could clearly observe the distribution of Au NP all over the cotton fabric. From the FESEM images, the size of the Au NP is found to be ≥ 20 nm. These closely packed NPs will aid in generating locations of greater electric fields known as “hot spots”.

4.3.1. SERS studies of MB

All the Raman spectroscopic studies of MB are carried out using Bruker FRA106 FT Raman spectrometer equipped with the 1064 nm laser. In order to assign the vibrational modes corresponding to individual peak positions correctly, we carried out ab initio quantum chemical calculations using the Gaussian 09 program to calculate the theoretical Raman spectrum of the compound. The calculations were carried out using density functional theory, employing the B3LYP functional and the 6-31+G* basis set. An empirical scaling factor of 0.9818 was used as the scaling factor, considering the frequencies of the ring C-C stretch mode in the powder spectrum and theoretical spectrum. The normal FT Raman spectrum of the powder MB and the calculated theoretical spectrum of MB are plotted together in Figure 4.6.

Methylene Blue is a widely studied analyte molecule because of its interesting geometry and there are lots of works reported in literatures on both theoretical and experimental Raman spectra of this molecule.²¹¹ Zhong et al studied adsorption orientation of MB on the silver colloid using SERS and DFT.²¹² According to SERS selection rule, the normal modes of vibrations with the polarizability derivative components perpendicular to the surface of NP will be enhanced more. From this perspective, they concluded that the enhancement of bands

corresponding to in-plane bending vibration, i. e., the CSC skeletal deformation and band at 1029 cm^{-1} , as a result of perpendicular orientation of MB on Ag NP surface at higher concentration. While a parallel orientation will enhance bands associated with out-of-plane vibrations such as band at 657 cm^{-1} correlated to skeletal deformation and bands at 688 and 801 cm^{-1} to the CH out-of-plane bending modes.

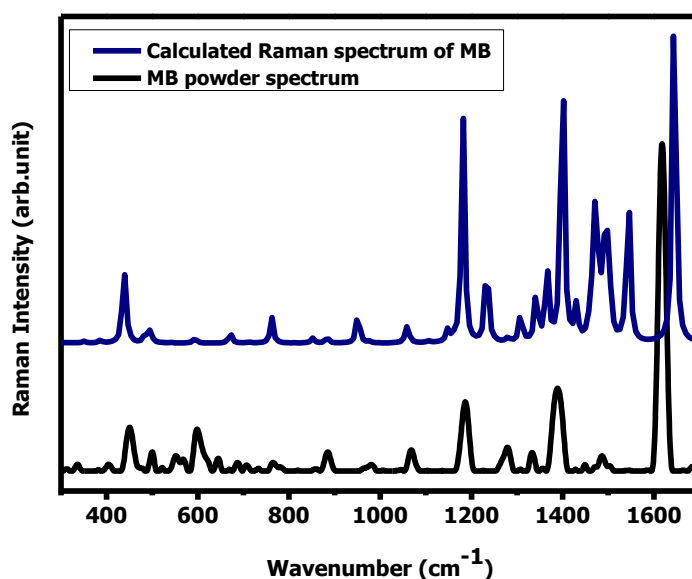


Figure 4.6. Ordinary FT-Raman spectrum of MB and calculated Raman spectrum.

The SERS spectra of MB show significant differences over Au, Ag and Au- Ag alloy substrates (Figure 4.6). Eventhough the SERS spectra of MB on Au and Ag substrate shows closer similarities in terms of peak positions, the relative intensities of the peaks vary, plausibly due to orientational differences. In fact, the SERS of MB from the alloy substrates are completely different, suggesting a totally different molecular orientation and binding.

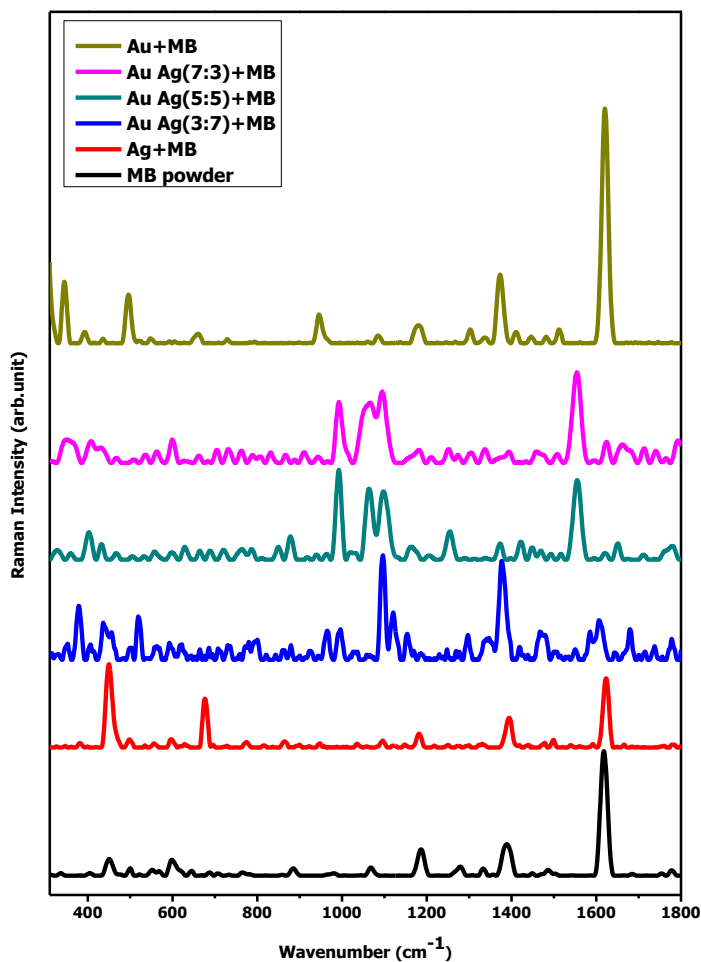


Figure 4.6. SERS spectra (10^{-4} M) on Ag NP, Au Ag (3:7) NP, Au Ag (5:5) NP, Au Ag (7:3) NP, Au NP -embedded cotton fabric. Powder FT Raman spectrum of MB is also shown.

There are four potential sites for the MB molecules to bind with the metal surfaces, i.e., N and S atoms of the thiazine ring, N atom attached to the methylene groups and finally the thiazine ring itself. In the SERS spectrum from the Ag substrate, we clearly see a weak intensity for the ring C-C-C stretching at 1617 cm^{-1} compared to peak at 450 cm^{-1} which could suggest that molecule is not lying completely normal to the

surface. In addition, the out-of-plane C-H bending peak at 675 cm^{-1} shows strong enhancement that may be resulting from a more parallel orientation. Metal-adsorbate bond formation at 244 cm^{-1} suggest the formation of Ag-N bond (Figure 4.7 (a)). In the SERS spectrum from the Au NP surface, one observes an enhancement of the band at 499 cm^{-1} (resulting from $\alpha(\text{CNC})_{\text{AMG}}$). Most of the in-plane vibrations are enhanced and also the most intense peak is due to ring C-C-C stretching that suggest perpendicular orientation of MB on Au surface. Metal adsorbate bond formation can be seen at 274 cm^{-1} suggesting Au-S bond formation due to the soft-soft interaction of Gold and Sulphur (Figure 4.7 (a)).

SERS spectra from the alloys in the region between 950 cm^{-1} and 1100 cm^{-1} has shown notable enhancement of peaks resulting from vibrations due to $\rho\text{ CH}_3$, $\beta\text{ CH}_3$ and $\delta\text{ C-S-C}$, $\nu\text{ C-C-C}$. Also, the ring C-C-C stretching band at 1620 cm^{-1} is very weak. It is also observed that the peaks corresponding to the asymmetric ring C-C-C stretching at 1550 cm^{-1} is enhanced. Metal-adsorbate region (Figure 4.7 (b)) suggest multiple binding due to Au-S and Ag-N formation on alloy substrate. Since most of the in-plane vibrations are absent, this suggests a completely parallel orientation of MB over alloy surface and binding through both Sulphur and Nitrogen.

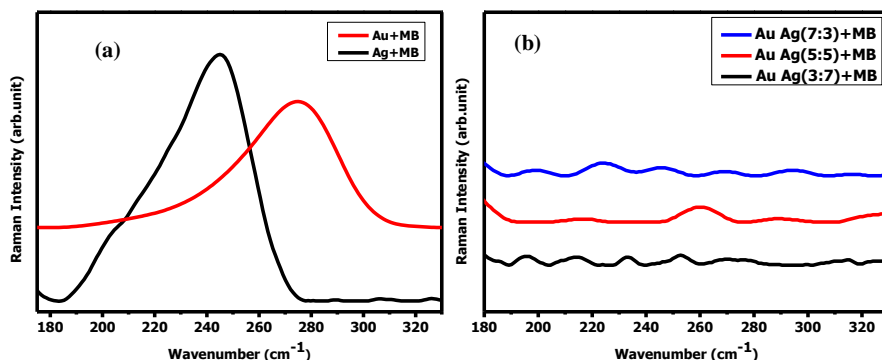


Figure 4.7: (a) SERS spectral region corresponding to metal-adsorbate bond formation in Au- and Ag -embedded cotton fabric for MB; (b), the same spectral region for the SERS spectra from the in AuAg alloy embedded cotton fabric for MB.

The complete assignment of the various peaks is given in Table 4.1.

For brevity, the SERS spectra of MB on the various substrates in the region $1500 - 1650 \text{ cm}^{-1}$ is presented in Figure 4.8. Remarkable variations observed in the relative intensities of the ring C-C-C vibrations can be seen from the figure 4.8. Both Au and Ag surfaces shown a similar ring C-C-C stretching at 1620 cm^{-1} for Ag and 1623 cm^{-1} for Au and this vibration corresponds to symmetric aromatic C-C-C stretching. But in the case of alloys although this peak present with low intensity, asymmetric ring C-C-C stretching at 1554 cm^{-1} is observed to get enhanced.

Table 4.1. Assignment of the various Raman peaks in the calculated, powder and SERS spectra.

	Calculated Raman spectra (cm ⁻¹)	Ordinary Raman spectra (cm ⁻¹)	SERS spectra of MB from Ag fabric substrate (cm ⁻¹)	SERS spectra of MB from Au fabric substrate (cm ⁻¹)	Vibrational band assignments
Region below 1000 (cm ⁻¹)	446	450	451	434	α (CNC) _{AMG} , δ (CNC) and δ (CSC) _{Thiazene ring}
	493	499	496	496	α (CNC) _{AMG}
	605	600	596	600	α (CNC) _{AMG}
	683	675	675	658	γ (CH)
	776		772	727	ν (CS) _{ring} , ν (CN) _{AMG} , β (CH)
		885	864		ν (CCC) _{ring}
	969	962	945	945	ρ (CH ₂), β (CH)
Region between 1000 and 1500 (cm ⁻¹)	1080	1067	1094	1084	β (CH), α (CCC) _{ring}
	1169	1186	1181	1180	ρ (CH ₃), β (CH)
	1203				ρ (CH ₃), β (CH)
	1256	1277			ρ (CH ₃), β (CH)
	1304	1305		1300	β (CH), ν (CN) _{ring}
	1332	1332		1337	ν (CCC) _{ring} , β (CH)
	1367	1355			ν (CCC) _{ring} , β (CH), (CH ₂) _{wagg} , α (CNC) _{AMG}
	1390	1388	1394	1371	ν (CN) _{ring}
	1425			1410	α (NCH) _{AMG}
	1457			1446	(CH ₂) _{sciss} , (CH ₂) _{wagg} , β (CH)
1496			1480	(CH ₂) _{twist} , β (CH)	
Region above 1500 (cm ⁻¹)	1526	1503		1511	ν (C ₉ -N ₁₀), ν (C ₃ -N ₂), (CH ₂) _{sciss} , (CH ₂) _{twist}
	1567	1542			ν (C ₉ -N ₁₀), (CH ₂) _{sciss} , β (CH)
	1574	1585	1592		ν (CCC) _{ring} , ν (CN) _{ring}
	1675	1617	1623	1620	ν (CCC) _{ring} , ν (CN) _{ring}

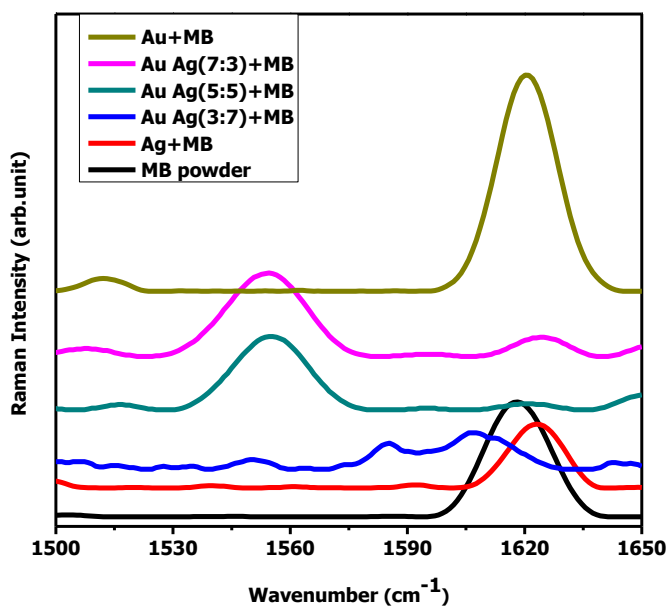


Figure 4.8. SERS spectra of MB in the region 1500-1650 cm⁻¹ showing differences in the ring C-C-C stretching mode for the metal and alloy SERS substrates. Powder spectrum of MB is also given for comparison.

Based on these observations, the following geometries may be proposed for the orientation and binding of MB on the Ag, Au, and the AuAg alloy NP substrates:

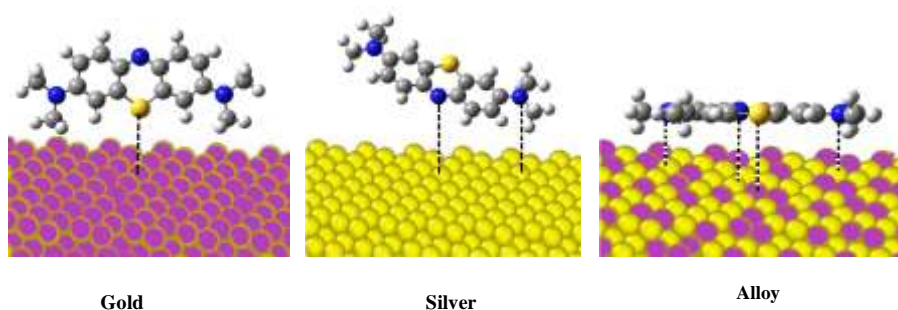


Figure 4.9. Mode of binding and orientation of MB on Au, Ag and AuAg alloy substrates.

4.3.2. SERS of R6B

The calculated (after empirical scaling) and powder FT-Raman spectra of R6B are presented in Figure 4. 10. Assignments are given in Table 4.2.

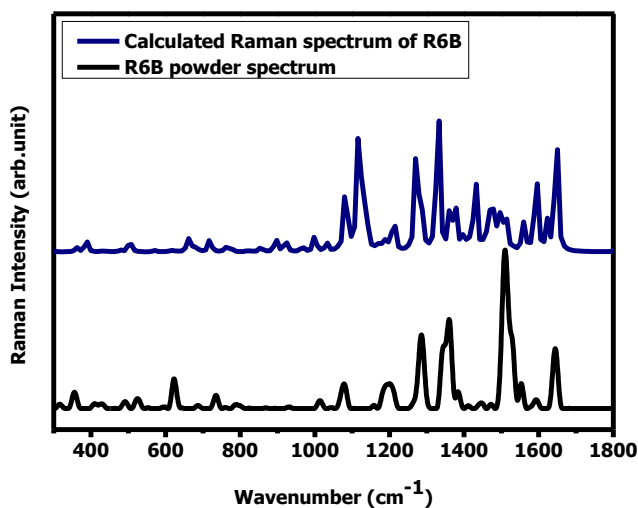


Figure 4.10. Ordinary Raman spectrum of R6B and calculated Raman spectrum.

SERS spectra of R6B (10^{-4} M) over Au, Ag and their alloy substrate of three different compositions (3:7,5:5,7:3) are shown in Figure 4.11. In the Powder Raman spectrum, there are six prominent peaks observed at 1644cm^{-1} , 1509cm^{-1} , 1360cm^{-1} , 1282cm^{-1} , 1031cm^{-1} , 491cm^{-1} . Out of these, the peak corresponding to the Xanthene ring stretching at 1509cm^{-1} is the most intense one. For a better understanding of each vibrational mode, assignments of the individual peaks are carried out using the GaussView visualization software. Detailed assignment of each peak in the Raman and SERS spectra are

given in the Table 4.2. It can be seen that the SERS spectra are weak for the substrates Ag and AuAg (3:7). Highest enhancement is observed from the Au substrate. The intense peak at 1001 cm^{-1} arises primarily from the ring breathing mode of the Benzoic acid ring with contributions also from $\nu_{\text{assym}}(\text{C-C-C})$, $\nu_{\text{assym}}(\text{C-O-C})$, $\nu(\text{C-N})$, and C-H wagging. While comparing the SERS spectra of R6B on Au, Au Ag (7:3) and Au Ag (5:5) substrates it is clear that only SERS spectra from the Au substrate shows a peak at 1642 cm^{-1} corresponding to free carbonyl ($>\text{C}=\text{O}$) stretching frequency of carboxylic acid, indicating the presence of free carboxylic acid group. This is further confirmed by the presence of Au-N bond at 265 cm^{-1} (shown in Figure 4.12), suggesting adsorption of R6B on Au surface through N atom of the diethyl amino group and the same band is missing in the case of Au Ag (7:3) and Au Ag (5:5) substrates.

Since the peak corresponding to carboxylic acid is missing in the SERS from the AuAg (7:3) and AuAg (5:5) substrates, these molecules may be adsorbing through carboxylate ions (COO^-) ion, subsequent to deprotonation. This is further confirmed by the enhancement in the bands at 1385 and 1414 cm^{-1} corresponding to the OCO bands of the carboxylate groups.

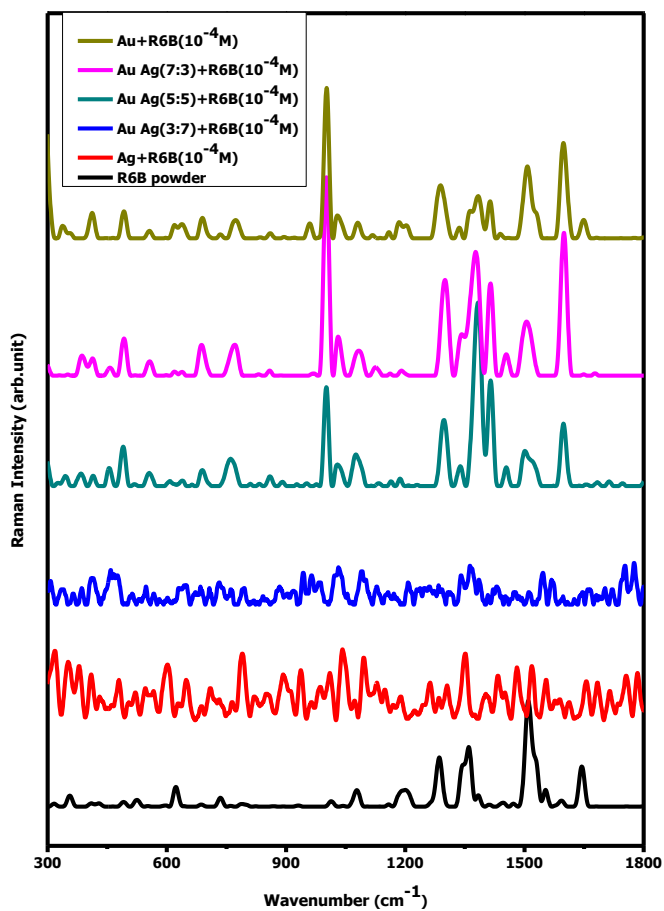


Figure 4.11. SERS spectra of R6B (10^{-4} M) on Ag NP, Au Ag (3:7) NP, Au Ag (5:5) NP, Au Ag (7:3) NP, Au NP -embedded cotton fabric. Powder spectrum of R6B is also given for a comparison.

Since there is enhancement in both benzoic acid and Xanthene ring vibrations that suggest both the rings are normal to the surface.

Table 4.2. Assignment of various bands in the powder and SERS spectra of R6G over different substrates.

	Ordinary Raman spectrum of R6B powder	SERS spectrum from Au Ag(5:5) substrate	SERS spectrum from Au Ag(7:3) substrate	SERS spectrum from Au substrate	Vibrational assignments
Region above 1500 cm ⁻¹	1642 cm ⁻¹	1651 cm ⁻¹	1649 cm ⁻¹	1649 cm ⁻¹	Carbonyl stretching+ Ring ν_{asym} (C-C-C)+ ring with COOH stretching
	1591 cm ⁻¹	1597 cm ⁻¹	1597 cm ⁻¹	1599 cm ⁻¹	Ring ν_{sym} (C-C-C)+C-H wagging
	1509 cm ⁻¹	1507 cm ⁻¹	1507 cm ⁻¹	1507 cm ⁻¹	AMG rocking+ring deformation
Region between 1000-1500 cm ⁻¹	1410 cm ⁻¹	1414 cm ⁻¹	1413 cm ⁻¹	1413 cm ⁻¹	OCOstretch+ Ring ν (C-C-C)+ ν (C-N)+methyl group rocking+C-H wagging
	1360 cm ⁻¹	1383 cm ⁻¹	1383 cm ⁻¹	1377 cm ⁻¹	OCO stretch + C-H wagging+ring breathing+ ν (C-N)
	1283 cm ⁻¹	1297 cm ⁻¹	1287 cm ⁻¹	1297 cm ⁻¹	Ring ν_{asym} (C-C-C)+C-H wagging+AMG rocking
	1194 cm ⁻¹	1186 cm ⁻¹	1194 cm ⁻¹	1190 cm ⁻¹	C-H wagging+ ν_{sym} (C-O-C)+ δ (O-H)
	1078 cm ⁻¹	1076 cm ⁻¹	1080 cm ⁻¹	1082 cm ⁻¹	C-H wagging+ring in-plane bending
	1042 cm ⁻¹	1029 cm ⁻¹	1029 cm ⁻¹	1030 cm ⁻¹	Methyl group rocking+C-H wagging+Ring breathing
	1014 cm ⁻¹	1001 cm ⁻¹	1001 cm ⁻¹	1001 cm ⁻¹	Benzoic acid ring breathing+Methyl group rocking+ C _x - C _x - C _x bending+ C _x - H wagging
Region below 1000cm ⁻¹	865 cm ⁻¹	858 cm ⁻¹	859 cm ⁻¹	857 cm ⁻¹	COOH attached ring C-H wagging+xanthene ring in-plane breathing vibration

761 cm ⁻¹	759 cm ⁻¹	773 cm ⁻¹	770 cm ⁻¹	Xanthene ring C-H rocking vibration
687 cm ⁻¹	688 cm ⁻¹	688 cm ⁻¹	687 cm ⁻¹	Xanthene ring & COOH attached ring breathing mode+ COOH bending
621 cm ⁻¹	623 cm ⁻¹	627 cm ⁻¹	627 cm ⁻¹	COOH attached ring out of plane bending vibration
552 cm ⁻¹	555 cm ⁻¹	555 cm ⁻¹	556 cm ⁻¹	Xanthene ring out of plane bending vibration
490 cm ⁻¹	490 cm ⁻¹	491 cm ⁻¹	491 cm ⁻¹	Ring deformation

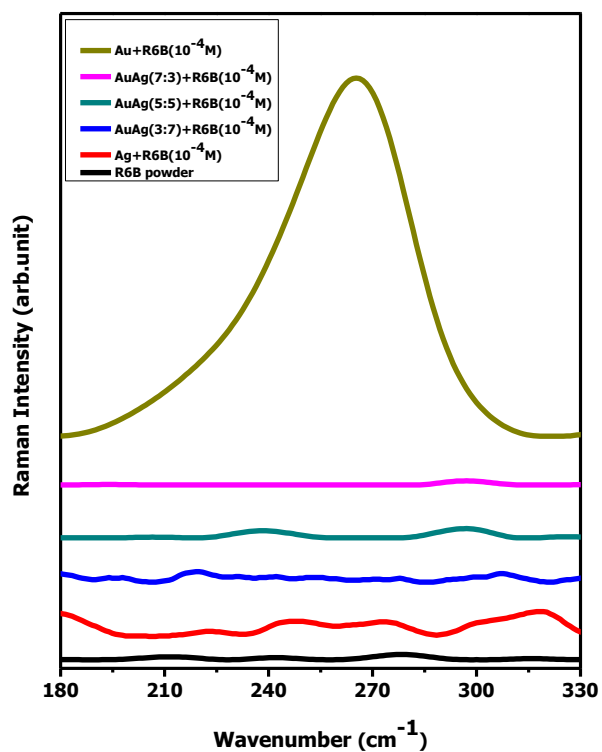


Figure 4.12. FT-SERS spectra of R6B on Au, Ag, and alloy substrates in the region 180-330 cm⁻¹.

Thus, the results indicate that the mode of binding and orientation of R6G on Au, and the AuAg alloys is very different.

4.4. Conclusions

Orientation and binding of molecules on the metal nanoparticle surface is a key factor in governing the intensity of various peaks in the SERS spectra. In this study, we have also examined the presence of different metal atoms on the nanoparticle surface by taking Au, Ag, AuAg alloy nanoparticle. Since there are different functional groups that allow different modes of binding in the model systems MB and R6G, we expect that they will bind and orient differently with respect to the surface. The results of the SERS studies clearly support this.

CHAPTER 5

Dependence of SERS spectra on the Shape/ Morphology of Ag NP substrates: Case studies of 1,4-Benzene Dithiol, Methylene Blue and Rhodamine-6B on Nanoflowers of different roughness

5.1. INTRODUCTION

As discussed in the earlier chapters, the molecular SERS spectra are dependent on several factors such as the proximity between the λ_{\max} and λ_{exc} , specific interaction between the metal NP surfaces, orientation of molecules, and the vicinity of different functional groups on multi-functional groups with respect to the surface. It is also important to investigate how the shape and the morphology of the nanoparticle substrate structures affect the SERS spectra. In fact, the shape of the nanoparticle can affect the SERS in many ways, particularly by virtue of the modifications in the electric field contributions to the SERS enhancement.²¹³ It is possible that one can tailor such structures by chemical control.²¹⁴ Depending on the growth parameters, one expects significant variations in the size and morphology of such nanostructures. It has been well documented over the years that one observes the formation of anisotropic nanostructures in cases where the spatial confinements of the growth are different in different dimensions. In such cases, the LSPR is also observed to be different along different

directions.²¹⁵ For example, for a nanorod, one observes a longitudinal plasmon and a transverse mode.²¹⁶ Shape-dependent variations in the local electric fields are also observed as in the case of the hot spots as mentioned in the previous chapters. In this Chapter, we discuss the variations in the SERS spectra as a result of such morphological modifications.

Physico-chemical controls are affected to ensure that one obtains the right environment for the growth of such morphological variants. Such anisotropic nanostructures include one-dimensional (nanorods, nanowires, nanotubes), two-dimensional (prisms, sheets, and plates, etc) and three dimensional (nanoflowers, nanostars, nanourchins, nanocubes, nanorice, etc) formations.²¹⁷ Herein, we present the observations on the differences in the SERS spectra based on the roughness of the nanoflower (NF) surface. Three different NF structures were prepared for the purpose.

The synthesis of Ag nanoflower (NF) using ascorbic acid, and poly (vinyl pyrrolidone) (PVP) as well as the one with ascorbic acid, PVP and CTAB were already reported previously.^{218,219} The use of different dicarboxylic acids along with ascorbic acid in structure directing roles in Ag NF preparation has already been investigated in detail.²²⁰ A modified method using ammonium citrate dibasic as initial complexation agent and ascorbic acid as reducing agent for anisotropic growth of Ag NF used as metallic conductive inks was also studied.²²¹ Chang et al have shown the application of Ag NF with abundant nanogaps as effective broadband plasmonic scatterers to achieve

different colours.²²² Therein, the interparticle coupling effect was attributed to abundant nanogaps and sharp tips near the surface. Therein, the nanogap density was controlled by varying the concentration of PVP. The different methods for the synthesis of morphologically different silver nanoparticles were reviewed by Khodashenas.²²³ In this review, he discusses about earlier reports towards Ag NF synthesis including wet-chemical methods using AgNO₃ and ascorbic acid by Cai and Zhai and reduction by ascorbic acid involving CTAB capping by Pourjavadi and Soleyman.^{224,225} Faseela et al reported the use of hierarchically structured silver NF for highly conductive metallic inks with reduced filler concentration.²²⁶ There, the ammonium citrate dibasic is employed as an initial complexation agent to control the anisotropic growth of silver particle, followed by the addition of aqueous ammonia and boric acid to maintain pH and finally ascorbic acid as the reducing agent. The concentration of the ascorbic acid was also observed to be a key factor in governing the bud size. Lui et al reported the controlled synthesis of hierarchical silver structures by regulating the kinetics of formation.²²⁷ Here, the amino acids used as reducing agents will also coordinate with the Ag⁺ ions to slow down the reduction process. Based on the concentration of the amino acid, the morphology of the resulting organizations gets modified from dendrites to flowers and then, to compacted spheres. El-Nagar et al has shown the use of 3D-Ag flower like microstructures for non-enzymatic amperometric detection of H₂O₂.²²⁸ In this case, the morphology is controlled by adding minute amounts of either succinic or malonic acid. Here also, the ascorbic acid is acting as the reducing agent.

The enzyme-induced reduction of Ag ions forms flower-like Ag NPs. There adenine was taken as the SERS probe.²²⁹ Wu et al has carried out the synthesis of silver NF using trisodium citrate and Canarium album Foliar Broths and tested the performance in SERS using R6G.²³⁰ There also flower like Ag NP with high anisotropy exhibited excellent SERS enhancement ability relative to the normal Ag NP (spheres and nanoplates). Application of Ag NF based structures as excellent SERS substrates were further studied by Liang et al using Ag NF prepared by PVP, ascorbic acid and AgNO₃ and was successful in detecting even 10⁻¹⁰M Malachite green isothiocyanate (MGITC).²³¹ Roy et al reported single particle SERS with 10 pm sensitivity using silver NF.²³² Here three different kinds of Ag NF particles were used as SERS substrates for probing 4-MBA molecule. Tang et al studied the application of silver sub microspheres as SERS substrates for the detection of Crystal Violet.²³³ Their sub microspheres are prepared using AgNO₃, ascorbic acid and Tween 20 that appeared like ‘meatball’ or ‘Walnut’ like structures. In another report, Oleveira et al demonstrated the use of office paper decorated with silver nano structures as an excellent SERS substrate for the detection of R6G.²³⁴

It is with this perspective in mind that we chose to investigate how the different morphological variants of Ag NFs respond to the SERS spectra. Essentially, any such difference in the SERS spectra can be correlated to the mode of binding of the molecule, LSPR, and the local electric fields experienced by the molecule at atomically rough surfaces. In this Chapter, we prepare Au and Ag nanostructures of different shapes and investigate the dependence of SERS on such structures.

5. 2. Experimental details

5.2.1. Synthesis of Ag Nanoflowers (NFs)

Three different NF systems are prepared using different combinations of the reducing and protecting agents. In all the three cases, the concentration of ascorbic acid is kept constant (.05M, 40 ml). Eventhough ascorbic acid can serve both as a reducing agent and a capping agent, an additional capping agent (soluble starch) is also employed. The combinations of the reagents used for the synthesis of the three NF systems, viz., NF1, NF2, and NF3 are given in Table 5.1. The reagents were subjected to microwave irradiation in a microwave oven. The NF dispersions obtained were then transferred into individual beakers containing Whatman filter papers. After the initial settlement of the dispersions, the supernatant liquid on top was removed using a micropipette, for each case. The films thus prepared were dried in an oven, maintained at 60 °C.

Table 5.1. Concentrations of reagents employed for the synthesis of Ag NF1, Ag NF2 and Ag NF3.

Reagents	Ag NF1	Ag NF2	Ag NF3
Ascorbic acid	0.05M (40ml)	0.05M (40ml)	0.05M (40ml)
AgNO ₃	0.01M (20ml)	0.05M (20ml)	0.05M (250μl)
Starch	Nil	1% (20ml)	1% (10ml)

5.3. Results and discussions

5.3.1. UV-VISIBLE, FESEM, TEM and XRD

Photographic images of Ag NF1-Ag NF3 sols just after preparation are shown in Figure 5.1.1 (a)-(c). As can be inferred from these figures, samples (a) and

(c) settles down faster. Absence of an absorption band corresponding to LSPR suggests that the LSPR may be absent in the system. Settled particles can be seen at the bottom of the bottle. Particles appeared in ash colour. The systems deposited on filter papers are dried in an oven at 60 °C and were used as substrates for SERS measurements. These Ag NF substrates are shown photographically in Figure 5.1.2 (a)-(c). The corresponding DRS spectra for these samples are also given in Figure 5.1.3.

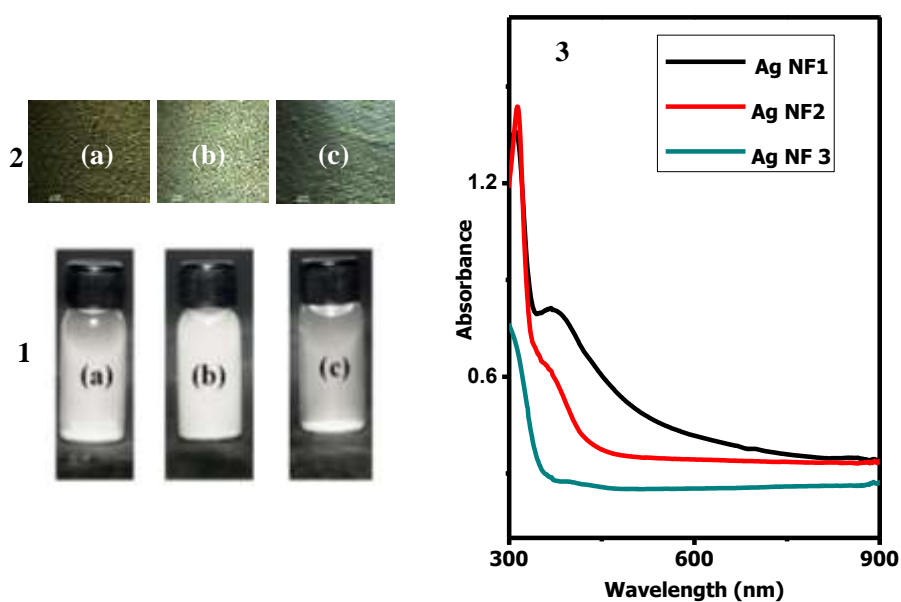


Figure 5.1:1(a)-(c) Photographic images of Ag NF1- Ag NF3 sols; 2(a) - (c) photographic images of Ag NF1-Ag NF3 substrates; 3: DRS of films in the range 300-900 nm.

The FESEM, TEM and SAED patterns of Ag NF of three different morphologies are shown in Figure 5.2. From the figure, it is clear that Ag NF1 and Ag NF3 have sharper edges as compared to Ag NF2.

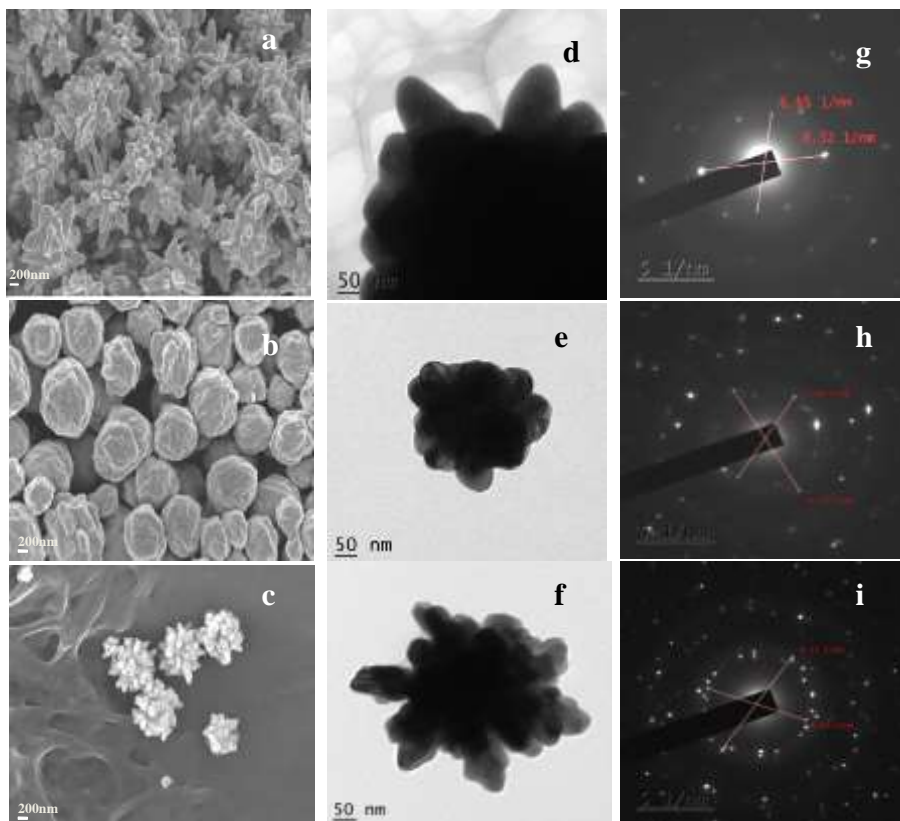


Figure 5.2: (a) – (c): FESEM images of Ag NF1-Ag NF3; (d) – (f): TEM images of Ag NF1-Ag NF3; (g) – (i): SAED patterns of Ag NF1- Ag NF3.

Crystallinity of the prepared Ag NF were further characterized by XRD. From Figure 5.3, XRD shows mainly (111), (200), (220) and (311) peaks in which (111) peak is the strongest one. These peaks correspond to FCC crystal structure of Ag NF.

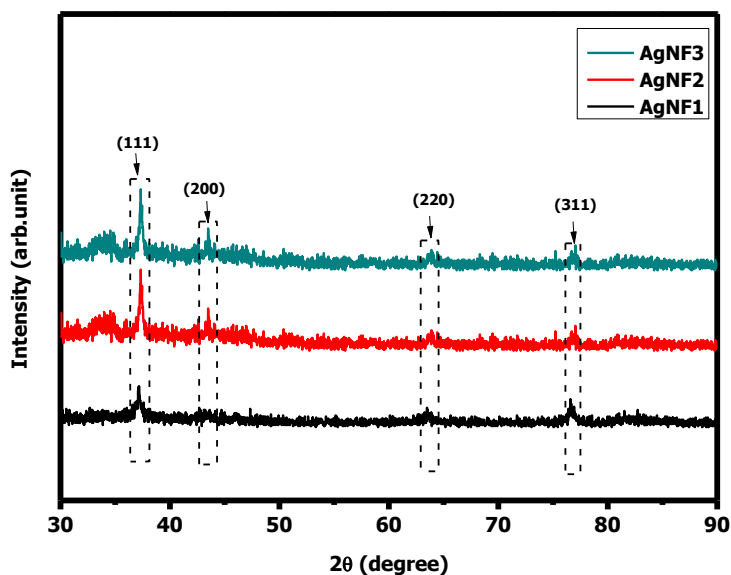


Figure 5.3. XRD of Ag NF1-Ag NF4 SERS substrates.

5.3.2. SERS studies

5.3.2.1. 1, 4-BDT

SERS studies were done using FT-Raman (1064 nm) excitation. 10^{-4} M solution of 1,4-BDT is prepared in ethanol and one drop of the solution is added to the Ag NF film, using a micropipette, kept for about 6 hours and dried at room temperature. Although all the three Ag NF SERS substrates yield good SERS spectra, the ones obtained using Ag NF1 and NF3 are more intense. This may be because of the sharper edges of the NF1 and NF3 samples as compared to NF2, as observed from the FE-SEM and HR-TEM analysis. The FT SERS spectra of 1, 4- BDT over these three substrates are presented in Figure 5.4.

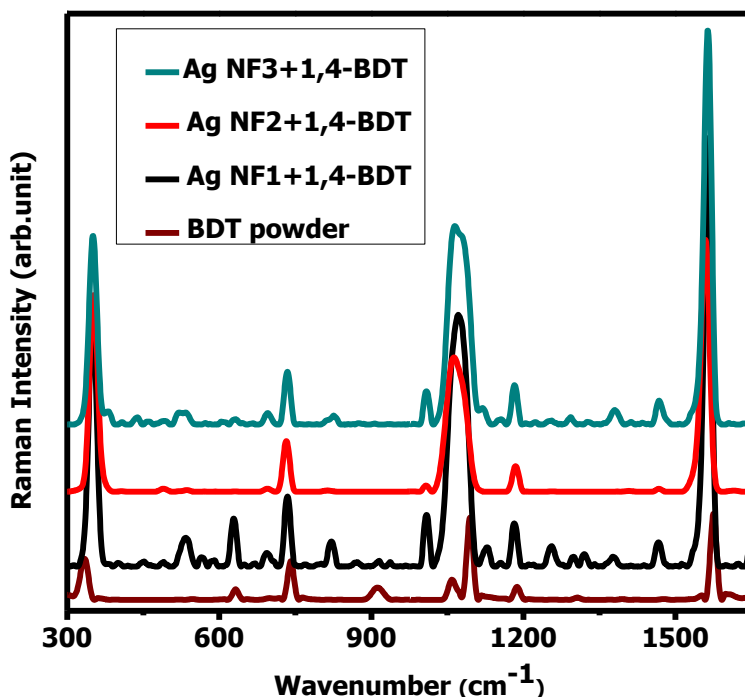


Figure 5.4. FT SERS spectra of 1, 4 -BDT obtained using the three Ag NF SERS substrates in the region between 300-1650 cm^{-1} . Ordinary powder FT Raman spectrum is also given.

It is generally observed that there are only minor differences observed between the different SERS spectra. However, minor differences do exist. The peaks corresponding to the ring stretching mode of 1, 4-BDT over Ag NF1 and Ag NF3 shows similar nature, while that for Ag NF2 is slightly different. For the sake of clarity of discussion, an expanded image is presented in Figure 5.5. As discussed earlier, the peaks are sharper and more intense in the case of Ag NF1 and NF3, plausibly due to enhanced local electric fields arising from sharper tips. Another important observation from Figure 5.5 is the slight red-shift of the ring C-C-C stretching modes for the SERS spectra from Ag NF2 as compared

to NF1 and NF3. It is also noteworthy that the peaks corresponding to the ring stretching modes for all these samples are red-shifted with reference to that for the powder spectrum. This can be explained based on fundamental spectroscopic equation relating frequency, force constant and reduced mass, viz., $\nu = \frac{1}{2\pi} \sqrt{\frac{k}{\mu}}$, where k is the force constant and ν is the vibrational frequency corresponding to that mode. A lower value for k is due to a reduced bond order in the ring and reduced electron density. This suggests that there is a stronger interaction between the benzene ring and the surface in the case of Ag NF2 with the blunt surface. The reduced intensity for the peak in the spectrum from AgNF2 also may be due to the lower electric field enhancement from the blunt surface of AgNF2.

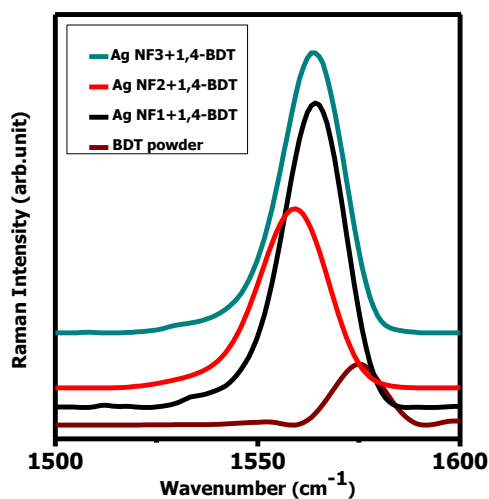


Figure 5.5. C-C-C ring stretching mode of 1,4-BDT powder and SERS spectra of BDT over Ag NF1, Ag NF2, Ag NF3 structures.

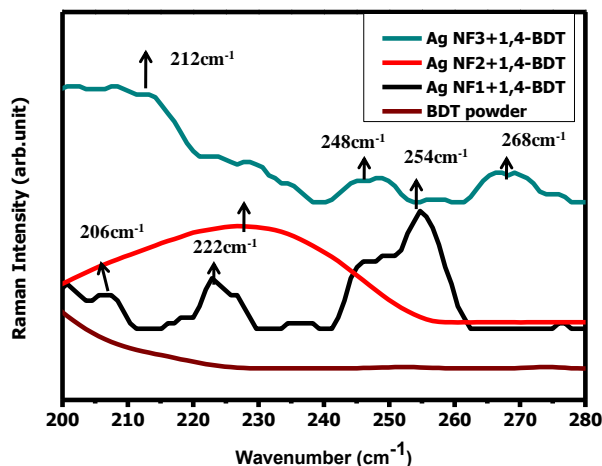


Figure 5.6. 200 - 280 cm^{-1} region of the FT SERS spectra of 1, 4-BDT over Ag NF1, Ag NF2, Ag NF3. Corresponding spectrum for the powder sample is also given.

This is also reflected in the low frequency Ag-S binding region of the spectra, below 300 cm^{-1} . For Ag NF1 and Ag NF 3 multiple peaks are obtained for the Ag-S binding, whereas only a single broad peak is present in the case of Ag NF2.

5.3.2.2. FT SERS of MB over Ag NF1, NF2, and NF3

Table 5.3 shows important vibrational modes and peak positions of both MB powder and spectral bands present in the SERS spectra of 10^{-4} M solution of MB over Ag NF substrates. Like that of BDT, most of the strong signals were obtained in the case of Ag NF1 and Ag NF3. A strong band at 243 cm^{-1} corresponding to Ag-N stretching is found to be most intense peak arising from Ag NF1 substrate that suggest chemical adsorption of MB molecules over Ag NF structures. Comparing SERS spectra resulting from all three substrates, the second most intense peak arises as a result of aromatic C-C-C stretching at 1620 cm^{-1} that suggest

MB molecules are normal to the surface. In the range 300-1000 cm^{-1} , three intense peaks appeared at 451 cm^{-1} , 680 cm^{-1} and 871 cm^{-1} corresponding to in plane (CNC) AMG bending, mixed vibrations of CH_3 rocking and out of plane CH bending and ring C-C-C stretching. At 1450 cm^{-1} peak due to asymmetric CN stretching appeared. These are shown in Figure 5.6. A strong single peak due to ring C-C-C stretching appeared at 1620 cm^{-1} in the region 1500- 1700 cm^{-1} .

Table 5.3. Peak positions corresponding to characteristic bond vibrations of ordinary Raman spectra of Methylene blue powder and SERS spectra of 10^{-4} M solutions of the same over four Ag NF substrates. (a) Ag -N stretching (b) C-N-C skeletal deformation (c) out of plane C-H bending (d) ring C-C-C stretching (e) out of plane C-H bending (f) out of plane C-H bending (g) C-N stretching (h) asymmetric C-N stretching (i) ring C-C-C stretching vibrations.

Sample	Peak positions corresponding to vibrations (cm^{-1})								
	a	b	c	d	e	f	g	h	I
MB powder		448	686	884	1067	1188	1386	1450	1617
Ag NF1+MB	243	451	681	872	1075	1182	1395	1461	1618
Ag NF2+MB	245	445	678	872	1073	1182	1401	1456	1618
Ag NF3+MB	243	451	672	878	1070	1182	1386	1474	1620

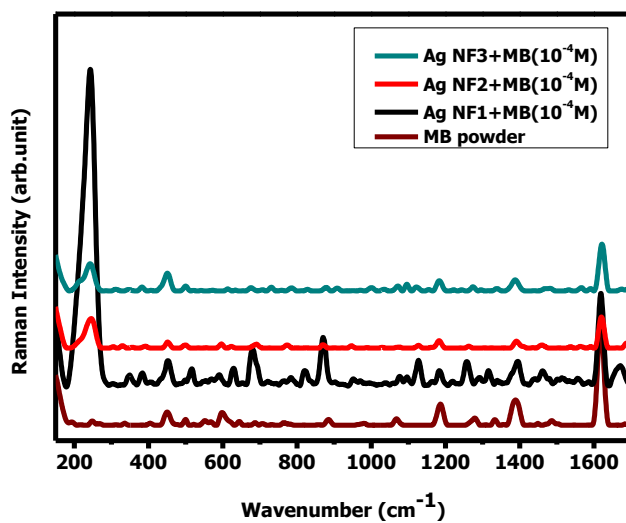


Figure 5.7. SERS spectra of 10^{-4} M solution of MB over Ag NF1-3 SERS substrates. Ordinary Raman spectra of MB powder is also given for reference.

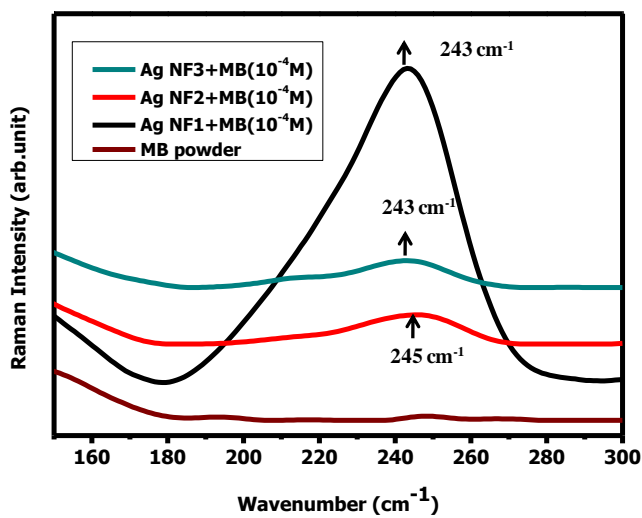


Figure 5.8. Region between 150 cm^{-1} and 300 cm^{-1} . SERS spectra showing Ag-N bonds.

5.3.2.3. Rhodamine 6B

R6B dye is an adulterant widely used in chilli powders and SERS can be used as a powerful tool for its detection.²³⁵ SERS studies as shown in Figure 5.9. suggest that SERS spectra from Ag NF1 and Ag NF3 are sharper as compared to that from Ag NF2 substrate also. However, the SERS spectral intensity from NF2 substrate is also quite significant. Compared to 1, 4-BDT and Methylene Blue, R6B is a larger and more complex molecule. Here also chemical bond formation of R6B over Ag NF substrate can be seen by the presence of strong band in the region below 300 cm^{-1} as shown in Figure 5.10. For Ag NF1, Ag NF2 and Ag NF3 this metal adsorbate bond formation is strong. Additionally, in all SERS spectra, band corresponding to carbonyl stretching (C=O) of carboxylic group can be seen at 1647 cm^{-1} , which further confirms the presence of free COOH group, i.e., binding through COO⁻ ion can be eliminated. Strong enhancement was found from Ag NF1 substrate. Here the most intense peak is the peak at 238 cm^{-1} corresponding to Ag–N bond stretching. Second most intense peak is at 1512 cm^{-1} , which is assigned as AMG rocking+ $\nu(\text{C-N}) + \nu(\text{COOH})$ vibrations. In the range 300-1000, a relatively intense peak appeared at 621 cm^{-1} and this corresponds to mainly xanthene ring puckering. There are three major peaks in the range 1000-1500 cm^{-1} , present at 1210, 1282, and 1386 due to C-O-C bridge band stretching, C-H bend, aromatic C-C bending. In the range 1500-1700 cm^{-1} , two more peaks appeared at 1593 and 1647 cm^{-1} (in addition to the peak at 1512), corresponding to the aromatic C-H bending and the aromatic C-C bending and the C=O stretching. Here, most of the Xanthene ring vibrations are enhanced significantly and vibration corresponding to benzoic acid ring is found to be weak, suggesting that benzoic acid ring is away from the surface

and that the Xanthene rings are normal to the surface. Peak positions corresponding to each spectral vibration is shown in Table 5.4.

Table 5.4. Peak positions corresponding to characteristic bond vibrations of ordinary Raman spectra of Rhodamine 6B powder and SERS spectra of 10^{-4} M solutions of the same over three Ag NF substrates: (a) Ag-N stretching (b) Xanthene ring puckering+ COOH attached ring out of plane bending vibration (c) C-O-C bridge band stretching +C-H wagging (d) C-H bending+ ring ν_{asym} (C-C-C) (e) ring breathing + ν (C-N) (f) AMG rocking+ ν (C-N) + ν (COOH)+aromatic C-H bending (g) Ring ν_{sym} (C-C-C)+CH₃ rocking (h) Ring ν_{asym} (C-C-C)+ring with COOH stretching+ ν (C-N).

Sample	Peak positions corresponding to vibrations (cm^{-1})							
	a	b	c	d	e	f	g	h
R6B powder		620	1193	1283	1361	1508	1593	1643
Ag NF1	238	620	1197	1279	1356	1512	1593	1647
Ag NF2	243	620	1197	1279	1356	1512	1593	1647
Ag NF3	228	620	1197	1279	1356	1508	1593	1647

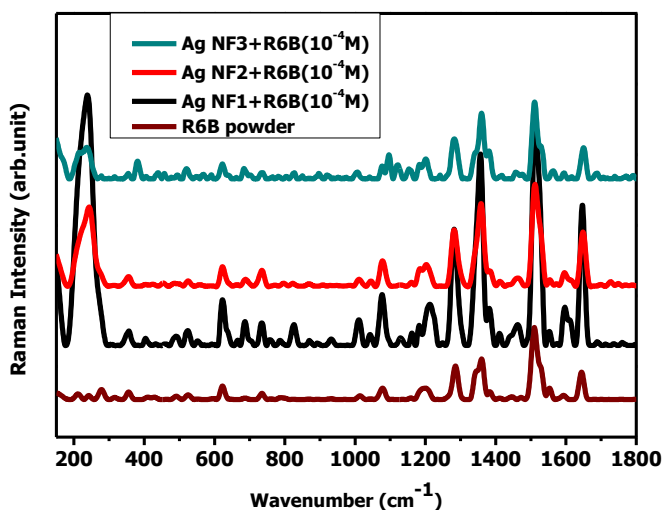


Figure 5.9: SERS spectra of 10^{-4} M solution of R6B over the three Ag NF1-3 substrates. Ordinary Raman spectra of R6B powder is also shown.

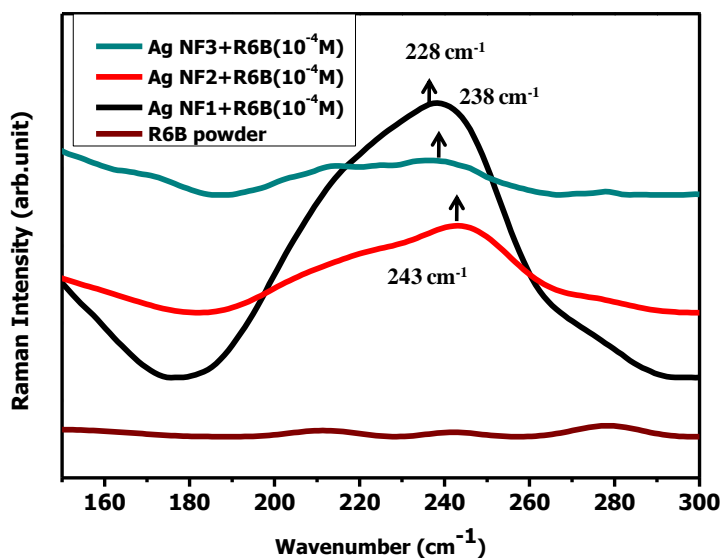


Figure 5.10. Region between 150 cm^{-1} and 300 cm^{-1} . SERS spectra showing presence of Ag-N bonds.

5. 4. Conclusions

Dependence of SERS spectra on the surface morphology/ shape anisotropy is investigated in this Chapter. Generally, we do expect that enhanced surface roughness would yield to enhanced local electric field and consequent enhancement in the SERS. Ag NF structures of different morphologies were prepared for investigating the spectral differences. It is interesting to note that LSPR is nearly absent in these substrates as a result of particle networking and interplasmonic coupling of the individual nanostructures. One can observe the metallic bond formation in the individual AgNPs. Thus, electric field enhancement must be resulting from the hot spots on the rough AgNF surface. Generally, we observe that there are no major differences in the spectra obtained, except the relative enhancement of the spectra for different substrates.

The intensities of the SERS spectra from AgNF1 and NF3 were observed to be higher from the “meat ball”-like AgNF2, due to a lesser degree of enhancement in the local electric field at the adsorbate surface. Another interesting observation is the observation of multiple peaks for the rough AgNF, possibly due to the dangling bonds at the rough nanometallic surface. Interestingly, we also observed a stronger interaction between the metallic surface and the π -electron system of the benzene ring of BDT and the rather flat NF2 surface as evidenced from the small red-shift of the mode corresponding to the ring C-C-C stretch.

CHAPTER 6

Dependence of SERS spectra of 1,4-BDT, MB, and R6B on the Shape/Morphology of Au NP substrates

6.1. Introduction

In Chapter 5, we discussed the SERS spectra of model molecular systems adsorbed on Ag NFs of different degree of surface roughness prepared by specifically tailored NF systems. It was demonstrated that the major differences were due to the difference in the local electric fields experienced by the molecule and consequent differences in SERS enhancements. For many of the applications, Au has more significant role in analytical chemistry particularly due to the biocompatibility and stability of the AuNPs from surface oxidation. Several synthetic strategies were adopted for the synthesis of Au NPs, such as those by Turkevich,²³⁶ Brust,²³⁷ Perrault,²³⁸ and Raveendran.²³⁹ It was demonstrated that by appropriate control of the reagents and the kinetics of both formation and growth, it is possible to synthesis Au NP systems having different morphologies such as Au nanospheres, nanorods, nanostars, nanocubes, nanoflowers, nanotriangles etc. Additionally, since Au NP is an excellent plasmonic material with specific LSPR absorptions in the visible range, shape dependent tuning of such LSPR absorptions too have gathered attention.²⁴⁰ In a broader sense, Au NPs with an extended plasmonic absorption in the Near Infrared region is highly beneficial for biomedical applications such as cancer diagnosis

and cancer treatments.²⁴¹ It is possible to functionalize them with polymers, surfactants, ligands, dendrimers, drugs, DNA, RNA, proteins, peptides and oligonucleotides, providing biomedical and bioanalytical applications with the least cytotoxic effects.

Seed mediated growth method has inspired the synthesis of many anisotropic AuNP systems and it was demonstrated that these systems hold much potential applications in areas of SERS and catalysis.²⁴² Gold nanoplates with specific shapes such as stars, pentagons, squares/rectangles, hexagons and truncated triangles falls under 2D anisotropic Au nanostructures. Usually, polymer templates such as PEO₂₀ PPO₇₀ PEO₂₀ (PEO=Poly (ethylene oxide), PPO = Poly (propylene oxide) were used as both reductant and stabilizer for gold nanosheet preparation.²⁴³ *In situ* thermal treatment in PVA matrix is also used for the preparation of polygonal gold nanoplates.²⁴⁴ For the synthesis of hexagonal single-crystalline Au nanoplates with preferential growth reduction by ortho-phenylene diamine in aqueous medium is employed.²⁴⁵ In another report Huang and co-workers synthesized triangular and hexagonal gold nanoplates in aqueous by thermal reduction of HAuCl₄ with tri sodium citrate in the presence of CTAB surfactant.²⁴⁶

Gold nanostructures hold excellent promise as SERS substrates. As observed in the previous chapters, it is likely that surface morphology and structure of the AuNP systems will have a significant role in governing their SERS activity. In this Chapter, we discuss the SERS of model molecular systems adsorbed on Au NP systems of different structure and morphology.

6.2. Experimental details

The general synthetic strategy was based on the earlier experimental procedures with slight modifications. Specific synthetic strategies are outlined below.

6.2.1. Synthesis of Au/C hybrid NFs

For Au/C hybrid NF synthesis, HAuCl_4 is reduced to Au/C hybrid NF using glucose as the reducing agent and a highly alkaline solution of sodium hydroxide. Au/C hybrid NF formation is facilitated by microwave irradiation. For this 40 ml 0.01M glucose, 20ml 1M NaOH and 200 μl 0.05M HAuCl_4 were used.

6.2.2. Synthesis of Au NFs

For Au NF synthesis, reduction of HAuCl_4 was carried out using ascorbic acid that found application in anisotropic NP synthesis due to its weak reducing capacity. 0.05M Ascorbic acid solution 40 ml, 200 μl 0.05M HAuCl_4 were subjected to microwave irradiation for Au NF synthesis.

6.2.3. Polygonal Au NPs

Here glucose is acting as the reducing agent and poly vinyl pyrrolidone (PVP) is functioning as capping agent. 200 μl of HAuCl_4 solution 0.05M, 40ml 0.05M glucose and 20ml 0.01M PVP solutions were heated using microwave energy for the formation of polygon shaped Au NP synthesis.

6.2.4. Preparation of SERS substrates

The SERS substrates were fabricated by depositing NP over Whatman 41 filter papers and drying in an oven at 60 °C.

6.3. Results and discussions

6.3.1. UV-Visible Absorption spectral studies

Photographic images of different shaped colloidal Au NP are shown in Figure 6.1 (1) and the corresponding SERS substrates are shown in Figure 6.1 (2). All the three Au based SERS substrates has shown an absorption in the visible region that extending to NIR region. DRS of the films are shown in Figure 6.1(3).

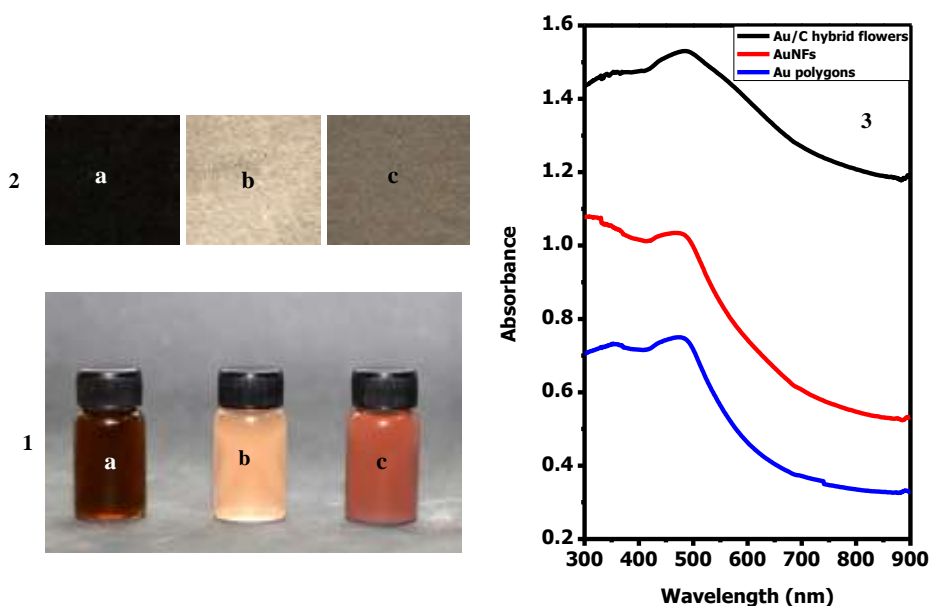


Figure 6.1.(1) [a-c] photographic images of Au/C hybrid flowers, Au NFs and Au hexagon nanoparticle sol (2) [a-c] photographic image of SERS substrates prepared from nanoparticle sol [a-c]. (3) DRS of the above NP films in the range 300-900 nm.

6.3.2. Morphological studies

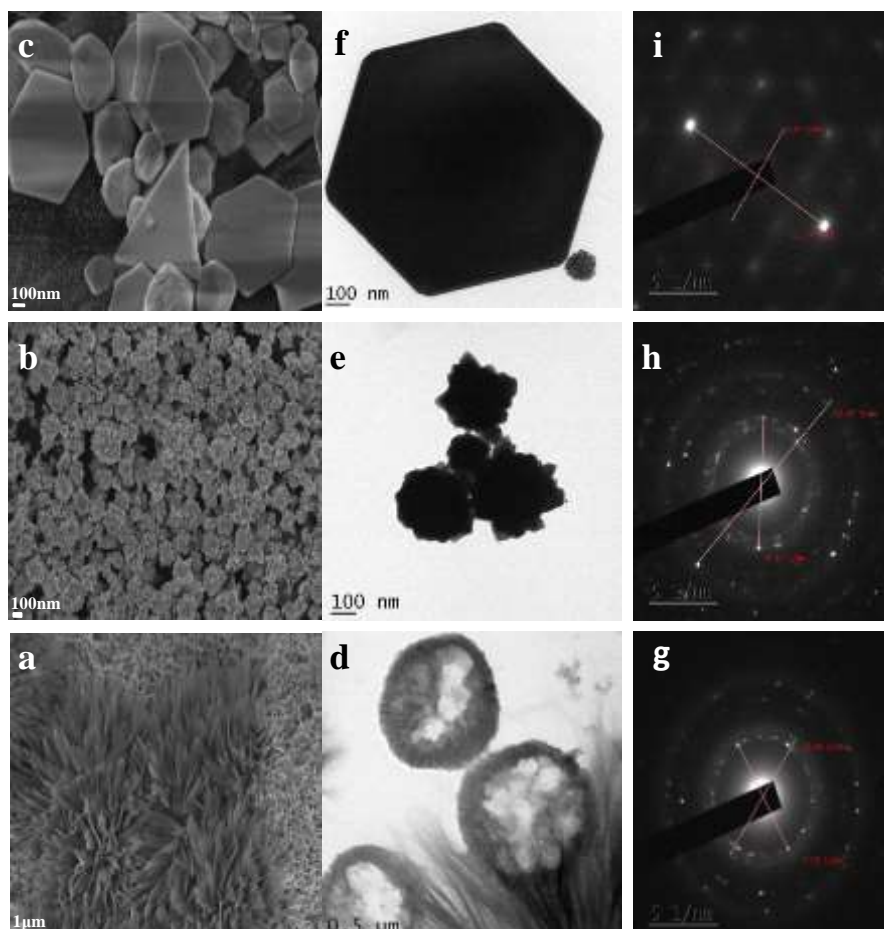


Figure 6.2: (a) – (c) High resolution FESEM images of the NPs corresponding to Figure 6.1. 1. (a)-(c); (d)–(f): High resolution TEM images and corresponding to (a)- (c); (g) – (i): SAED patterns corresponding to samples (a) – (c).

The FE-SEM images corresponding to the dispersions shown in Figure 6.1.1 (a) –(c) are presented in Figure 6.2. The SEM images clearly show three morphologically different species. The first one is a nanoflower like structure with lean fibers of Au, the second is a nanoflower structure

similar to the ones we observed for the silver nanoflowers shown in Chapter 5 and the third shows large faceted polygons. The same is also confirmed by the TEM presented in Figure 2, (d)-(f). The SAED patterns reveal the presence of Au/C hybrid nanostructure for the third sample. This is also supported by the TEM images in Figure 6.2. (d).

6.3.3. XRD studies

Crystallinity of prepared Au NPs were further characterized by XRD. From figure 5.3, XRD shows mainly (111), (200), (220) and (311) peaks in which (111) peak is the strongest one. These peaks correspond to FCC crystal structure of Au NP.

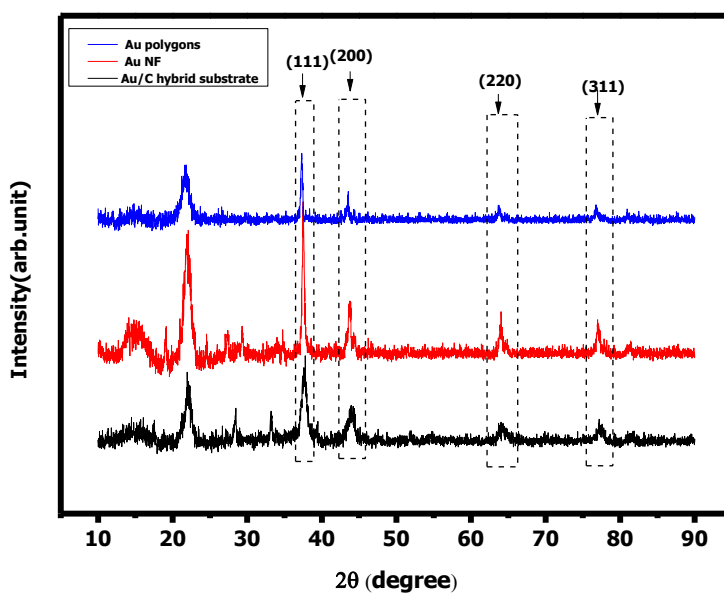


Figure 6.3. XRD patterns corresponding to the different samples: Au/C hybrid flowers; Au NFs, Au polygons.

6.3.4. SERS Studies

6.3.4.1. 1, 4- BDT

The focus of the investigations here is the difference in the SERS response to the difference in the structural and morphological differences of the different Au NP substrate systems studied. The FT-SERS spectra of 1, 4-BDT on Au/C hybrid flowers, Au NFs and Au polygon-based SERS substrates are presented in Figure 6.4. Normal powder FT Raman spectra of the sample is also shown for reference.

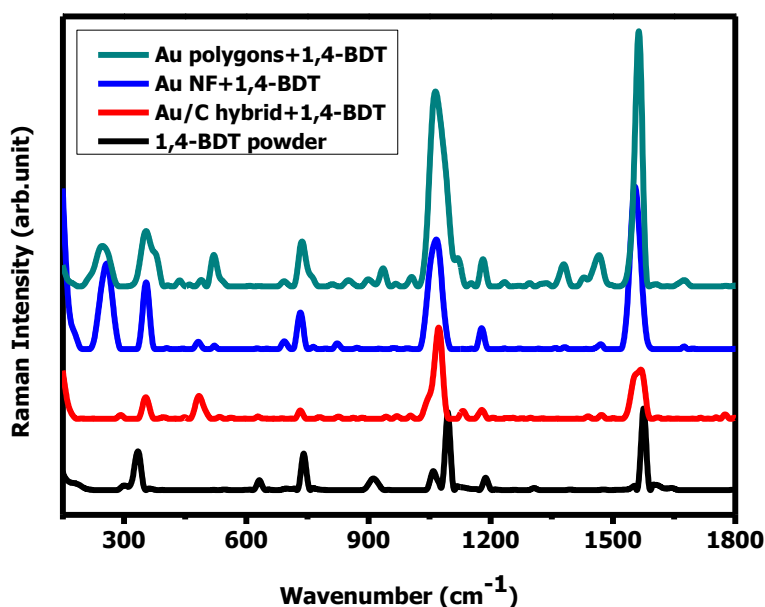


Figure 6.4. FT-SERS spectra of 1, 4-BDT on Au/C hybrid flowers, Au NFs and Au polygon based SERS substrates. Normal powder FT Raman spectra of the sample is also shown for reference.

It is observed that, in addition to the changes in the overall intensities of the spectra, the relative intensities of the individual peaks of FT-SERS

spectra of 1, 4-BDT has shown significant differences. It may also be noted here that we didn't observe any such significant differences between the spectra corresponding to different Ag NF systems in Chapter 5. Thus, these observations acquire significance.

Here when we look at the nature of peaks, peaks are much broadened, especially in the case of the ring breathing mode, plausibly due to faster relaxation at the surface. One observes a reversal in relative intensities of the peaks corresponding to the ring C-C-C stretching and the ring breathing vibration, respectively, of the 1,4-BDT molecule on the Au/C hybrid flower substrate that indicate a tilted or parallel orientation of the molecule. The higher intensity for the ring C-C-C stretching for the polygonal substrate plausibly indicate the angle of inclination of the molecule with respect to the surface is possibly more than that for the flower. We also observe small shifts in the ring C-C-C stretching frequencies indicating a small difference in the binding of the ring with reference to the surface and the modifications in the electron densities therefrom. Additionally, we observe a reduction in the intensity of peak at 350 cm^{-1} and an increase in intensity of peak at 483 cm^{-1} that resulting from the out-of-plane bending vibration of benzene ring. From the reduction in intensity of in-phase C-S bending and the ring C-C-C stretching, one may infer that there is no direct formation of Au-S bond. C-S stretching vibration at 535 cm^{-1} is strong in the case of Au polygons. The peak positions of ordinary Raman spectra of 1,4- BDT and SERS spectra arising from various substrates are shown in table 6.1

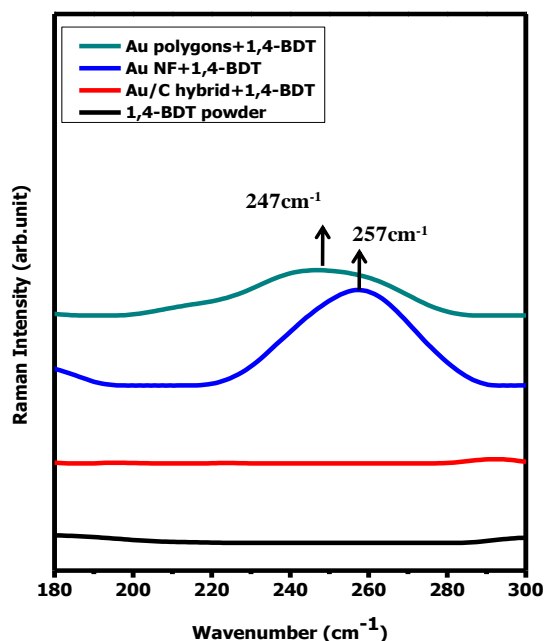


Figure 6.5. Metal-adsorbate region of the SERS spectra of 1,4-BDT on the three substrates (180-300 cm^{-1}). The powder spectrum is also provided for reference.

Table 6.1. Peak positions corresponding to characteristic bond vibrations of 1, 4-BDT in ordinary Raman and Surface Enhanced Raman. (a) in-plane C-S bending (b) ring out of plane bending (c) C-S stretching (d) in-plane ring bending (e) ring breathing (f) C-S-H bending (g) C-H wagging and ring in plane bending (f) ring stretching (g) ring C-C-C stretching

Sample	Peak positions corresponding to vibrations (cm^{-1})								
	a	b	c	d	e	f	g	h	i
BDT powder	334	Nil	Nil	631	740	914	1058,1094	1187	1574
Au polygons	354		535	-	735	Nil	1064	1179	1564
Au NF	354			631	731	Nil	1067	1176	1554
Au/C hybrid flowers	350	483		631	731	Nil	1070	1176	1567

The low frequency region of the FT-SERS spectra of the molecule on the three different substrates is presented in Figure 6.5.

It can be observed that the metal-adsorbate bonding is stronger in the case of the Au NF substrate in comparison with the faceted polygonal substrates. In fact, one observes the Au-S stretch at 257 cm^{-1} for the Au-NF system while the same frequency is at a lower value at 247 cm^{-1} for the polygonal substrate. Notably, the band corresponding to the Ag-S bond is nearly absent in the case of the Au/C hybrid substrate. This may also be correlated with the frequency shift, though small, of the ring C-C-C stretching. For clarity, this region of the spectra alone is reproduced in Figure 6.6.

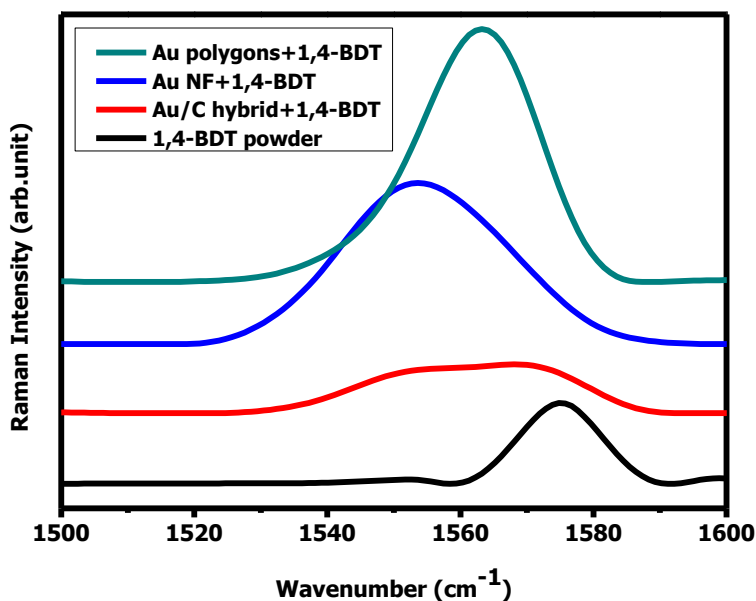


Figure 6.6. Spectral region corresponding to ring C-C-C stretching vibration of the SERS spectra of 1, 4-BDT on Au/C hybrid flowers, Au NFs and Au polygon-based SERS substrates. Powder Raman spectrum is also presented for reference.

It is observed that the peak corresponding to the ring C-C-C mode occurs at 1550 cm^{-1} for the AuNF substrate whereas the same peak appears around 1562 cm^{-1} in the case of the polygonal Au substrate. These observations may plausibly be explained by an increased flow of electron from the π -electron network of the thiol to the AuNF substrate via the Au-S bond, making the latter strong. This also explains the lower frequency of the ring C-C-C stretch for the NF adsorption in comparison with the polygonal structure. Interestingly, the SERS spectrum from the Au/C hybrid substrate show two peaks one around 1550 cm^{-1} and another around 1560 cm^{-1} , indicating two different modes of interaction. It may also be recalled that the peak corresponding to the Au-S mode is absent in the SERS from the Au/C hybrid substrate. The results clearly indicate how the SERS can in fact be dependent on the substrate surface structure and bonding.

6.3.4.2. SERS of Methylene Blue (MB)

At this point, it is also pertinent to investigate the SERS spectra of MB on these three substrate systems and the same is presented in Figure 6.7.

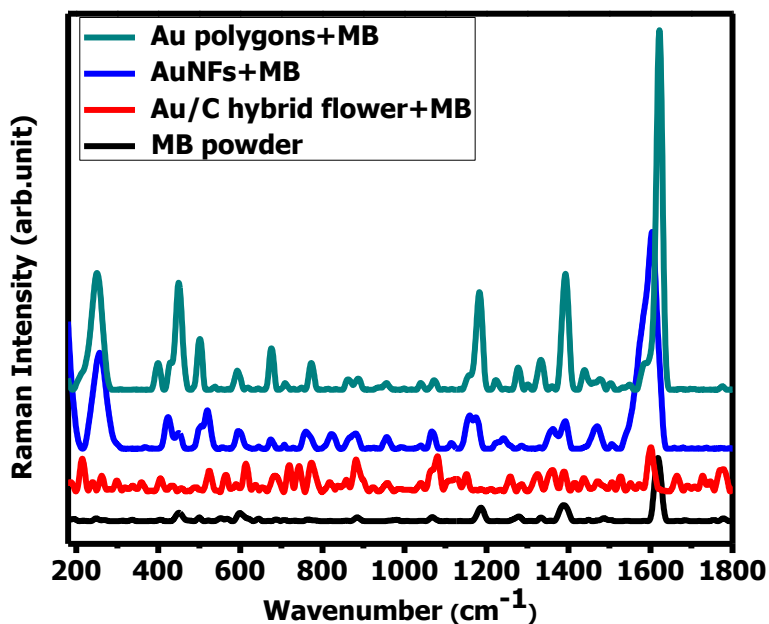


Figure 6.7. SERS spectra of MB on Au/C hybrid flowers, Au NFs and the Au polygon-based SERS substrates. The FT-Raman spectra of the powder sample is also presented for reference.

In fact, one observes significant differences between the SERS spectra for the MB sample recorded from the three substrate systems. Generally, the SERS spectrum from the Au/C hybrid system is much less intense in comparison with the other two spectra. Of all the three different Au substrates, the polygon shaped NP substrate gives the most intense and well-defined SERS peaks. The low frequency region of the SERS spectra of MB from the different substrates is given in Figure 6.8.

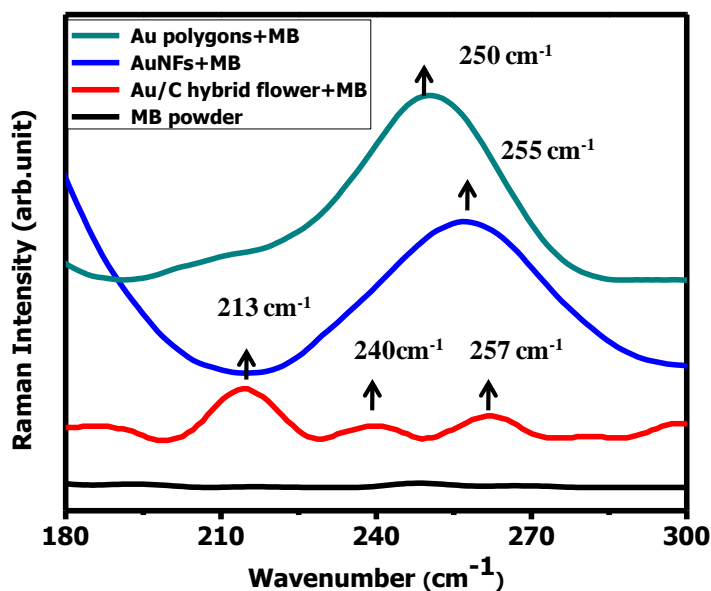


Figure 6.8. Ordinary Raman spectra and SERS spectra of MB on Au/C hybrid flowers, Au NFs and Au polygon based SERS substrates in the region 180-300 cm^{-1} showing the presence of Au-S bond in SERS spectra.

Almost all peaks in the powder spectra get enhanced for both Au polygons and Au NF SERS substrates which can be explained on the basis of strong adsorption of MB over these substrates through metal-adsorbate bond formation. For the polygon Au NP substrate, the Au-S mode is present at 250 cm^{-1} while that for the Au NF, it is at 257 cm^{-1} . For the Au/C hybrid substrate, three relatively less intense peaks are present at 213 cm^{-1} , 240 cm^{-1} and 257 cm^{-1} . This reveals strong binding of the molecule with the Au surface through the sulphur atom, although the strength of binding is different for the three systems; the strongest being for the NF system. Multiple binding modes are possible in the case of the Au/C hybrid substrate as evidenced by the multiple peaks. The overall SERS spectral profiles resulting from the Au polygons and Au

NF found to be nearly similar, although one observes small changes with reference to the relative intensities of some bands. For the region 300-1000 cm^{-1} , for polygon shaped Au substrate and Au NF, the intense peak at 449 cm^{-1} correspond to the $\delta(\text{CNC})_{\text{AMG}}$ mode. Other intense peaks were observed at 501, 593, 676, 772 cm^{-1} related to the $\alpha(\text{CNC})_{\text{AMG}}$ and $\delta(\text{C-S-C})$, $\gamma(\text{CH})$ and $\nu(\text{CS})_{\text{ring}}$, $\nu(\text{CN})_{\text{AMG}}$, and βCH . In the region 1000-1500 cm^{-1} , the peak corresponding to $\nu(\text{CN})_{\text{ring}}$ at 1392 cm^{-1} is the most intense. Another intense peak is observed at 1183 cm^{-1} due to methyl group rocking and CH out of plane bending. In the region 1500-1800 cm^{-1} , for the Au polygon substrate, a strong peak is present at 1621 cm^{-1} corresponding to skeletal vibrations of both ring CCC and ring CN. But this peak for the Au NF- and the Au/C hybrid substrates this peak occurs around 1601 cm^{-1} . The individual peak positions for the various substrates are presented in Table 6.2.

Table 6.2. Peak positions corresponding to characteristic bond vibrations of ordinary Raman spectra of Methylene blue powder and SERS spectra of 10^{-4} M solutions of the same over four Ag NF substrates. (a) Au-S stretching (b) C-N-C skeletal deformation, δ C-S-C, ring deformation (c) C-N-C skeletal deformation (d) δ C-S-C (e) ring C-C-C stretching (f) out of plane C-H bending (g) out of plane C-H bending (h) in-plane C-H bending (i) C-N stretching (h) asymmetric C-N stretching (i) ring C-C-C stretching vibrations.

Sample	Peak positions corresponding to vibrations (cm^{-1})											
	a	b	c	d	d	e	f	g	h	i	j	k
MB powder		448	499			686	884	1067	1188	1386	1450	1617
Au polygons+MB	250	449	502	593	Nil	676	863, 887	1073	1181	1391	1475	1621
Au NF+MB	255	423, 449	500, 520	595	Nil	674	878	1066	1157, 1176	1390	1467	1602
Au/C hybrid flowers+MB	213, 240, 257	Nil		Nil	614	682	882	1080	Nil	1390	1470	1600

The spectral region corresponding to the ring C-C-C stretch region is presented in Figure 6.9. One observes that the peak corresponding to the ring C-C-C stretch is at a considerably higher wavenumber for the polygonal substrate in comparison with that for the Au/C hybrid substrate. As mentioned, this indicates that electron density in the ring is higher in the case of the polygonal Au substrate and lower in the other two cases, indicating a difference in the strength of interaction with the surfaces. As discussed earlier, this is also evident from the Au-S interaction strengths. Also, the line width of the spectrum from the polygonal substrate is sharper than the other two. This may be due to enhanced surface disorder in the case of the NF and Au/C hybrid systems and consequently faster relaxation of this vibrational mode.

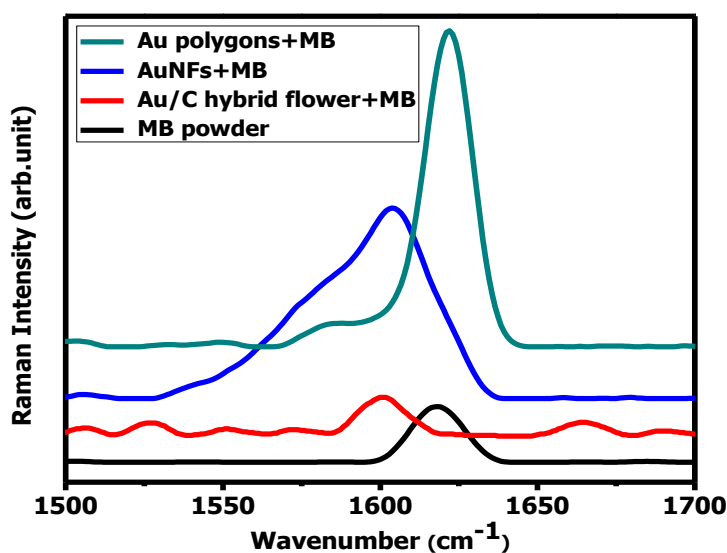


Figure 6.9. SERS spectra of MB on Au/C hybrid flowers, Au NFs and Au hexagon based SERS substrates in the region 1500-1800 cm⁻¹ showing red shift in the ring C-C-C vibration in SERS spectra. The FT Raman spectrum of the powder sample is also given.

6.3.4.3. Rhodamine 6B (R6B)

The FT-SERS spectra of R6B in the 200-1700 cm^{-1} region on the three substrate systems is presented in Figure 6.10.

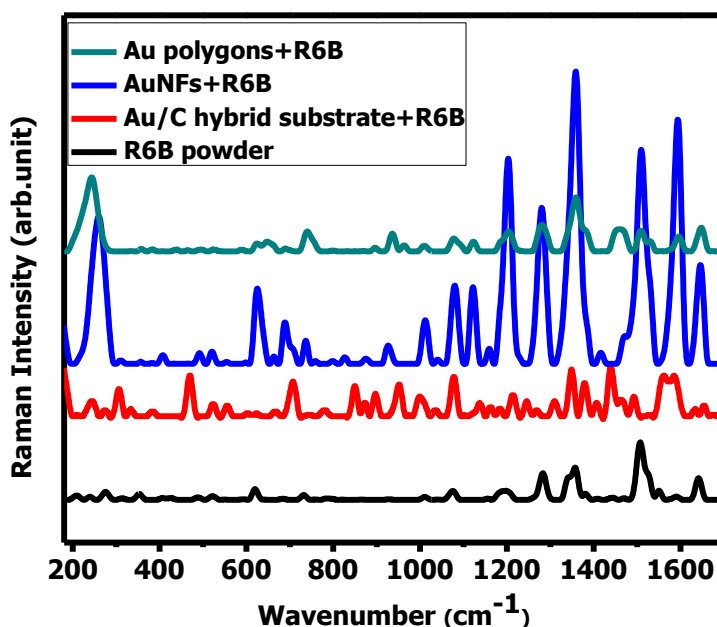


Figure 6.10. SERS spectra of R6B on Au/C hybrid flowers, Au NFs and Au hexagon based SERS substrates. Ordinary Powder FT Raman spectrum is also given for reference.

All the three substrates yield reasonably good SERS spectra, although the spectral intensity is more prominent for the polygonal Au NP system. In the region below 300 cm^{-1} , the modes corresponding to the metal-adsorbate bond formation are present, suggesting both chemical and electromagnetic contributions towards SERS enhancement. The low wavenumber regions of the spectra are presented separately in Figure 6.11. For Au polygon shaped NP based SERS substrate a strong peak is

present at 243 cm^{-1} , while that for Au NF substrate it is at 260 cm^{-1} . For the Au/C hybrid substrate, this region exhibits weak multiple peaks at 244 cm^{-1} and 274 cm^{-1} . The presence of Au-N bond suggests adsorption of R6B through Nitrogen. This is further supported by the presence of carbonyl stretching band at 1646 cm^{-1} arising from free carboxylic acid group.

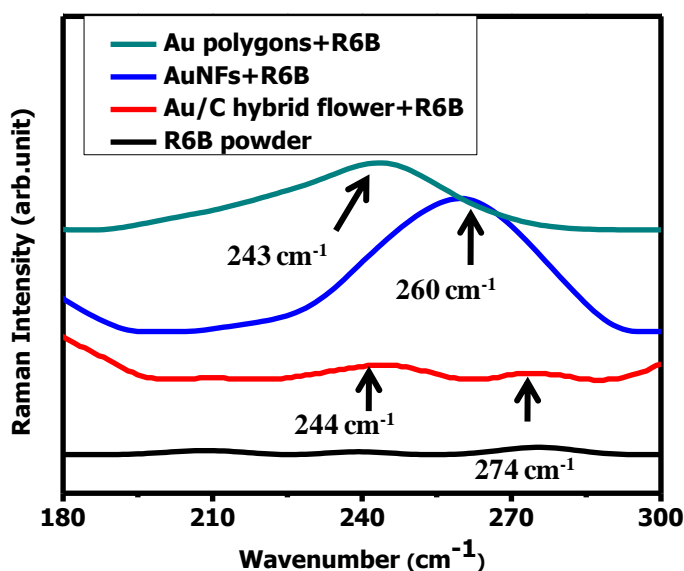


Figure 6.11. SERS spectra of R6B on the three SERS substrates, in the region $180\text{-}300\text{ cm}^{-1}$. Ordinary powder FT Raman of the sample is also presented for comparison.

A strong metal-adsorbate binding is missing in the case of Au/C hybrid flowers. This also leads to a very weak SERS spectrum in the case of the Au/C hybrid system. There are two peaks at 1633 and 1653 cm^{-1} , respectively, and the one at 1653 cm^{-1} may be resulting from the free carboxylic acid group attached to the benzene ring. While comparing the relative intensities of the peaks, the intensity of the benzoic acid ring is

much lower than that for the Xanthene ring, suggesting that the benzoic acid ring is farther from the Au surface. This can be well explained if the nitrogen of the xanthene ring is taking part in adsorption. Regarding the orientation of R6B, one may suggest that the R6B is normal to the surface in the case of Au NF substrate, while it is tilted or parallel to the surface of Au polygons and Au/C hybrid flowers. The peak at 624 cm^{-1} due to xanthene ring puckering is intense for the NF substrate and weak for the Au/C hybrid substrate peak. In the region $1000\text{-}1500\text{ cm}^{-1}$, six intense peaks are present that are located at 1011 cm^{-1} , 1079 cm^{-1} , 1120 cm^{-1} , 1202 cm^{-1} , 1280 cm^{-1} , 1358 cm^{-1} and these peaks are originating as a result of number of mixed vibrations such as (methyl group rocking + $\text{C}_x\text{-C}_x\text{-C}_x$ bending + $\text{C}_x\text{-H}$ wagging), (C-H wagging + ring in-plane bending), (C-H wagging + $\nu_{\text{sym}}(\text{C-O-C}) + \delta(\text{OH})$), (ring $\nu_{\text{asym}}\text{C-C-C} + \text{C-H}$ wagging + AMG rocking, C-H wagging + ring breathing + $\nu(\text{CN})$). Out of these, peak at 1358 cm^{-1} is the most intense one. In the region $1500\text{-}1800\text{ cm}^{-1}$, three intense peaks are present for Au NF based substrate, one at 1508 and the rest two at 1593 and 1645 cm^{-1} . These are assigned as vibrations due to (AMG rocking + ring deformation), (ring $\nu_{\text{sym}}\text{C-C-C} + \text{C-H}$ wagging), ring $\nu_{\text{sym}}\text{C-C-C}$. These peaks are relatively less intense in the case of the other two substrates. The assignments of the various peaks are presented in Table 6.3.

Table 6.3. Peak positions corresponding to characteristic bond vibrations of ordinary Raman spectra of Rhodamine 6B powder and SERS spectra of 10^{-4} M solutions of the same over three Au substrates. (a) Au-N stretching (b) Xanthene ring puckering+ COOH attached ring out of plane bending vibration (c) C-O-C bridge band stretching +C-H wagging (d) C-H bending+ ring ν_{assym} (C-C-C) (e) ring breathing + ν (C-N) (f) AMG rocking+ ν (C-N) + ν (COOH)+aromatic C-H bending (g) Ring ν_{sym} (C-C-C) +CH₃ rocking (h) Ring ν_{assym} (C-C-C) +ring with COOH stretching+ ν (C-N) + Carbonyl stretching

Sample	Peak positions corresponding to vibrations (cm ⁻¹)							
	a	b	c	d	e	f	g	h
R6B powder		620	1193	1283	1361	1508	1593	1643
Au polygons	243	625, 643	1204	1280	1355	1506	1597	1646
Au NF	260	625	1199	1280	1358	1506	1591	1646
Au/C hybrid flower	244, 274	Nil	1213	Nil	1347, 1380	1491	1558, 1585	1633, 1653

6.4. Conclusions

In this chapter, we present the SERS spectra of 1,4-BDT, MB and R6B are studied over three Au-based SERS substrate systems, viz., the faceted polygonal, NF, and Au/C hybrid substrates. All the three give good SERS spectra although the one obtained from the Au/C hybrid system is generally weak. We observe considerable differences in the SERS of these three compounds with reference to the different substrate systems. Specifically, one observes a difference in the mode and strength of binding of these molecules on the three substrates as evidenced by the position of the metal-adsorbate peaks. The metal-

adsorbate bonds are stronger in the case of the NF system in comparison with the polygonal systems. This must be attributed to the largely unsatisfied Au surfaces of the NFs, making the metal-adsorbate peaks stronger. This is also evidenced by the increased electron density in the π -ring systems in the case of the adsorbate molecules attached to the rather smooth polygonal systems. In comparison with Ag NF systems studied in Chapter 5, the observed differences between the different SERS substrate systems are more pronounced plausibly because of the fact that the differences between the substrate structures in the case of the AgNF systems are much lesser than those between the Au substrate systems investigated here.

CHAPTER 7

CONCLUSIONS AND OUTLOOK

Over the past two decades, metal and alloy nanoparticles have acquired significant importance in a wide range of applications in diverse areas such as optics, electronics, biology and medicine, and information technology, by virtue of the novel electronic properties that result from spatial confinement effects. Surface enhanced Raman spectroscopy (SERS) has been one such major advancement that helped the analytical chemist to surmount the challenge of overcoming the very poor Raman scattering cross-section that enabled the Raman spectroscopic detection and analysis of important molecular systems. When a molecule is adsorbed on the surface of a metal nanoparticle, the Raman spectral intensity corresponding to that molecule enhances by a factor of about 10^6 by virtue of two mechanisms, viz., the chemical enhancement and the electromagnetic enhancement. The former is directly related to the “bonding” of the molecule with the surface and the plausible electron transfer between the molecule and the surface. The latter, the electromagnetic enhancement, is generally related to the enhancement of the local electric field experienced by the molecule and depends on several factors such as the proximity of a specific functional group of the molecule with respect to the surface, its orientation with respect to the surface as well as the geometry of the measurement. For a metal or alloy nanoparticle, the localized surface plasmon resonance causes a resonant, collective oscillation of the surface electrons of the nanoparticle by absorbing light of characteristic wavelength that

matches the energy required for such an oscillation. It is also possible to tune the LSPR or the corresponding wavelength of the absorbed light by modifying the size of the particle, choice of the metal, and by the process of alloying of two or more metallic systems. Since the discovery of SERS, volumes of works have focused on understanding SERS more fundamentally and to explore how one can utilize SERS as an analytical tool more effectively. At the outset itself, it is important to mention SERS, not just an enhanced Raman spectroscopic technique, but a more versatile tool that provides several other properties such as the binding and orientation of the molecule. The work presented in this thesis is a humble attempt in this direction to complement some of the existing knowledge in this aspect. The thesis is divided into seven Chapters.

A general introduction to nanoscience and nano technology, metal nanoparticles especially Gold and Silver, Surface plasmons, various theories of optical properties of metal NP, fundamentals of Raman spectroscopy, SERS spectroscopy and its applications are outlined in the first Chapter. In chapter 2, we have provided a brief description of various analytical and instrumental techniques used for the analysis of nanostructured materials are discussed.

Chapter 3 deals with the wavelength dependent SERS studies of 1,4-BDT under three conditions-plasmon resonant, near resonant and off resonant conditions, with reference to the absorption maximum λ_{\max} of the using two excitation lines 532nm and 1064nm. The main objective of the work is to investigate the correlation between laser excitation and plasmon excitation on SERS spectra using Au, Ag, and AuAg alloy

nanoparticles of various composition in association with the two excitation lines. Flexible, cellulose acetate sheet was selected for incorporating metal and alloy NPs for the preparation of the SERS substrate. We also employed networked metal and alloy NPs, which do not have any specific absorption maximum, or that absorbs over the entire region of the visible region of the electromagnetic spectrum to investigate its effect on the SERS. SERS studies of 1,2-BDT and 1,3-BDT on plasmonic metal and alloy nanoparticles and their networked structures are carried out for the purpose. These studies show that differences are arising with respect to relative intensities and spectral profile. There appears to be several factors that doesn't allow a generalization in terms of a correlation between the position of laser excitation and plasmon excitation wavelength on SERS enhancement. It also indicated that the composition dependence of SERS substrates also have a significant influence on the SERS spectra.

In chapter 4, the possibility of preferential binding of different atoms of analyte molecules on Au, Ag, and AuAg alloy NPs was studied. For this, analyte molecules with multiple binding sites such as MB, and R6B molecules were selected and SERS studies were carried out using 1064 nm. Since absorption of both dyes are off resonant with excitation wavelength, problem of fluorescence can be avoided. Here we have taken cotton fabric as the base material for incorporating NPs. The SERS spectra exhibit significant changes and a detailed examination of these spectra reveal the formation of distinct metal- adsorbate bonds and the differences in the mode of binding of the molecule with reference to the

surface. In comparison with the calculated spectra, we could predict the orientation of these analyte molecules on different SERS substrates.

In chapter 5, we have carried out the SERS studies of 1,4-BDT, MB and R6B on Ag substrates with different shape/morphology. Ag NF structures of different morphologies were prepared for investigating the spectral differences. It is observed that we do not observe any specific absorption in the visible region, except for a general broad absorption, plausibly as a result of particle networking and interplasmonic coupling of the individual nanostructures, via metallic bond formation between the individual Ag NPs. Thus, electric field enhancement must be resulting from the hot spots on the rough Ag NF surface. The spectra obtained from these substrates did not exhibit major changes, except the difference in the relative enhancement of the spectra from the different substrates. The intensities of the SERS spectra from AgNF1 and NF3 were observed to be higher from the “meat ball”-like AgNF2, due to a lesser degree of enhancement in the local electric field at the adsorbate surface. Another interesting observation is the observation of multiple peaks for the rough Ag NF, possibly due to the dangling bonds at the rough nanometallic surface. Interestingly, we also observed a stronger interaction between the metallic surface and the π -electron system of the benzene ring of BDT and the rather flat NF2 surface as evidenced from the small red-shift of the mode corresponding to the ring C-C-C stretch. Shape-dependent studies on Ag were carried out by preparing three Ag NF substrates containing flowers with varying degrees of sharpness and we studied how this slight change in flower morphology going to affect SERS spectra. We were able to predict the orientation of these analytes

by detailed observation of SERS data and concentration of electric fields on sharp tips and protrusions contributing towards higher enhancement in SERS were also examined. We additionally prepared Au NP of three different morphologies and studied shape dependence on SERS using same model systems.

In Chapter 6, we have presented the SERS spectra of 1,4-BDT, MB and R6B studied over three Au-based SERS substrate systems, viz., the faceted polygonal, NF, and Au/C hybrid substrates. All the three give good SERS spectra although the one obtained from the Au/C hybrid system is generally weak. We observe considerable differences in the SERS of these three compounds with reference to the different substrate systems. Specifically, one observes a difference in the mode and strength of binding of these molecules on the three substrates as evidenced by the position of the metal-adsorbate peaks. The metal-adsorbate bonds are stronger in the case of the NF system in comparison with the polygonal systems. This must be attributed to the largely unsatisfied Au surfaces of the NFs, making the metal-adsorbate peaks stronger. This is also evidenced by the increased electron density in the π -ring systems in the case of the adsorbate molecules attached to the rather smooth polygonal systems. In comparison with Ag NF systems studied in Chapter 5, the observed differences between the different SERS substrate systems are more pronounced plausibly because of the fact that the differences between the substrate structures in the case of the AgNF systems are much lesser than those between the Au substrate systems investigated here.

The results presented in the above chapters clearly demonstrate that SERS cannot be considered as a routine Raman spectroscopic technique and care must be taken to analyze the SERS spectra. SERS spectra recorded from different substrates vary based on the shape of the individual nanoparticles, their shapes as well as the orientation of the molecule with respect to the surface. Since the molecular orientation depends on the mode of binding, the nature of the metal or alloy surface on which also affects the SERS spectra. We have also shown that the λ_{\max} value of the nanoparticle substrate and its relative positioning with reference to the excitation source can also affect the SERS spectra. In conclusion, it may be stated that each SERS spectrum may be unique in terms of these factors mentioned above and that SERS should be used as a detection tool for biomolecules, providing additional information regarding the binding and orientation of the molecules. Since some vibrational modes will be amplified and some may be suppressed based on these, care must be taken to interpret the spectra correctly.

REFERENCES

1. Liz-Marzan, L.M. *Langmuir*. **2006**, 22, 32-41.
2. Schwartzberg, A. M; Zhang, J. Z. *J. Phys. Chem. C*, **2008**, 112, 10324- 10337.
3. Henglem, A. *Chem. Rev.* **1989**, 89, 1861 – 1873.
4. Hartland, G.V. *Chem. Rev.* **2011**, 111, 3858 – 3887.
5. Noguez. C, *J. Phys. Chem. C*. **2007**, 111, 3806 – 3819.
6. Sau, T. K; Rogach, Ai; Jackel F; Klar, T. A; Feldmann, J. *Adv. Mater.* **2010**, 22, 1805 – 1825.
7. Xia, Y; Xiong, Y; Lim, B; Skrabalak, S. E. *Angew. Chem. Int. Eb.* **2009**, 48, 60-103.
8. Liz-Marzan, L. M. *Mater.Tobay.* **2004**, 7, 26 – 31.
9. Petryayeva, E; Krull, U. *J. Analytica Chimica Acta.* **2001**, 706, 8-24
10. Zackay, V. F; Parker, E. R; Morris Jr, J. W; Thomas, G. *Mater. Sci. and Eng.* **1974**, 16(3),201 -203.
11. Feynman, R. P. "There's Plenty of Room at the Bottom". In Gilbert, Horace D(ed). *Miniaturization. Reinhold.* **1961**, 282 – 296.

12. Taniguchi, N. On the basic concept of “Nano – Technology “, Proceedings of the International Conference on Production Engineering Tokyo Part II, Japan Society of Precision Engineering, Tokyo, **1974**, 5 – 10.
13. “The Nobel Prize in Physics **1986**, Perspectives –Life through a lens”
14. Von Ardenne, Manfred, “Das Elektronen- Rastermikroskop. Praktische Ausführung” Zeitschrift für Technische Physik, **1938**, *19*, 407-416.
15. Binnig, G. Scanning Tunneling Microscopy – from birth to adolescence, Nobel Lectures in Physics, 1981-1990, world scientific publishing.
16. Binnig, G; Quate, C. P; Gurber, C. Atomic Force Microscope, *Phys. Rev. Lett.* **1986**, *56*, 930.
17. Smalley, R. E, Discovering the fullerenes, Nobel Lectures in Chemistry.1996-2000, World Scientific Publications Co. Singapore, **2003**, 89.
18. Iijima, S, Helical Micro tubes of graphitic Carbon, *Nature*. **1991**, *354*,96.
19. Geim, A. K, “Graphene Pre History” *Physica Scripta*. **2012**,146.
20. Boehm, H. P; Clauss, A; Fisher, G. O; Hofmann, U, *Zeitschrift für Anorganische und Allgemeine Chemie*. **1962**, *316*, 3 – 4.

21. Liang Li; Takeshi Sasaki; Yoshiki Shimizu; Naoto Koshizaki, *J. Phys. Chem. C* **2009**, *113* (36), 15948-15954.
 22. Alexis Loiseau; Lu Zhang; David Hu; Michèle Salmain; Yacine Mazouzi; Raphaël Flack; Bo Liedberg; Souhir Boujday, *ACS Appl.Mater. Interfaces*. **2019**, *11* (50), 46462-46471
 23. Alec P. LaGrow; Kristian Rahbek Knudsen; Noktan M. AlYami; Dalaver H. Anjum; Osman M. Bakr, *Chem. Mater.* **2015**, *27* (11), 4134-4141
 24. Swihart, M. T., *Curr. Opin. Colloid Interface. Sci.* **2003**, *8*(1), 127 – 133.
 25. Amendola, V; Meneghetti, M. *Phys. Chem. Chem.Phys*, 2009, *11*, 3805- 3821.
 26. Solero, G. J., *Nanosci.Nanotechnol.* **2017**, *7*(1), 21- 25.
 27. Kermantur, A; Rizi, B. N; Vaghyenegar, M; Yazdabadi, H. G. *Mater.***2009**, *63*(5), 575- 577.
 28. Torimoto, T; Okazaki, K-I; Kiyama, T. *Appl. Phys. Lett*, **2006**, *89*, 243117
 29. Munoz, J. E; Cervantes, J; Esparza, R; Rosas, G. J. *Nanopart. Res.* **2007**, *9*, 945 – 950
 30. Marques- Hueso, J; Morton, J. A. F; Wang, X; Bertram – Seira, E; Desmulliez, M. P. Y. *Nano technology*, **2019**, *30*, 015302.
-

31. Chem, D-H; He, X-R., *Mater. Res.* **2001**, 36, 1369 – 1377.
 32. Petcharoem, K; Sirivat, A., *MATSCIENGB- ADV.* **2012**, 177(5), 421-427.
 33. Han, S; Kong, M; Guo, Y; Wang, M., *Mater.***2009**, 63(13-14), 1092-1094.
 34. Prathna, T. C; Chandrasekaran, N; Raichur, A. M; Mukherjee, A., *Colloids Surf B Biointerfaces.* **2011**, 82, 152-159.
 35. Malik, M. A; Wani, M. Y; Hashim, M. A. *Arab.J.Chem.* **2012**, 5(4), 397-417.
 36. Xu, H; Zeiger, B. W; Suslick, K. S. *Chem.Soc.Rev.* **2013**, 42, 2555-2567.
 37. Roberto A. Martínez-Rodríguez; Francisco J. Vidal-Iglesias; José Solla-Gullón; Carlos R. Cabrera; Juan M. Feliu, *J. Am. Chem. Soc.* **2014**, 136 (4), 1280-1283.
 38. Partha Pratim Goswami; Hanif A. Choudhury; Sankar Chakma; Vijayanand S. Moholkar, *Ind. Eng. Chem. Res* **2013** 52 (50), 17848-17855
 39. Turkevich, J; Stevenson, P.C; Hillier, J. *Discuss. Faraday. Soc.* **1951**, 11, 55-75.
 40. Frens, G., *Colloid Polym Sci.* **1972**, 250(7),736-741.
-

41. Brust, M; Walker, M; Bethell, D; Schiffrin, D.J; Whyman, R., *Chem. Commun.* **1997**, 7,801-802.
 42. Song, Y. Z; Li, X; Song, Y; Cheng, Z. P; Zhong, H; Xu, J. M; Lu, J. S; Wei, C. G; Zhu, A.F; Wu, F. Y; Xu, j. *Russ. J. Phys. Chem.* **2013**, 87,74-79.
 43. Yu, D. G., *Colloids Surf B Biointerfaces.* **2007**, 59(2), 171-8.
 44. Liu,Y-C; Lin, L-H., *Electrochem.commun.* **2004**,6(11), 1163-1168.
 45. Goia, D.V; Matjevic. *New J.Chem.***1998**, 22,1203-1215.
 46. Jana, N. R; Gearheart, L; Murphy, C., *Adv. Mater.* **2001**,13(18),1389-1393.
 47. Raveendran, P; Fu, J; Wallen, S. L. *J. Am. Chem. Soc.* **2003**, 125, 13940-13941.
 48. Beveridge, T. J; Murray, R. G. E., *J. Bacteriol*, **1960**, 141(2), 876-887.
 49. Srivastava, S. K; Constanti, M., *J. Nanoparticle Res.* **2012**, 14(4), 831.
 50. Otari, S; Patil, R; Nadaf, N; Ghosh, S., *J. Mater. Lett.* **2012**, 72, 92-94.
 51. Bhargava, A; Jain, N; Khan, M. A; Pareek, V., *J. Environ. Manage.* **2016**, 183, 22-32.
-

52. Da Silva Ferreira, V; Conz Ferreira, M. E; Lima, L. M. T. R; Frases, S; de Souza, W; Sant Anna, C., *Enzyme Microb. Technol.* **2017**, 97, 114-121.
53. Cao, J; Guenther, R. H; Sit, T. L; Opperman, C. H, Lommel, S. A; Willoughby, J. A., *Small.* **2014**, 10(24).
54. Shankar, S. S; Ravi, A; Ahmed, A; Sastry, M. J., *Colloid Interface Sci.* **2004**, 275, 496-502.
55. Gardea-Torresdey, J. L; Parsons, J. G; Peratta-Videa, J; Troiani, H, E; Santiago, P; Yacaman, M., *J. Nano Lett.* **2002**, 2(4), 397-401.
56. Chandran, S. P; Choudhary, M; Pasricha, R; Ahmad, A; Sastry, M. *Biotechnol Prog.* **2006**, 22(2), 577-83.
57. Philip, D., *Spectrochim Acta A Mol. Biomol. Spectrosc.* **2011**, 78(1), 327-331.
58. Elumalai, E. K; Prasad, T. N. V. K. V; Hemachandran, J; Viviyani, T. S; Thirumalai, T; David, E., *Int. J. Pharm. Sci. Res.* **2010**, 2(9), 549-554.
59. Ahmed, S; Annu; Manzoor, K; Ikram, S., *J. Bionanosci.* **2016**, 10, 1-6.
60. Haruta, M; Ueda, A; Tsubota, S; Torres Sanchaz, R. M. *Catal. Today.* **1996**, 29(1-4), 443-447.

61. Jurgen, O; Rainer, G; Rolf, E. J; Marc, A; Frank, G; Kirill, K., J. *Catal.* **2008**, *258*, 210-218.
 62. Yeshchenko, O. A; Dmitruk, I. M; Alexeenk, A. A; Kotko, A. V; Verdal, J; Pinchuk, A. O., *Ukr. J. Phys.* **2012**, *57(2)*, 266-277.
 63. Tan, N; Zhou, Z. Y; Sun, S. G; Ding, Y; Wang, Z. L., *Science.* **2007**, *316*, 732-735.
 64. Edelstein, A. S; Cammarata, R. C., *Nanomaterials: Synthesis, Properties and Applications*. 2nd edn. London: CRC press, Taylor and Francis Group; **1998**.
 65. Carcia, P. F; Shah, S. I; Zeper, W. B., *Appl. Phys. Lett.* **1990**, *56(23)*, 2345-2347.
 66. Thanh, N. T. K; Maclean, N; Mahiddine, S., *Chem.Rev.* **2014**, *114*, 7610-7630.
 67. Janos, H. F, *Nanoparticles and Nanostructured Films- Preparation, Characterization and Applications*. Newyork. Wiley- VCH, **1998**.
 68. Jiang, N; Zhuo, X; Wang, J. *Chem.Rev.* **2018**, *118(6)*, 3054-3099.
 69. Emily Townsend; Garnett W. Bryant, *Nano Letters* **2012**, *12 (1)*, 429-434.
 70. Wilson, A. J; Willets, K. A., *Annu. Rev. Anal. Chem.* **2016**, *9*, 27-43.
-

71. Mie, *Annalen der Physik*. **1908**, 330(3), 377-445.
 72. Gans, R., *Ann.Phys*, **1912**, 342, 881.
 73. Drude, P., *Annalen der Physik*. **1900**, 306(3), 566-613.
 74. Levy, O; Stroud, D., *Phys. Rev. B*. **1997**, 56, 13.
 75. McNamara, K; Tofail, S. A. M., *Adv. Phys.* **2016**, 2, 54-88.
 76. Azharuddin, M; Zhu, G.H; Das, D; Ozgur, E; Uzum, L; Turmer, A. P. F; Patra, H. K. *Chem. Commun.* **2019**, 55, 6964-6996.
 77. Ramos, A.P; Cruz, M. A. E; Tovani, C. B; Ciancaglini. P, *Biophys. Rev.* **2017**, 9(2), 79-89.
 78. Khan, Z. U. H; Khan, A; Chen. Y; Shah, N. S; Muhammed, N; Khan, A. U; Tahir, K; Khan, F. U; Murtaza, B; Hassan, S. U; Quisrani, S. A; Wan, P. J. *Photochem. Photobiol B.* **2017**, 173, 150-164.
 79. Angela P. Blum; Jacquelin K. Kammeyer; Anthony M. Rush; Cassandra E. Callmann; Michael E. Hahn; Nathan C. Gianneschi, *J. Am. Chem. Soc.* **2015**, 137 (6), 2140-2154.
 80. Wagner, A.M; Knipe, J. M; Orive, G; Peppas, N. A., *Acta Biomaterialia.* **2019**, 94, 44-63.
 81. Matea, C. T; Mocan, T; Tabaran, F; Pop, T; Mosteanu, O; Puia, C; Iancu, C; Mocan, L., *Int J Nanomedicine.* **2017**, 12, 5421-5431.
-

82. Ito, A; Shinkai, M; Honda, H; Kobayashi, T., *J. Biosci. Bioeng.* **2005**, *100(1)*, 1-11.
 83. Alexiou, C; Jurgons, R; Seliger, C; Iro, H. J., *Nanosci Nanotechnol.* **2006**, *6(9-10)*, 2762-8.
 84. Anderson, S. D; Gwenin, V. V; Gwenin, C. D., *Nanoscale Res. Lett.* **2019**, *14*, 188.
 85. Alshehri, R; Ilyas, A. M; Hasan, A; Arnaout, A; Ahmed, F; Memic, A., *J. Med. Chem.* **2016**, *59(18)*, 8149-8167.
 86. Semon, J; Flahaut, E; Golzio, M., *Materials.* **2019**, *12(4)*, 624.
 87. Porto, S; Rosa, A. D; Caraglia, M., *Int. J. Immunopath. Ph.* **2015**, *28(1)*, 4-13.
 88. Sokolov, K; Follen, M; Aron, J; Pavlova, I; Malpica, A; Lotan, R; Richards-Kortum, R., *Cancer Res.* **2003**, *63*, 1999-2004.
 89. Huang, X; El-Sayed, I. H; Qian, W; El-Sayed, M.A., *Nano.Lett.* **2007**, *7(6)*, 1591-1597.
 90. Haifeng Wang; Terry B. Huff; Daniel A. Zweifel; Wei He; Philip S. Low; Alexander Wei; Ji-Xin Cheng, *Proc. Natl. Acad. Sci.* **2005**, *102 (44)*, 15752-15756.
 91. Durr, N. J; Larson, T; Smith, D. K; Korgel, B.A; Sokolov, K; Ben-Yakor, A., *NanoLett.* **2007**, *7(4)*, 941-945.
-

92. Riley, R. S; Day, E. S., *Interdiscip Rev Nanomed Nanobiotechnol.* **2017**, 9(4), 1449.
 93. Pistillides, C. M; Joe, E. K; Wei, X; Anderson, R. R; Lin, C. P., *Biophys. J.* **2003**, 84(6), 4023-4032.
 94. El-Sayed, I. H; Huang, X; El-Sayed, M. A., *Cancer Lett.* **2006**, 239, 129-135.
 95. Austin, L. A; Mackey, M. A; Dreaden, E. C; El- Sayed, M. A., *Arch Toxicol.* **2014**, 88(7), 1391-1417.
 96. Malekzad, H; Zangabad, P. S; Mirshekari, H; Karimi, M; Hamblin, M. R., *Nanotechnol. Rev.* **2017**, 6(3), 301-329.
 97. Doria, G; Conde, J; Vejgas, B; Giestas, L; Almeida, C; Assuncao, M. *Sensors.* **2012**, 2(2), 1657-1687.
 98. Othman, A; Karimi, A; Andreescu, S., *J. Mater. Chem. B.* **2016**, 4, 7178-7203.
 99. Elyahanian, R; Storhoff, J. J; Mucic, R. C; Letsinger, R. L; Mirkin, C. A., *Science.* **1997**, 277, 5329.
 100. Cao, Y. C; Jin, R; Mirkin, C. A., *Science.* **2002**, 297, 1536.
 101. Li, H; Rothberg, L., *Proc. Natl. Acad. Sci. U. S. A.* **2004**, 101(39), 14036-14039.
 102. Tsai, C-S; Yu, B. T-B; Chen, C-T., *Chem Commun.* **2005**, 34(34), 4273-5.
-

103. Lan, D; Li, B; Zhang, Z., *Biosens. Bioelectron.* **2008**, *24(4)*, 934-938.
104. Nasaruddin, R. R; Chen, T; Yan, N; Xie, J., *Coord. Chem. Rev.* **2018**, *368*, 60-79.
105. Raza, A; Javed, S; Qureshi, M. Z; Khan, M. U; Khan, M. S., *Appl. Nanosci.* **2017**, *7(7)*, 412-437.
106. Dotzauer, D. M; Battacharjee, S; Wen, Y; Bruening, M. L., *Langmuir.* **2009**, *25*, 1865-1871.
107. Jiang, Z-L; Liu, C-Y; Sun, L-W., *J. Phys. Chem. B.* **2005**, *109(5)*, 1730-1735.
108. Nilesh C. Sharma; Shuvendra V. Sahi; Sudip Nath; Jason G. Parsons; Jorge L. Gardea-Torresdey; Tarasankar Pal, *Environ Sci Technol.* **2007**, *41(14)*, 5137-5142.
109. Mukherjee,P; Patra, C.R; Ghosh, A; Kumar, R; Sastry, M., *Chem. Mater.* **2002**, *14(4)*, 1678-1684.
110. Pina, C.D; Falletta, E; Ross, M. *Top. Catal.* **2007**, *44*, 1-2.
111. Raman, C.V., *Nature.* **1928**, *121(3051)*, 619-619.
112. Bumbrab, G.S; Sharma, R. M., *Egypt. J. Forensic Sci.* **2016**, *6(3)*, 209-215.

113. Venkeirsbilck, T; Vercauteren, A; Baeyens, W; Weken, G.V; Verpoort, F; Vergote, G; Remon, J. P., *Trends Analyt Chem.* **2002**, *21(12)*, 869-877.
 114. Das, R. S; Agarwal, Y. K., *Vib. Spectrosc.* **2011**, *57(2)*, 163-176.
 115. Ellas, D. I; Goodacre, P., *Analyst.* **2016**, *131*, 875-885.
 116. Fleischmann, M; Hendra, P. J, Mcquilla, A., *J. Chem. Phys. Lett.* **1974**, *26*, 163-166.
 117. Kneipp, K; Kneipp, H; Itzkan, I; Dasari, R. R; Feld, M.S., *J. Phys. Condens. Matter.* **2002**, *14*, 597-624.
 118. Zhang, X. Y; Young, M. A; Lyandres, O; Van Duyne, R. R., *J. Am. Chem. Soc.* **2005**, *127*, 4484-4489.
 119. Jeanmaire, D. L; Van Duyne, R. P., *J. Electroanal. Chem.* **1977**, *84*, 1-20.
 120. Albrecht, M. G, Creighton, J. A., *J. Am. Chem. Soc.* **1977**, *99(15)*, 5215-5217.
 121. Nie, S. M; Emory, S. R., *Science.* **1997**; *275*, 1102-1106.
 122. Kneipp, K; Wang, Y; Kneipp, H; Perelman, L. T; Itzkan, I; Dasari, R. R; Feld, M.S., *Phys. Rev. Lett.* **1997**, *78*, 1667-1670.
 123. Stiles, P. L; Dieringer, F. A; Shah, N. C; Van Duyne, R. P., *Annu. Rev. Anal. Chem.* **2008**, *1*, 601-626.
-

-
124. Doering, W. E; Nie, S. M., *J. Phys. Chem. B.* **2002**, *106*, 311-317.
 125. Otto, A., *J. Raman Spectrosc.* **2002**, *33*, 593-598.
 126. Xia, L; Chen, M; Zhao, X; Zhang, Z; Xia, J; Xu, H; Sun, M., *J.Raman. Spectrosc.* **2014**, *45(7)*, 533-540.
 127. Creighton, J A., *Surf. Sci.* **1983**, *124(1)*, 209-219.
 128. Kottmann, J. P; Matrin, O. J. F; Smith, D. R; Schultz, S., *Chem. Phys. Lett.* **2001**, *341(1-2)*, 1-6.
 129. Ru, E. C; Mayer, M; Blackie, E; Etchegoin, P. G., *J. Raman. Spectrosc.* **2008**, *39(9)*, 1127-1134.
 130. Kerker, M., *Acc. Chem. Res.* **1984**, *17(8)*, 271-277.
 131. Ding, S-Y; You, E-M; Tian, T-Q; Moskovits, M., *Chem. Soc. Rev.* **2017**, *46*, 4042-4076.
 132. Muehlethaler, C; Leona, M; Lambardi, J. R., *Anal. Chem.* **2016**, *88(1)*, 152-169.
 133. Premasiri, W. R; chen, Y; Fore, J; Brodeur. A; Ziegler, L. D., *Frontiers and Advances in Molecular Spectroscopy.* **2018**, 327-367.
 134. Sharma, B; Frontiera, R. R; Henry, A.I; Renge, E; Van Duyne, R. P., *Mater. Today.* **2012**, *15(1-2)*, 16-25.
-

135. Hudson, S. D; Chumanov, G., *Anal Bioanal Chem.* **2009**, *394*, 679- 686.
136. Pang, S; Yang, T; He, L; *Trends Analyt Chem.* **2016**, *85*, 73-82.
137. Fan, M; Andrade, G. F. S; Brolo, A. G., *Analytica Chimia Acta.* **2011**, *693*, 7-25.
138. Tolaymat, T. M; El Badawy, A. M; Genaidy, A; Scheckel, K. G; Luscton, T. P; Suidan, M., *Sci. Total Environ.* **2010**, *408*, 999-1006.
139. Yaseen, T; Pu, H; Sun, D., *Trends Food Sci Technol.* **2018**, *72*, 162-174.
140. Mosier- Boss, P. A. *nanomaterials*, **2017**, *7*, 142.
141. McNay, G; Eustace, D; Smith, W. E; Faulds, K; Graham, D., *Appl. Spectrosc.* **2011**, *65*, 825-837.
142. Yan, B; Thubagere, A; Premasiri, W. R; Ziegler, L.D; Dal Negro, L; Reinhar, B. M., *ACS Nano.* **2009**, *26*; *3(5)*, 1190-202.
143. . Temu ır, E; Boyace, I. H; Tamer, U; U ınsal, H., *Anal. Bioanal. Chem.* **2010**, *397(4)*, 1595-1604.
144. Shafer- Peltier, K. E; Haynes, C. L; Gluckberg, M. R; VanDuyne, R. P., *J. Am. Chem. Soc.* **2003**, *125*, 588-593.

-
145. Lyandres, O; Yuen, J. M; Shah, N. C; VanDuyne, R. P; Walsh, Jr, J. T; Glucksberg, M. R., *Diabetes Technol Ther.* **2008**, *10(4)*, 257-265.
 146. Kahraman, M; Zamaluva, A. I; Fakhrullin, R. F; Culha, M., *Anal. Bioanal. Chem.* **2009**, *395*, 2559-2567.
 147. Montoya, G; Cases, R; Yruela, I; Picoril, R., *J. Photochem. Photobiol.* **1993**, *58(5)*, 724-729.
 148. Feng, J-J; Murgide, D. H; Kuhlmann, U; Utesch, T; Mroginski; M. A; Hildebrandt, P; Weidinger, I. M., *J. Phys. Chem. B.* **2008**, *112(47)*, 15202-15211.
 149. Culha, M; Stokes, D; Allain, L. R; Vo- Dinh, T., *Anal. Chem.* **2003**, *75(22)*, 6196-6201.
 150. Kaminska, A; Inya-Agha, O; Forster, R. J; Keyes, T. E., *Phys. Chem. Chem. Phys.* **2008**, *10*, 4172-4180.
 151. Isola, N. R; Stokes, D. L; Vo-Dinh, T., *Anal. Chem.* **1998**, *70(7)*, 1352-1356.
 152. Lahr, R-H; Wallace, G. C; Vikesland, P., *ACS Appl. Mater. Interfaces.* **2015**, *7(17)*, 9139-9146.
 153. Han, Y; Lapitsky, R; Chou, T. M; Stafford, C. M; Du, H; Sukhishvili, S., *Anal Chem.* **2011**, *83(15)*, 5873-80.
 154. Xie, W; Schlücker, S., *Rep. Prog. Phys.* **2014**, *77*, 22.
-

155. Fahlman, B. D. *Materials Chemistry*, Springer **2007**, 357 – 412.
 156. Poole Jr., C. P.; Owens, F. J. *Introduction to Nanotechnology*, Wiley 2008, 42 – 62.
 157. Chorkendorff, I.; Niemantsverdriet, J. W. *Concepts of Modern Catalysis and Kinetics*, Wiley, **2007**, 129 - 164.
 158. Hornyak, G. L.; Tibbals, H. F.; Dutta, J.; Moore, J. J. *Introduction to Nanoscience and Nanotechnology*, Taylor & Francis Group, **2009**, 107 - 167.
 159. Kulkarni, S. K. *Nanotechnology: Principles and Practices*, Capital Publishing Company, **2007**, 107 – 156.
 160. Rogers, B.; Pennathur, S.; Adams, J. *Nanotechnology: Understanding Small Systems*. Taylor & Francis Group **2008**, 170 – 185.
 161. Kirkland A, I.; Hutchison J. L. (edited) *Nanocharacterisation*, The Royal Society of Chemistry **2007**, 1 – 136.
 162. Cheng Zong; Mengxi Xu; Li-Jia Xu; Ting Wei; Xin Ma; Xiao-Shan Zheng; Ren Hu; Bin Ren; *Chem. Rev.* **2018**, *118* (10), 4946-4980.
 163. Seungyoung Park; Jiwon Lee; Hyunhyub Ko; *ACS Appl. Mater. Interfaces* **2017**, *9*(50), 44088-44095.
 164. Ruirui Li; Bo Gui; Haiyang Mao; Yudong Yang; Dapeng Chen; Jijun Xiong, *ACS Sens.* **2020**, *5* (11), 3420-3431.
-

-
165. Nina Jiang; Xiaolu Zhuo; Jianfang Wang, *Chem. Rev.* **2018**, *118* (6), 3054-3099.
166. Paige Hall, W.; Salome N. Ngatia; Richard P. Van Duyne, *J. Phys. Chem. C* **2011**, *115* (5), 1410-1414.
167. Sundar Kunwar; Puran Pandey; Jihoon Lee, *ACS Omega* **2019**, *4* (17), 17340-17351.
168. Chuanliu Wu; Qing-Hua Xu, *Langmuir* **2009**, *25* (16), 9441-9446.
169. Carlos Diego L. de Albuquerque; Kallai M. Hokanson; Sarah R. Thorud; Regivaldo G. Sobral-Filho; Nathan C. Lindquist; Alexandre G. Brolo, *ACS Photonics* **2020**, *7* (2), 434-443.
170. Samir Kumar; Kouta Tokunaga; Kyoko Namura; Takao Fukuoka; Motofumi Suzuki, *J. Phys. Chem. C* **2020**, *124* (38), 21215-21222.
171. Le Ru, E. C.; Blackie, E.; Meyer, M.; Etchegoin, P.G., *J. Phys. Chem. C* **2007**, *111* (37), 13794-13803.
172. Faezeh Mohaghegh; Alireza Mazaheri Tehrani; Arnulf Materny, *J. Phys. Chem. C* **2021**, *125* (9), 5158-5166.
173. Dhara J. Trivedi; Brendan Barrow; George C. Schatz, *J. Chem. Phys.* **2020**, *153*, 124706.
174. Sha Liu; Guanying Chen; Paras N. Prasad; Mark T. Swihart, *Chem. Mater.* **2011**, *23* (18), 4098-4101.
-

175. Peter N. Njoki; Maurice E. D. Roots; Mathew M. Maye, *ACS Appl. Nano Mater.* **2018**, *1*(10), 5640-5645.
176. Michael P. Mallin ; Catherine J. Murphy, *Nano Lett.* **2002**, *2* (11), 1235-1237.
177. Zhang, H.; Yang, S.; Zhou, Q., *Plasmonics* **2007**, *12*, 77–81.
178. Semion K. Saikin; Yizhuo Chu; Dmitriy Rappoport; Kenneth B. Crozier; Alán Aspuru-Guzik, *J. Phys. Chem. Lett.* **2010**, *1* (18), 2740-2746.
179. Ashish Tripathi; Erik D. Emmons; Neal D. Kline; Steven D. Christesen; Augustus W. Fountain; Jason A. Guicheteau, *J. Phys. Chem. C* **2018**, *122* (18), 10205-10216.
180. Cristian Mihail Teodorescu, *Phys. Chem. Chem. Phys.* **2015**, *17*, 21302-21314.
181. Fromm; David; Sundaramurthy; Arvind; Schuck, P.; Kino; Gordon; Moerner; William, *Procedia Eng.* **2004**; *4* (5), 957-961.
182. Zayak, A. T.; Hu, Y. S.; Choo, H.; Bokor, J.; Cabrini, S.; Schuck, P. J.; Neaton, J. B., *Phys. Rev. Lett.* **2011**, *106*, 083003.
183. Nicholas Valley; Nathan Greeneltch; Richard P. Van Duyne; George C. Schatz, *J. Phys. Chem. Lett.* **2013**, *4* (16), 2599-2604.
184. Miri Sinwani; Merav Muallem; Yaakov R. Tischler, *J. Raman. Spectrosc.* **2017**, *48* (6), 829-836.
-

-
185. Ramón A. Álvarez-Puebla, *J. Phys. Chem. Lett.* **2012**, 3 (7), 857-866.
186. Nathan G. Greeneltch; Martin G. Blaber; George C. Schatz; Richard. P. Van Duyne, *J. Phys. Chem. C* **2013**, 117 (6), 2554-2558.
187. Yong-Hyok Kwon; Robert Ossig; Frank Hubenthal; Heinz-Detlef Kronfeldt, *J. Raman. Spectrosc.* **2012**, 43(10), 1385-1391.
188. Jian Ye; James Andell Hutchison; Hiroshi Uji-I; Johan Hofkens; Liesbet Lagae; Guido Maes; Gustaaf Borghsa; Pol Van Dorpea, *Nanoscale*. **2012**, 4, 1606.
189. Hongyun Guo, *Nanotechnology*. **2013**, 24 ,045608.
190. Sean T. Sivapalan; Brent M. DeVetter; Timothy K. Yang; Thomas van Dijk; Matthew V. Schulmerich; Scott Carney,P.; Rohit Bhargava; Catherine J. Murphy, *ACS Nano* **2013**, 7 (3), 2099-2105.
191. Zheng Liu; Zhi-Lin Yang; Li Cui; Bin Ren; Zhong-Qun Tian; *J. Phys. Chem C*. **2007**, 111 (4), 1770-1775.
192. George Chumanov; Konstantin Sokolov; Brian W. Gregory; Therese M. Cotton, *J. Phys. Chem.* **1995**, 99 (23), 9466-9471.
193. Cañamares, M. V.; Garcia-Ramos, J. V.; Gómez-Varga, J. D.; Domingo, C.; Sanchez-Cortes, S., *Langmuir* **2007**, 23 (9), 5210-5215.
-

194. Siliu Tan; Melek Erol; Svetlana Sukhishvili; Henry Du; *Langmuir* **2008**, *24* (9), 4765-4771.
 195. Kiang Wei Kho; Ze Xiang Shen; Hua Chun Zeng; Khee Chee Soo; Malini Olivo, *Anal. Chem.* **2005**, *77* (22), 7462-7471.
 196. Aysun Korkmaz; Maya Kenton; Gulsen Aksin; Mehmet Kahraman; Sebastian Wachsmann-Hogiu, *ACS Appl. Nano Mater.* **2018**, *1* (9), 5316-5326.
 197. Gaowu W. Qin; Juncheng Liu; Tatineni Balaji; Xiaoning Xu; Hideyuki Matsunaga; Yukiya Hakuta; Liang Zuo; Poovathinthodiyil Raveendran, *J. Phys. Chem C* **2008**, *112* (28), 10352-10358
 198. Fleger, Y; Rosenbluh, M., *J. Opt.* **2009**, *2009*, 1-5.
 199. Moskovits, M.; Suh, J.S., *J. Phys. Chem.* **1984**, *88* (23), 5526-5530.
 200. Keith T. Carron; Gayle Hurley, L., *J. Phys. Chem.* **1991**, *95*(24), 9979-9984.
 201. Joy, V. T.; Srinivasan, T. K. K., *J. Raman Spectrosc.* **2001**, *32*, 785.
 202. Rousaki, Anastasia & Vargas; Emmanuel & Vázquez; Cristina & Aldazabal; Verónica & Bellelli; Cristina & Carballido Calatayud; Mariana & Hajduk; Adam & Palacios; Oscar &
-

- Moens; Luc & Vandenabeele; Peter; *Trends Analyt Chem.* **2018**, *105*, 338-351.
203. Mark R. Kagan; Richard L. McCreery, *Anal. Chem.* **1994**, *66* (23), 4159-4165.
204. Holly Fleming; Sarah McAughtrie; Bethany Mills; Michael G. Tanner; Angus Marksa; Colin J. Campbell, *Analyst.* **2018**, *143*, 5918-5925.
205. Chia-Chi Huang; Chi-Yun Cheng; Yen-Shi Lai, *Trends Food Sci. Technol.* **2020**, *100*, 349-358.
206. Lemei Cai; Zhuo Deng; Jing Dong; Shidong Song; Yiru Wang & Xi Chen, *J. Anal. Test* **2017**, *1*, 322–329.
207. Chakraborty, I.; Bag, S.; Landman, U.; Pradeep, T., *J. Phys. Chem. Lett.*, **2013**, *4*, 2769–2773.
208. Kim, K.; Lee, H. B.; Lee, J. W.; and Shin, K. S., *J. Colloid Interface Sci.* **2010**, *345*, 103–108.
209. Ballerini; David & Li; Xu & Shen; Wei, *Anal. Bioanal. Chem.* **2011**, *399*, 1869-75.
210. Ashley M. Robinson; Lili Zhao; Marwa Y. Shah Alam; Paridhi Bhandari; Scott G. Harroun; Dhananjaya Dendukuri; Jonathan Blackburn; Christa L. Brosseau, *Analyst.* **2015**, *140*, 779-785.
211. Gui-Na Xiao; Shi-Qing Man, *Chem. Phys. Lett.* **2007**, *447*(4-6), 305-309.
-

212. Zhong, L.; Hu, Y.; Xing, D., *Conference on Lasers and Electro-Optics*. **2009**, 1-2.
213. .Yong Yang; Shigemasa Matsubara; Liangming Xiong; Tomokatsu Hayakawa; Masayuki Nogami, *J. Phys. Chem. C* **2007**, *111*(26), 9095-9104.
214. Youju Huang; Liwei Dai; Liping Song; Lei Zhang; Yun Rong; Jiawei Zhang; Zhihong Nie; Tao Chen, *ACS Appl. Mater. Interfaces*. **2016**, *8* (41), 27949-27955.
215. Nathan D. Burrows; Ariane M. Vartanian; Nardine S. Abadeer; Elissa M. Grzincic; Lisa M. Jacob; Wayne Lin; Ji Li; Jordan M. Dennison; Joshua G. Hinman; Catherine J. Murphy, *J. Phys. Chem. Lett.* **2016**, *7* (4), 632-641.
216. Mahmoud A. Mahmoud; Mostafa A. El-Sayed, *J. Phys. Chem. Lett.* **2013**, *4* (9), 1541-1545.
217. Anirban Das; Nitin Yadav; Saikumar Manchala; Manisha Bungla; Ashok K. Ganguli, *ACS Omega*, **2021**, *6* (2), 1007-1029.
218. Yilong Wang; Pedro H. C. Camargo; Sara E. Skrabalak; Hongchen Gu; Younan Xia, *Langmuir*, **2008**, *24* (20), 12042-12046.
219. Umme Thahira Khatoon; Nageswara Rao, G. V. S.; Krishna Mohan Mantravadi; Yasemin Oztekin, *RSC Adv.*, **2018**, *8*, 19739-19753.

220. Wu, Lingfeng & Wu; Weiwei & Jing; Xiaolian & Huang; Jiale & Sun; Daohua & Odoom-Wubah; Tareque & Liu; Hongyu & Wang; Haitao & Li; Qingbiao, *Ind. Eng. Chem Res.*, **2013**, *52(14)*, 5085–5094.
221. Muhammed Ajmal C.; Faseela K. P.; Swati Singh; Seunghyun Baik, *Sci. Rep.*, **2016**, *6*, 34894.
222. Chang, Q.; Shi, X.; Liu, X.; Tong, J.; Liu, D.; Wang, Z, *Nanophotonics*, *6(5)*, 1151-1160.
223. Bahareh Khodashenas; Hamid Reza Ghorbani, *Arab. J. Chem.*, **2019**, *12(8)*, 1823-1838.
224. Cai, X.; Zhai, A., *Rare Met.*, **2010**, *29(4)*, 407.
225. Ali Pourjavadi; Rouhollah Soleyman, *Mater. Res. Bull.*, **2011**, *46(11)*, 1860-1865.
226. Muhammed Ajmal, C.; Faseela, K. P.; Swati Singh & Seunghyun Baik, *Sci. Rep.*, **2016**, *6*, 34894.
227. Jianmei Liu; Tao Yang; Chengxiang Li; Jinhui Dai & Yongsheng Han; *Sci. Rep.*, **2015**, *5*, 14942.
228. Gumaa A. El-Nagar; Radwan M. Sarhan; Ahed Abouserie; Natalia Maticiuc; Matias Bargheer; Iver Lauermann & Christina Roth, *Sci. Rep.*, **2017**, *7*, 12181.
229. Mukherji, S., Bharti, S., Shukla, G. & Mukherji, S., *Phys. Sci. Rev.*, **2019**, *4(1)*, 20170082.
-

-
230. Lingfeng Wu; Weiwei Wu; Xiaolian Jing; Jiale Huang; Daohua Sun; Tareque Odoom-Wubah; Hongyu Liu; Haitao Wang; Qingbiao Li, *Ind. Eng. Chem. Res.* **2013**, *52* (14), 5085-5094.
231. Hangyan Liang; Zipeng Li; Wenzhong Wang; Yoshi Wu; Hongxing Xu, *Adv. Mater.*, **2009**, *21*, 1-5.
232. Shrawan Roy, *Nanotechnology*, **2017**, *28*, 465705.
233. Tang, Bin & Li; Jing liang & Fan; Linpeng & Wang; Xungai, *RSC Adv.*, **2015**, *5*.
234. Oliveira, M.J.; Quaresma, P.; Peixoto de Almeida, M., *Sci Rep*, **2017**, *7*, 2480.
235. Shuang Lin; Wu-Li-Ji Hasi; Xiang Lin; Si-qin-gao-wa Han; Xiu-Tao Lou; Fang Yang; Dian-Yang Lin; Zhi-Wei Lu, *Anal. Methods*. **2015**, *7*, 5289-5294.
236. Turkevich, J.; Stevenson, P. C; Hillier, J., *Faraday Discuss.* **1951**, *11*, 55-75.
237. Brust, M.; Walker, M.; Bethell, D.; Schrifin, D. J.; Whyman, R., *Chem. Commun.*, **1994**, *7*, 801- 802.
238. Perrault, S. D.; Chan, W. C., *J. Am. Chem. Soc.*, **2009**, *131*(47), 17042-3.
239. Raveendran, P.; Fu, J.; Wallen, S. L., *Green Chem.*, **2006**, *8*(1), 34-38.
-

240. Jain, P. K.; Lee, K. S.; El-Sayed, El-Sayed, M. A., *J. Phys. Chem. B*, **2006**, *110*(4), 7238-7248.
241. Dykman, L.; Khlebtsov, N., *Chem. Soc. Rev.*, **2012**, *41*, 2256-2282.
242. Kneipp, K.; Kneipp, H.; Manoharan, R.; Halon, E. B.; Itzkan, I.; Dasari, R. R., *Appl. Spec.* **1998**, *52*, 1493-1497.
243. Sakai, Toshio; Alexandridis, Paschalis, *Macromolecular synopsis.*, **2010**, *289*, 18-24.
244. Mukherjee, Shatabdi; Singh, Sashi; Radhakrishnan, T. P, *Chem. Comm.* **2005**, 2387-9.
245. Xuping Sun Dr.; Shaojun Dong Prof; Erkang Wang Prof, *Angew. Chem.*, **2004**, *116*(46), 6520-6523.
246. Hsin-Cheng Chu; Chun- Hong Kuo; Mchael H. Huango, *Inorg. Chem.* **2006**, *45*(2), 808-813.

APPENDIX

Refereed Journals

1. Anju Ajayan; Vineeth Madhavan; **Sumitha Chandran** and Poovathinthodiyil Raveendran*, *A simple anti-solvent method for the controlled deposition of metal and alloy nanoparticles*, *New J. Chem.*, **2018**, *42*, 11979-11983.
2. Vineeth Madhavan; Pranav Gangadharan; Anju Ajayan; **Sumitha Chandran**; Poovathinthodiyil Raveendran*, *Microwave-assisted solid-state synthesis of Au nanoparticles, size-selective speciation, and their self-assembly into 2D superlattice*. *Nano-Structures & Nano-Objects*, **2019**, *17*, 218-222.

Conference Proceedings

1. Poster presentation at the Fifth International Conference on Nanoscience and Nanotechnology (ICONN 2019) organized by Department of Physics and Nanotechnology, SRM IST, Kattankulathur during 28-30 January 2019.
2. Oral presentation at International conference on advanced materials (ICAM) organized by department of Physics, Nirmalagiri college, Kannur during 12-14 June 2019.